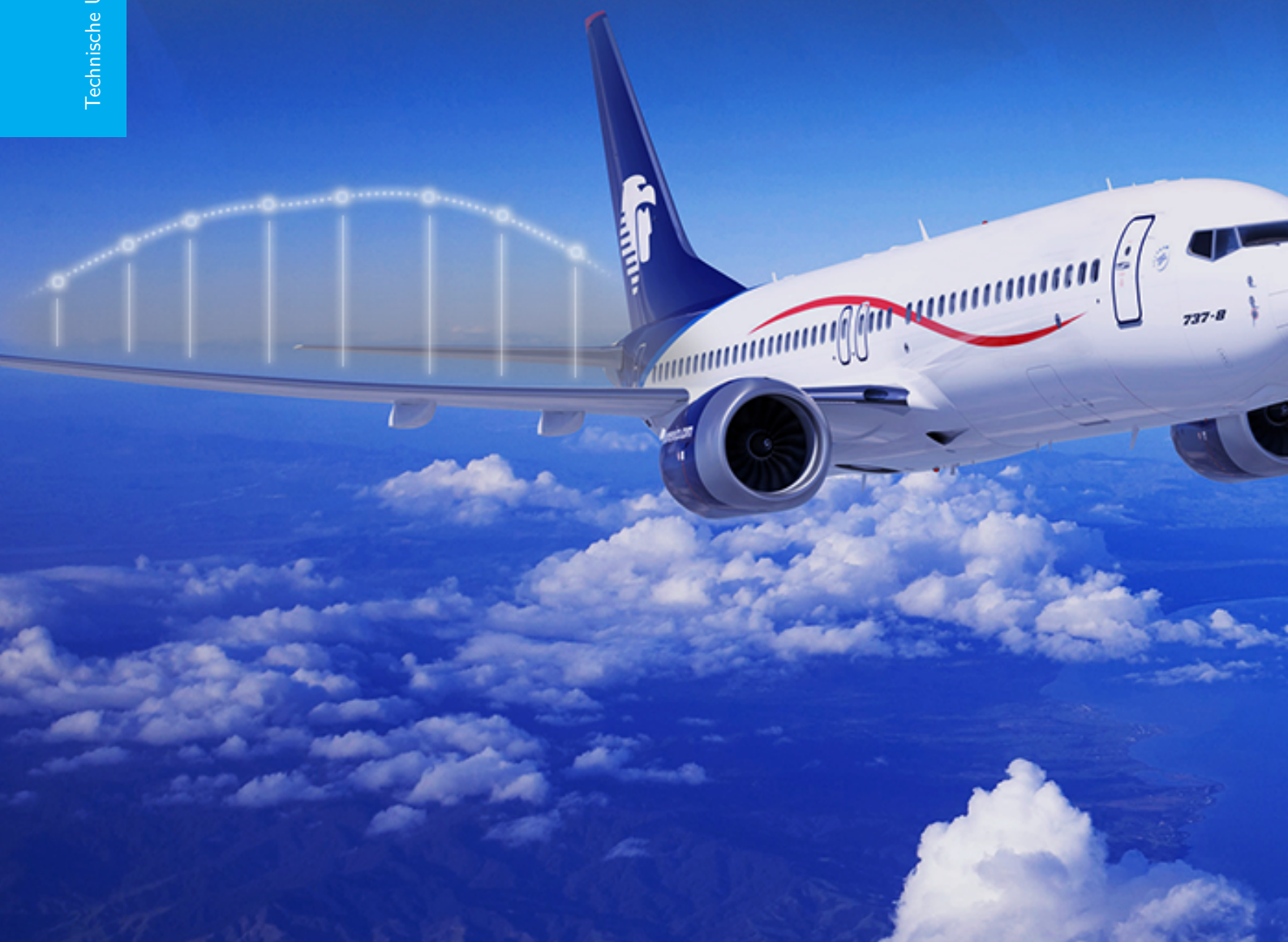


# A Medium-Fidelity Method for Rapid Maximum Lift Es- timation

Thesis Report

B. Singh B.Sc.





# A MEDIUM-FIDELITY METHOD FOR RAPID MAXIMUM LIFT ESTIMATION

## THESIS REPORT

by

**B. Singh B.Sc.**

in partial fulfillment of the requirements for the degree of

**Master of Science**  
in Aerospace Engineering

at the Delft University of Technology,  
to be defended publicly on Wednesday January 18, 2017 at 9:00 AM.

Supervisor: Dr. ir. R. Vos  
Thesis committee: Prof. dr. ir. L. L. M. Veldhuis  
Dr. ir. A. H. van Zuijlen

Student number: 4116879  
Thesis registration number: 112#17#MT#FPP

Cover image: Credits: Marc De La Paz, marcdelapaz@gmail.com

An electronic version of this thesis is available at <http://repository.tudelft.nl/>.

Department of Flight Performance and Propulsion  
Faculty of Aerospace Engineering • Delft University of Technology



# PREFACE

This thesis marks the completion of both my Master program 'Flight Performance and Propulsion' of the faculty of Aerospace Engineering at Delft University of Technology and my student career. This thesis report documents the research endeavors to build a low-speed maximum lift coefficient prediction method for conceptual aircraft design.

Several peers and supervisors aided me in my effort to establish this method. Hence, I would like to express my sincere gratitude to them. First of all, I would like to thank my supervisor Roelof Vos for his exceptional support and guidance throughout the past year. His inspiration and creativity helped me to achieve more than I could imagine at the start of my thesis. I would like to extend my gratitude to Leo Veldhuis and Alexander van Zuijlen for chairing in my exam committee.

Also, the fellow students of 'Kamertje 1' made my graduation project unforgettable and much more enjoyable. Specifically, I would like to express my heartfelt gratitude to Jelle Boersma and Malcom Brown for aiding me with my research and all the troubles that came with the Initiator. Furthermore, I would like to commend my friend Tahmitah Dirksz for helping me relax during the stressful periods throughout my career as an Aerospace Engineering student. To complete my gratitude, I would like to praise my parents and family for their unconditional support and guidance that kept me motivated during my student career.

*B. Singh B.Sc.  
Delft, January 2017*



# SUMMARY

Within this thesis, methods to predict the low-speed maximum lift coefficient have been analyzed. Hereby, the research goal was to extend the conceptual/preliminary design routine the Initiator which is designed by the Flight Performance & Performance group of the TU Delft. The Initiator is a rapid aircraft design routine, programmed in MatLab, that synthesizes the preliminary design of transport aircraft from a set of top-level requirements. Within the Initiator, it was found that maximum lift coefficient prediction method lacked fidelity. For example, the maximum lift coefficient of the Airbus A320 was over estimated by 190%. Hence, the goal of this thesis was to develop a rapid method for predicting the maximum lift coefficient of an aircraft while adhering to a prediction accuracy that pertains to a conceptual design level. Here, rapid is defined as within 15 seconds and a conceptual design accuracy is reached when the difference between the estimated and measured  $C_{L_{max}}$  is within 15%. Also, the developed  $C_{L_{max}}$  prediction method was to be translated to a MatLab tool, which was to be incorporated within the Initiator.

Initially, a literature study has been conducted to expose the relevant variable which dictate maximum lift coefficient prediction. Here, it was found that the wing geometry, especially the sweep angle, airfoil geometry, Mach number, and Reynolds number all dictate the onset of stall over a lifting surface. Also, it was found that the maximum lift coefficient of the wing has a significant impact on the conceptual design phase of an aircraft. As such, the maximum lift coefficient of the wing affects the size of the wing, size of the engine and dictates the airfield performance. For an efficient wing design, high-lift devices are required since they allow for a variable geometry wing which can change according to the performance requirements which found during the various stages of the mission profile of an aircraft.

Continuing, an extensive analysis on the flow physics surrounding stall has been conducted. Here, it was found that there is a significant difference between two-dimensional aircraft stall and 3-dimensional wing stall. Airfoils suffer from the three different stall types: leading-edge stall which often occurs on thin airfoils, trailing-edge stall which is commonly found on thick airfoils and a combination of the aforementioned stall types. Stall on swept wings is dictated by a spanwise boundary layer flow, which acts as a natural form of boundary layer control which postpones stall. Also, the planform geometry plays a crucial role in where the initial stall on a wing is formed and the propagation thereof.

Subsequently, several analytically methods that both account for these stall effects and enable the prediction of the maximum lift coefficient were discussed and a trade-off between the methods was conducted. From this trade-off, it was found that both the Pressure Difference Rule and the so-called Critical Section Method were both rapid and easily implemented within the Initiator. Therefore, both methods were selected as candidates for the Initiator and were analyzed against robustness, accuracy and versatility accordingly.

The Critical Section Method was incorporated by coupling Athena Vortex Lattice and the ESDU 84026 method for determining an airfoil's maximum lift coefficient. Within this method, stall is reached when the spanloading, obtained from the vortex-lattice, is locally equal the wing section's  $c_{l_{max}}$ . The Pressure Difference Rule on the other hand, determines wing stall by implementing an empirical chordwise pressure difference criterion. Hereby, wing stall is reached when the wing section's chordwise pressure difference, at an angle of attack, equals to the critical pressure difference which is empirically derived and depends on both the Mach- and Reynolds number. For the implementation of the Pressure Difference Rule, a two-dimensional vortex-panel method was coupled with a downwash model to determine the wing's induced angle of attack distribution.

Both the Pressure Difference Rule and Critical Section Method were validated against windtunnel experiments, both for wing only samples and wing + fuselage models. The approximation of clean maximum lift coefficient showed to be in good agreement, about 3% error, with windtunnel tests for straight wings when incorporating the Critical Section Method. A contrast was observed with the Pressure Difference Rule as this method is not suitable on straight (or low-swept) wings that incorporate airfoils that stall from the trailing-edge. This information became apparent after an interview with the leading researcher behind the Pressure Difference Rule. Similarly, swept wings have been tested with both the Pressure Difference Rule and Critical Section Method. Here, the Pressure Difference Rule was within a 5% error margin for three clean swept-back wings. On the contrary, The Critical Section Method lacked fidelity in determining the  $C_{L_{max}}$  of swept wings due to the negligence of spanwise boundary layer flow.

Proceeding, the Pressure Difference Rule was validated against two high-lift swept-back wings which had full span single-slotted Fowler flaps. Here, it was found that the maximum error in the maximum lift coefficient approximation was +11% on a kinked swept-back wing with a 10° deflected single-slotted Fowler flap. The subsequent  $C_{L_{\max}}$  estimations on high-lift wings with flaps deflections of 0°, 25° and 40° showed to be within a 5% error margin when compared to measurements.

Finally, a Newton-Raphson root-finding algorithm was incorporated. With this, both the Pressure Difference Rule and Critical Section Method converged within 3 – 4 seconds for clean configuration and 5 – 7 seconds for high-lift wings. Hence, meeting the requirements which was set by the Initiator.

To conclude, a conjunction between the Pressure Difference Rule and the Critical Section Method is required within the Initiator to increase the design space of  $C_{L_{\max}}$  predictability. This is because the Pressure Difference Rule is applicable to swept wings and straight wings with leading-edge stall while the opposite is true for the Critical Section Method, which solely works on straight wings.

# CONTENTS

<b>List of Figures</b>	<b>ix</b>
<b>List of Tables</b>	<b>xiii</b>
<b>Nomenclature</b>	<b>xv</b>
<b>I Part I: A Medium Fidelity Method for Rapid Maximum Lift Estimation</b>	<b>1</b>
<b>1 Introduction</b>	<b>3</b>
1.1 Background . . . . .	3
1.2 Research Goal . . . . .	4
1.3 Thesis outline . . . . .	5
<b>2 Theoretical Background</b>	<b>7</b>
2.1 The Initiator . . . . .	7
2.2 Maximum lift coefficient design topology . . . . .	9
2.2.1 Definition . . . . .	9
2.2.2 Mission requirements . . . . .	11
2.2.3 The need for high-lift devices . . . . .	12
2.2.4 Design principles of the maximum lift coefficient . . . . .	14
2.3 Flow physics at maximum wing lift . . . . .	15
2.3.1 Definition of stall . . . . .	16
2.3.2 Two-dimensional section stalling characteristics . . . . .	17
2.3.3 Three-dimensional viscous flow phenomena . . . . .	19
2.3.4 Flow physics of stalling high-lift configurations . . . . .	25
2.3.5 Maximum lift coefficient experimental trends . . . . .	28
2.4 Methods for low-speed wing maximum lift coefficient prediction. . . . .	30
2.4.1 State-of-the-art . . . . .	30
2.4.2 Alpha method . . . . .	30
2.4.3 ESDU 89034 method . . . . .	31
2.4.4 Critical section method . . . . .	32
2.4.5 United States Air Force Datcom method . . . . .	33
2.4.6 Phillips and Alley's method . . . . .	34
2.4.7 Pressure difference rule . . . . .	35
2.4.8 Empirical high-lift increment factors . . . . .	36
2.4.9 Method trade-off . . . . .	37
2.5 Root finding algorithms . . . . .	39
2.5.1 Bi-section algorithm . . . . .	40
2.5.2 Newton-Raphson root finding algorithm . . . . .	40
<b>3 Methodology</b>	<b>43</b>
3.1 Critical Section Method implementation . . . . .	43
3.1.1 Maximum airfoil lift coefficient . . . . .	44
3.1.2 Aerodynamic loading analysis using Athena Vortex-Lattice solver . . . . .	47
3.1.3 Coupling of AVL and the $c_{l_{\max}}$ analysis . . . . .	51
3.2 Pressure Difference Rule implementation . . . . .	52
3.2.1 Constant-Vortex panel method . . . . .	53
3.2.2 Downwash model . . . . .	54
3.2.3 Coupling of the downwash model and inviscid panel method . . . . .	57

3.3	Maximum lift coefficient in high-lift setting . . . . .	59
3.3.1	High-lift vortex-lattice model . . . . .	59
3.3.2	Multi-element linear-strength vortex panel method . . . . .	63
3.3.3	Multi-element lift curve slope . . . . .	65
3.3.4	Flap decambering analysis . . . . .	65
3.4	Airfoil smoothing . . . . .	66
3.4.1	Airfoil parsing . . . . .	67
3.4.2	Airfoil sampling . . . . .	67
3.4.3	Test case sampling . . . . .	68
3.5	Fuselage correction . . . . .	69
3.6	Convergence optimization . . . . .	71
3.7	Verification & Validation . . . . .	73
3.7.1	ESDU 84026 $c_{l_{\max}}$ prediction validation . . . . .	73
3.7.2	Vortex-lattice grid convergence study . . . . .	75
3.7.3	Two-dimensional vortex-panel method verification . . . . .	76
3.7.4	$C_{L_{\max}}$ prediction method verification . . . . .	78
<b>4</b>	<b>Test Cases</b> . . . . .	<b>81</b>
4.1	Straight Wing . . . . .	81
4.2	Swept Wings . . . . .	83
4.2.1	Swept untwisted wing . . . . .	83
4.2.2	Swept twisted wing . . . . .	86
4.3	Swept high-lift wings . . . . .	87
4.4	Results and discussion . . . . .	89
<b>5</b>	<b>Conclusions and Recommendations</b> . . . . .	<b>93</b>
5.1	Conclusion . . . . .	93
5.2	Recommendations . . . . .	94
5.2.1	Expansion of high-lift device implementation . . . . .	94
5.2.2	Expansion to transonic Mach numbers . . . . .	94
5.2.3	Interference effects . . . . .	94
5.2.4	Trim effects . . . . .	94
5.2.5	Sweep angle vs $C_{L_{\max}}$ prediction implementation . . . . .	94
5.2.6	Fuselage model . . . . .	95
5.2.7	Downwash model . . . . .	95
5.2.8	Modified Pressure Difference Rule . . . . .	95
5.2.9	Newton-Raphson stability analysis . . . . .	95
<b>II</b>	<b>Part II: Code Report</b> . . . . .	<b>97</b>
<b>1</b>	<b>Introduction</b> . . . . .	<b>99</b>
<b>2</b>	<b>Development Requirements</b> . . . . .	<b>101</b>
2.1	Scope & Limitations . . . . .	101
2.2	Use Cases . . . . .	102
2.3	Requirements . . . . .	102
2.4	Assumptions & Simplifications . . . . .	102
<b>3</b>	<b>Prediction Tool</b> . . . . .	<b>105</b>
3.1	The Tool . . . . .	105
3.2	Working Guide . . . . .	107
3.3	Future work . . . . .	108
<b>4</b>	<b>Development Requirements</b> . . . . .	<b>109</b>
<b>A</b>	<b>Appendix A: High-lift AVL input file</b> . . . . .	<b>111</b>
<b>Bibliography</b>		<b>115</b>

# LIST OF FIGURES

2.1 N2 diagram of the Initiator (version 2.9) showing the process flow of the automated synthesis of an aircraft . . . . .	8
2.2 Initiator's computed aircraft geometry for the Airbus A320-200 (all dimensions in meters) . . . . .	10
2.3 Typical stalling pattern for a passenger aircraft during flight. Data obtained from the work of Fischenberg and Jategaonkar as cited in (Vos and Farokhi [19] ) for a Dornier 328. (left) Lift coefficient. (right) Moment coefficient . . . . .	10
2.4 Typical flight profile of an airliner . . . . .	11
2.5 Typical landing procedure . . . . .	12
2.6 Effects on the lift polars by deploying selected high-lift devices [23] . . . . .	14
2.7 Commonly used high-lift devices and their geometries [24] . . . . .	14
2.8 Typical constraint in a wing loading vs thrust loading diagram . . . . .	15
2.9 A carpet plot showing stalling speed as a function of wing loading and maximum lift coefficient for landing configuration at gross weight and standard sea level density . . . . .	15
2.10 Typical pressure distribution over the NACA 0018 airfoil as computed by XFOIL . . . . .	16
2.11 Manifestation of several states of a boundary layer around an airfoil . . . . .	17
2.12 Typical lift polar at various stall types [27] . . . . .	18
2.13 Flow characteristics of an airfoil at various stall types [28] . . . . .	18
2.14 The lift and drag curves along side typical pressure distributions at various angles of attack for trailing-edge separation with associated upper-surface stream line at $Re = 6.3 \cdot 10^6$ , $M = 0.15$ . Data obtained from McGhee and Beasley as cited in (Vos and Farokhi [19] ) . . . . .	19
2.15 The lift and drag curves along side typical pressure distributions at various angles of attack for leading-edge separation with associated upper-surface stream line at $Re = 4.0 \cdot 10^6$ , $M = 0.17$ . Data obtained from Maki and Hunton as cited in (Vos and Farokhi [19] ) . . . . .	19
2.16 Illustration of boundary layer separation on various wing geometries during a three-dimensional stall. The dark blue regions represent separated flow [10] . . . . .	20
2.17 Spanwise cross flow over a swept-back wing . . . . .	21
2.18 Comparison of two- and three-dimensional experimental lift curves of the NACA64A010 section on a 45° swept-back wing [29] . . . . .	22
2.19 Effects of sweep, aspect ratio, and Mach number on the comparison between two- and three-dimensional lift curves [29] . . . . .	22
2.20 Comparison of two- and three-dimensional experimental pressure distributions at $c_{l_{\max}}$ for the NACA64A010 airfoil [29] . . . . .	23
2.21 Schematic view of a leading-edge vortex flow and the associated effects on the local pressure- and lift distributions of a sweptback wing ( $\Lambda_{c/4} = 45^\circ$ ) of aspect ratio 3.5, which incorporates circular-arc airfoils at $C_L = 0.67$ [26] . . . . .	24
2.22 Graphical representation the vortices which are generated at the wing tips with their associated effects on the local downwash velocity . . . . .	24
2.23 Graphical representation of the effects of the induced angle of attack on both the lift- and drag coefficient of a wing section and a representation of $\alpha_{\text{eff}}$ [30] . . . . .	25
2.24 Trailing-edge stall on the flap of a two-element high-lift configuration [3] . . . . .	25
2.25 Trailing-edge stall on the main component of a two-element high-lift configuration [3] . . . . .	26
2.26 Leading-edge stall on the main component of a two-element high-lift configuration [3] . . . . .	26
2.27 Flow separation on the slat of a three-element high-lift configuration [3] . . . . .	27
2.28 Trailing-edge stall on the main component of a three-element high-lift configuration [3] . . . . .	27
2.29 Leading-edge stall on the main component of a three-element high-lift configuration [3] . . . . .	27
2.30 The airfoil of the Airbus A320 in landing configuration [19] . . . . .	28
2.31 The effects of Mach number on the two-dimensional maximum lift coefficient . . . . .	29
2.32 The effects of Reynolds number on the two-dimensional maximum lift coefficient . . . . .	29
2.33 A visual of the $\alpha$ method routine to approximate the non-linear part of a lift polar [4] . . . . .	31

2.34 Lift distribution near stall as predicted by a vortex-lattice method and the distribution of section maximum lift coefficient[10] . . . . .	32
2.35 Empirical $\frac{C_{Lmax}}{C_{lmax}}$ ratio determined by USAF Datcom [10, 12] . . . . .	33
2.36 Empirical $\Delta C_{Lmax}$ as determined by USAF DATCOM for $\Lambda_{LE} = 0$ and $\Lambda_{LE} = 20$ [10, 12] . . . . .	34
2.37 Behavior of sweep coefficients . . . . .	35
2.38 Critical pressure difference for given Mach number and chordwise Reynolds number [37] . . . . .	36
2.39 Example pressure difference distribution on a swept high-lift wing [37] . . . . .	36
2.40 Pressure Difference Rule validation against wind tunnel measurements [37] . . . . .	36
2.41 Upward increment in airfoil lift polar due to the deployment of a flap by $20^\circ$ [11] . . . . .	37
2.42 Planform of a wing where the shaded area is the portion of the wing planform area affected by deployed flaps [11] . . . . .	37
2.43 Graphical representation of the bisection method . . . . .	40
2.44 Graphical representation of the Newton-Raphson algorithm . . . . .	41
 3.1 Airfoil geometry nomenclature as per IHS ESDU [42] . . . . .	44
3.2 Lift coefficient increment for airfoils with smooth leading edges [42] . . . . .	45
3.3 Correction factor for the theoretical lift curve slope according to Datcom [12] . . . . .	46
3.4 Correction factor on the $c_{l_{max}}$ for airfoils with rear loading [42] . . . . .	47
3.5 Factors that correct the computed maximum lift coefficient for Mach number effects [42] . . . . .	47
3.6 Schematic overview of a vortex-lattice method [43] . . . . .	48
3.7 Vortex-lattice grid for a clean wing with a surface area of $0.55 \text{ m}^2$ , span of 2.15m, a taper ratio of 0.35, quarter chord sweep of $28^\circ$ and an aspect ratio of 8.35 . . . . .	50
3.8 Change in flow-tangency boundary condition for a multi-surface wing where the trailing surface is deflected by $40^\circ$ . The wing has a surface area of $0.61 \text{ m}^2$ , span of 2.15m, a taper ratio of 0.25 and an aspect ratio of 7.53 . . . . .	50
3.9 Spanwise loading on a clean wing at $\alpha = 5^\circ$ . The wing has a surface area of $0.61 \text{ m}^2$ , span of 2.15m, a taper ratio of 0.25, quarter chord sweep of $28^\circ$ and an aspect ratio of 7.53 . . . . .	51
3.10 Flow chart of the Critical Section Method for clean $C_{L_{max}}$ prediction as implemented in this thesis . . . . .	52
3.11 Pressure Difference Rule for maximum lift [37] . . . . .	53
3.12 Schematic overview of a constant-strength vortex panel method [43] . . . . .	54
3.13 Scheme presented by Elham [44] to determine the spanwise downwash distribution . . . . .	55
3.14 Flow chart of the downwash model for the calculation of the induced angle of attack as implemented in this thesis . . . . .	57
3.15 Schematic of cosine distributed wing strips at which $\Delta C_{P_{crit}}$ and $\Delta C_{P_{eff}}$ are to be determined . . . . .	58
3.16 Pressure difference rule flow chart for a clean $C_{L_{max}}$ prediction . . . . .	59
3.17 The slotted Fowler flaps of a Boeing 747-400 . . . . .	60
3.18 Gap filling methods in a vortex-lattice method as been tested by Moerland [47] . . . . .	60
3.19 Bunching of vortex panels at the overlap of the clean and high-lift wing surfaces. The red lines indicate the junction of two different surfaces and the grey dotted lines represent vortex legs . . . . .	61
3.20 Representation of a single-slotted flap with multiple airfoil definition for both the main and flap element . . . . .	62
3.21 Graphical representation of used airfoil definitions at spanwise locations. The red lines indicate the implementation of the clean airfoil. At the blue lines, the flap airfoil is utilized. The main airfoil of the high-lift airfoil configurations is located at the purple lines . . . . .	62
3.22 Vortex-lattice grid for a high-lift wing with a full span trailing-edge flap. This wing has a surface area of $0.55 \text{ m}^2$ , span of 2.15m, a taper ratio of 0.35, quarter chord sweep $28^\circ$ and an aspect ratio of 8.35 . . . . .	63
3.23 Spanwise loading on a multi-surface wing at $\alpha = 15^\circ$ where the trailing surface is deflected by $40^\circ$ . The wing has a surface area of $0.61 \text{ m}^2$ , span of 2.15m, a taper ratio of 0.25 and an aspect ratio of 7.53 . . . . .	63
3.24 Nomenclature used in the linear-vortex panel method [43] . . . . .	64
3.25 Nomenclature used to determine the lift curve slope for single-slotted fowler flaps [49] . . . . .	65
3.26 Flap decambering reduction curves [50] . . . . .	66
3.27 Flap angle reduction curves for single-slotted- and plain flaps as per the indicated researchers [3, 37, 50] . . . . .	66
3.28 Removal of the mean camber distribution on the Boeing747-100b airfoil . . . . .	68

3.29 Radial coordinates distribution for the Boeing737 root airfoil . . . . .	68
3.30 Comparison between the original Boeing747-100b airfoil and the resampled and parsed airfoil coordinates . . . . .	69
3.31 Boeing747-100b airfoil - Comparison between resampled and original airfoil coordinates . . . . .	69
3.32 Empirically derived data to correct the wing-only maximum lift coefficient for body effects [12] . . . . .	70
3.33 Scematic illustration of wing anhedral and wing dihedral . . . . .	71
3.34 Initial range schematic of KS-values at $\alpha = 0^\circ$ and $\alpha = 30^\circ$ for the Newton-Raphson algorithm . . . . .	72
3.35 Comparison between the Newton-Raphson- and bisection convergence for a clean wing with $45^\circ$ sweep back, aspect ratio 6, taper ratio 0.5 and a span of 11 m . . . . .	73
3.36 Validation of the ESDU 84026 method for the NACA24XX airfoil family . . . . .	74
3.37 Vortex-lattice grid densities which are used in the convergence study of the clean wing . . . . .	76
3.38 Pressure coefficient distribution over the NACA 4415 at $\alpha = 10^\circ$ and $M = 0$ - XFOIL vs constant strength-vortex panel method . . . . .	76
3.39 Inviscid pressure coefficient distribution over the NACA 6424 at $\alpha = 10^\circ$ and $M = 0$ - XFOIL vs constant strength-vortex panel method . . . . .	77
3.40 Inviscid pressure coefficient distribution over the NACA 8412 at $\alpha = 10^\circ$ and $M = 0$ - XFOIL vs constant strength-vortex panel method . . . . .	77
3.41 Pressure coefficient distribution over a multi-element airfoil at $\alpha = 2^\circ$ and $M = 0$ - MSES vs linear-vortex panel method . . . . .	78
3.42 Inviscid pressure coefficient distribution over the NACA 23012 with a plain flap at $\alpha = 8^\circ$ , $\delta_f = 15^\circ$ and $M = 0$ - XFOIL vs linear-vortex panel method . . . . .	78
3.43 Computed $C_{L_{\max}}$ results by the CSM and PDR for various leading-edge sweep angles at $M = 0.22$ and $Re_\infty = 0.96 \cdot 10^6$ for the wing geometry given in Table 3.6 . . . . .	79
3.44 . . . . .	79
4.1 The planform of the Fokker F27 wing as tested by Spigt and de Gelder [57] . . . . .	81
4.2 Stalling pattern on the Fokker F27 wing [57] . . . . .	82
4.3 Lift polar comparison between the clean Fokker F27 results [57, 58], at $M = 0.27$ and $Re = 7 \cdot 10^6$ , and the estimated lift polars as per the CSM and PDR methods & critical span loading . . . . .	83
4.4 The planform of Hunton's analyzed wing+fuselage combination [59, 60] . . . . .	84
4.5 Effective and induced angle of attack distribution perpendicular to the wing at stall for the clean wing given in Table 4.4 . . . . .	84
4.6 Lift polar comparison between the results of Hunton [59, 60], at $M = 0.2$ and $Re = 8 \cdot 10^6$ , and the estimated lift polar as per the PDR for the wing geometry given in Table 4.4 & section pressure distribution . . . . .	85
4.7 Section $c_{l_{\max}}$ distribution comparison between the measurements of Hunton [59, 60], at $M = 0.2$ and $Re = 8 \cdot 10^6$ , and the estimated $c_{l_{\max}}$ distribution as per the ESDU 84026 method for the wing geometry given in Table 4.4 . . . . .	85
4.8 Lift polar comparison between the results of Hunton [59, 60], at $M = 0.2$ and $Re = 8 \cdot 10^6$ , and the estimated lift polar as per the CSM for the wing geometry given in Table 4.4 . . . . .	86
4.9 Lift polar comparison between the results of Hunton [59, 60], at $M = 0.2$ and $Re = 8 \cdot 10^6$ , and the estimated lift polar as per the PDR for the twisted wing geometry given in Figure 4.4 & section pressure distribution . . . . .	86
4.10 Airfoil and wing geometry in high lift setting generated by the high-lift AVL routine for the geometrical properties that are presented in Table 4.7 . . . . .	87
4.11 Computed $C_{L_{\max}}$ by the high-lift PDR implementation, at $M = 0.223$ and $Re = 1.27 \cdot 10^6$ , for several flap angles and the comparison between flap angle reduction models of Figure 3.27 . . . . .	88
4.12 Comparison between estimated and measured [56] $C_{L_{\max}}$ ,at $M = 0.223$ and $Re = 1.27 \cdot 10^6$ ,for the wing only model . . . . .	88
4.13 Comparison between estimated and measured [56] $C_{L_{\max}}$ ,at $M = 0.223$ and $Re = 1.27 \cdot 10^6$ ,for the wing fuselage combination . . . . .	89
4.14 Comparison between estimated and measured [56] wing + fuselage $C_{L_{\max}}$ at various flap angles for RAE's kinked wing, $S = 0.55m^2$ , $AR = 8.5$ , $\lambda = 0.35$ , $\Lambda_{c/4} = 28$ , $M = 0.2$ . . . . .	89
4.15 Section pressure distribution comparison between chordwise, streamwise and measured local pressure distributions on a $45^\circ$ swept-back wing [29] . . . . .	90
4.16 The Modified Pressure Difference Rule for trailing-edge stall airfoils . . . . .	91

4.17 Lift polar comparison between the clean Fokker F27 results [57, 58], at $M = 0.27$ and $Re = 7 \cdot 10^6$ , and the estimated lift polars as per the CSM, PDR, and the MPDR for the wing depicted in Figure 4.1 . . . . .	91
2.1 Aircraft axis system . . . . .	103
3.1 Overview of the prediction method as implemented in the Initiator . . . . .	106
3.2 Overview of the Pressure Difference Rule as implemented in the Initiator . . . . .	107
3.3 Sample Wing . . . . .	108

# LIST OF TABLES

2.1	Airbus A320-200 geometrical wing properties . . . . .	9
2.2	Aerodynamic properties of the Airbus A320-200 predicted by the Initiator for cruise conditions . . . . .	9
2.3	Airfield performance requirements for take-off and landing [4] . . . . .	12
2.4	Comparison of two wings, one optimized for cruise (Aircraft A), and one for take-off and landing (Aircraft B) at $M_\infty = 0.8$ [4] . . . . .	13
2.5	Design space of the ESDU 89034 prediction methodology . . . . .	32
2.6	High-lift maximum lift coefficient prediction method implementation outline . . . . .	39
2.7	High-lift maximum lift coefficient prediction method scoring outline . . . . .	39
2.8	High-lift maximum lift coefficient prediction method trade-off results . . . . .	39
 3.1	 Validation of the ESDU 84026 $c_{l_{\max}}$ prediction method for NACA 4-digit series at $M = 0.38$ and $Re = 9 \cdot 10^6$ . Experimental results obtained from Abbot & von Doenhoff [32] . . . . .	 74
3.2	Validation of the ESDU 84026 $c_{l_{\max}}$ prediction method for NACA 5-digit series at $M = 0.38$ and $Re = 9 \cdot 10^6$ . Experimental results obtained from Abbot & von Doenhoff [32] . . . . .	75
3.3	Validation of the ESDU 84026 method for the NASASC2-0714 airfoil at $Re = 6 \cdot 10^6$ . Experimental results obtained from Harris et al[54] . . . . .	75
3.4	AVL grid convergence study - Clean wing . . . . .	75
3.5	AVL grid convergence study - Full span flap deflection: $\delta_f = 10^\circ$ . . . . .	75
3.6	Geometrical properties of the verified wing [56] . . . . .	79
 4.1	 Fokker F27 "Friendship" geometrical properties [58] . . . . .	 82
4.2	Comparison between the results found by Spoon [58], at $M = 0.27$ and $Re = 7 \cdot 10^6$ , and the estimated values with the Critical Section Method for the wing depicted in Figure 4.1 . . . . .	82
4.3	Comparison between the results found by Spoon [58], at $M = 0.27$ and $Re = 7 \cdot 10^6$ , and the estimated values with the Pressure Difference Rule for the wing depicted in Figure 4.1 . . . . .	83
4.4	Geometrical properties of the swept-back wing as tested by Hunton [59, 60] . . . . .	83
4.5	Comparison between the results found by Hunton [59, 60] at, $M = 0.2$ and $Re = 8 \cdot 10^6$ , and the estimated values with the Pressure Difference Rule for the wing geometry given in Table 4.4 . . . . .	85
4.6	Comparison between the results found by Hunton [59, 60] and the estimated values, at $M = 0.2$ and $Re = 8 \cdot 10^6$ , for the twisted wing geometry given in Figure 4.4 . . . . .	87
4.7	Geometrical properties of the RAE wing as tested by Lovell [56] . . . . .	87



# NOMENCLATURE

## ABBREVIATIONS

AIC	Aerodynamic Influence Matrix
AOA	Angle of Attack
AVL	Athena Vortex Lattice
CS	Certification Specification
CFD	Computational Fluid Dynamics
CSM	Critical Section Method
EASA	European Aviation Safety Agency
EMWET	Elham Modified Weight Estimation Technique
DATCOM	Data Compendium
FAA	Federal Aviation Authority
FAR	Federal Aviation Regulations
FPP	Flight Performance & Propulsion
KS	Kreisselmeier-Steinhauser
LE	Leading Edge
MAC	Mean Aerodynamic Chord
MPDR	Modified Pressure Difference Rule
MTOM	Maximum Take-Off Mass
NACA	National Advisory Committee for Aeronautics
OEM	Operative Empty Mass
PDR	Pressure Difference Rule
TE	Trailing Edge

## LATIN SYMBOLS

Symbol	Units	Description
A	-	influence matrix
AR	-	aspect ratio
a	m/s	speed of sound
B	-	Pankhurst coefficient
b	m	wing span
c	m	chord
c'	m	airfoil flap combination chord
C <sub>D</sub>	-	wing drag coefficient
C <sub>d</sub>	-	airfoil drag coefficient
c <sub>l</sub>	-	airfoil lift coefficient
C <sub>L</sub>	-	wing lift coefficient
C <sub>m</sub>	-	pitching moment coefficient
C <sub>p</sub>	-	pressure coefficient
C <sub>T</sub>	-	thrust coefficient
D / d	N / (N/m)	drag
e	-	Oswald factor (efficiency factor)
f	-	generic function
	-	Kreisselmeier-Steinhauser function value
F <sub>M</sub>	-	compressibility correction factor
F <sub>S</sub>	-	modern airfoil correction factor
K	-	Kreisselmeier-Steinhauser data-set size
L / l	N / (N/m)	lift

m	$\text{deg}^{-1}$	Newton-Raphson slope
M	-	Mach number
Re	-	Reynolds number
S	$\text{m}^2$	surface area
T	N	thrust
t	m	thickness
U	$\text{m/s}$	velocity along X
W	$\text{m/s}$	velocity along Y
	kg	weight
X / x	m	dimension along the chord
Y / y	m	dimension normal to the surface
Z / z	m	dimension along the span

## GREEK SYMBOLS

Symbol	Units	Description
$\alpha$	deg, rad	angle of attack
$\beta$	-	Prandtl–Glauert compressibility correction
$\Gamma$	-	aerodynamic vortex
$\gamma$	deg	flight path angle
$\Delta$	-	finite step
$\delta$	-	derivative
	deg	flap deflection
$\epsilon$	deg	local geometrical twist angle
	-	error margin
$\eta$	-	normalized y coordinate
$\Lambda$	deg, rad	sweep angle
$\mu$	$\text{kg}/(\text{m} \cdot \text{s})$	dynamic viscosity
$\rho$	$\text{kg}/\text{m}^3$	density (of air)
$\tau$	deg	trailing-edge airfoil angle

## SUB- & SUPERSCRIPTS

Symbol	Description
0	zero incidence
1-G	steady rectilinear flight
1.25	$x/c = 0.0125$
2D	two-dimensional
A	approach
aero	aerodynamic
crit	critical
$c/4$	quarter chord
eff	effective
f	flap
i	induced
min	minimum
max	maximum
p	panel
TO	tail-off
u	upper
um	maximum thickness
$\alpha$	slope w.r.t angle of attack
$\infty$	infinity
$\perp$	perpendicular

*"The scientists of today think deeply instead of clearly. One must be sane to think clearly, but one can think deeply and be quite insane."*

- Nikola Tesla



# I

## PART I: A MEDIUM FIDELITY METHOD FOR RAPID MAXIMUM LIFT ESTIMATION



# 1

## INTRODUCTION

### 1.1. BACKGROUND

The world's urban population is rapidly increasing towards an estimate of 5 billion by 2030. Along side this, it is predicted that the global middle class will more than double [1]. According to Airbus, an accompanied increase in general living standard and wealth among this population is expected to follow [1]. Hereby, the worldwide demand for air travel will drive the growth of the aerospace industry. Embraer quantifies this growth by an average of 4.8 percent annually through 2033 [1]. Subsequently, this growth will lead to an increased demand for aircraft that cover the full design range of commercially profitable aircraft [2].

To cope with these increasing demands, emphasis is put on an efficient aircraft design process. Hereby, a decrease in overall expense, expressed both in time and resources, during the conceptual/preliminary design of an aircraft is desirable. Due to this, empirical based, inexpensive design methods are desirable during this design phase. Unfortunately, certain key performance indicators still ought to be difficult to approximate with these inexpensive design methods [3]. One of the decisive performance indicators is the aircraft's maximum lift coefficient in high-lift setting. The difficulties associated with the predictability of the maximum lift coefficient originates from the synergy between intricate non-linear flow physics, geometry and actuation surrounding this performance indicator [3, 4].

The importance of the maximum lift coefficient is discussed by Meredith [5]. According to Meredith, an increase of 1.5% in maximum lift coefficient can possibly result in an extra 3000 kg payload at fixed approach speed. This consequently alters the design requirements on the aircraft's high-lift architecture for take-off and landing conditions. This is a snippet of the famous snowballing effect that plagues aircraft design. Therefore, the aircraft industry demands analytical methods to accurately predict an aircraft's maximum lift coefficient, as conducting flight and wind tunnel tests ought to be too expensive at a conceptual design stage.

However, to accurately estimate the maximum lift coefficient analytically seems to be challenging, even when comprehensive higher order computational fluid dynamics (CFD) and detailed information pertaining the high lift geometry is utilized [6–8]. Typical errors between 5% – 9% are currently obtained in predicting a full scale aircraft's  $C_{L_{max}}$  while requiring a computational expense in terms of days [8]. This accuracy is only obtained when the correct flow dependent turbulence models are applied. Hence, establishing a conceptual aircraft design using CFD would simply be too costly in terms of computational expenses and lack of generality. Therefore, quasi-three-dimensional methodologies or semi-empirical/empirical methods are often used during conceptual aircraft design routines [9–12]. These methods are both favorable for generality and computational expense but suffer from decreased fidelity.

TU Delft's Initiator is such a conceptual/preliminary aircraft design routine which is mostly build on semi-empirical methods. This design routine synthesizes the preliminary design of subsonic transport aircraft from a set of top-level requirements [13, 14]. TU Delft's Initiator has been validated for low-speed maximum lift coefficient prediction for an A320-200. Hereby, a low-speed clean  $C_{L_{max}}$  of 4.9 was predicted which is clearly inaccurate since current airliners achieve a clean  $C_{L_{max}}$  between 1.0 – 1.5 [10]. This inaccuracy originated from the implemented method, a multiplication of the spanwise sectional lift coefficient at critical conditions with a predefined load factor. Intricate three-dimensional flow phenomena on three-dimensional lifting surfaces during stall are neglected accordingly. Additionally, The Initiator lacked high-lift  $C_{L_{max}}$  predictability. Ideally, the addition of a rapid routine to accurately predict  $C_{L_{max}}$  for both clean and high-lift con-

figurations complement TU Delft's Initiator and broadens the workable design space of this aircraft design tool.

## 1.2. RESEARCH GOAL

In the current research, the goal is to extend the previously mentioned conceptual/preliminary aircraft design routine Initiator to enable the rapid estimation of both the clean and high-lift  $C_{L_{max}}$  in low-speed flight conditions. In light of this development, effort is made to document research objectives since they can serve as guideposts throughout the process to realize the research goal. Therefore, the research goal is realized if the following research objectives are attained:

- Understanding and exposing key variables which play a profound role in the prediction of  $C_{L_{max}}$  and understanding their working principles.
- Exploring methods and tools for rapid  $C_{L_{max}}$  prediction.
- Interrelate these methods and key variables to develop a methodology for rapid  $C_{L_{max}}$  prediction.
- Validate the developed  $C_{L_{max}}$  prediction methodology.
- Eliminate repetitive and non-creative tasks in the prediction process by developing a  $C_{L_{max}}$  prediction tool.
- Seamlessly implement the  $C_{L_{max}}$  prediction tool within TU Delft's Initiator.
- Establishing a thorough documentation of the methodology and the underlying code for future users of the Initiator.

Several research questions following from the previously established research objectives. The project is concluded when the answers to these questions are answered. The following provides the main research question that defines the current project.

*"What methodology could be implemented for the design of a maximum lift prediction tool for pre-specified aircraft configurations while adhering to a computational limitations of not more than 15 seconds and a prediction accuracy pertaining to a conceptual design level?"*

This research question is subsequently sub-divided into the following set of sub-questions:

- Which variables are pertinent to the prediction of  $C_{L_{max}}$ ?
  - What methods are available to analytically describe the effects of these variables?
  - What processes are required to interrelate these variables to obtain a  $C_{L_{max}}$  prediction model?
- What advanced computational methods/software for the prediction of maximum lift exist?
  - On what basis are these computational software evaluated for the applicability in the current project?
  - What is required to implement these computational methods in an automated scheme?
- What methods are required to design a rapid stand-alone prediction tool?
- What optimization schemes exist that entail a high degree of generality to applicability?
- What is necessary to seamlessly incorporate the prediction tool within TU Delft's Initiator?

The research documented within this thesis tries to answer the main question by answering these sub-questions in a step-by step manner. Hence, the following presents an outline of this thesis where every chapter and associated sections collaboratively try to answer one or more of these sub-questions.

### 1.3. THESIS OUTLINE

As mentioned before, an outline of this thesis is presented in this section. To start, this thesis is sub-divided in two parts. Part I discussed the research aspect of this project where in Chapter 2, an extensive summary of underlying theoretical knowledge to support this thesis is presented. Chapter 3 discusses the synergy of the utilized methodologies that became apparent in the theoretical background of Chapter 2. Chapter 4 assesses the newly established  $C_{L_{max}}$  prediction methodology by validating against wind tunnel experiments. Chapter 5 gives an extensive summary of the found conclusions and recommendations which follow from the conducted research to conclude Part I of this thesis. Part II of this thesis presents the  $C_{L_{max}}$  prediction tool, which has been established in light of the  $C_{L_{max}}$  prediction methodology. Hereby, various flow charts and uml-diagrams are presented to show-case the  $C_{L_{max}}$  prediction tool to establish a thorough documentation for future users of the Initiator.



# 2

## THEORETICAL BACKGROUND

This Chapter presents the theoretical background which is the basis of the conducted research within this thesis. Initially, the Initiator is introduced in Section 2.1. Here, the working principles and shortcomings of the Initiator is discussed. This is followed by a discussion on the design topology of the maximum lift coefficient within the conceptual aircraft design phase in Section 2.2. Subsequently, the flow physics at the maximum lift coefficient are discussed in Section 2.3 for both two- and three-dimensional lifting surfaces. Then, approaches to approximate the maximum lift coefficient are discussed in Section 2.4. Finally, root-finding algorithms are discussed in Section 2.5 for optimization purposes.

**Key words**—*Flight mission, Stall, Crossflow, Prediction, Rootfinding, Pressure Difference Rule, Critical Section Method, Initiator, Wing design, High lift*

### 2.1. THE INITIATOR

In the previous Chapter, it became clear that this thesis revolves around the development of a rapid  $C_{L\max}$  prediction method which is to be incorporated within TU Delft's Initiator. However, the working principles of the Initiator are still unclear up until this point. Hence, this Section will elaborate on the conceptual/preliminary aircraft design processes of the Initiator and demonstrate a run case for the Airbus A320-200.

The Initiator is a conceptual/preliminary aircraft design routine that is developed by TU Delft's Flight Performance and Propulsion (FPP) group. This design routine synthesizes the preliminary design of subsonic transport aircraft from a set of top-level requirements [13, 14]. The Initiator was initially conceived in 2011 for both conventional and box-wing/Prandtl aircraft [15] and has progressively been developed where it now allows for the designs of both three-surface [16] and blended-wing-body aircraft [17, 18] configurations.

The goal of the Initiator is to quickly conceive realistic aircraft designs in order to investigate the effect of newly implemented technologies and aircraft configurations. This aircraft design tool distinguishes itself from other aircraft design programs by combining empirical models with numerical models to warrant reliable analysis results that are applicable to both conventional and unconventional aircraft configurations. The Initiator is coded in the multi-paradigm numerical computing environment MatLab and is aggregated in a class-based programming structure. Hereby, XML is utilized for all the in- and output files generated by the Initiator while the open source TIXI library is used for reading and writing.

At the core of the Initiator we can find the controller that connects the aircraft object with various design and analysis modules. The main task of the controller is to control the program flow. Here, it tracks which modules have been completed and the dependencies between modules. As of now, the Initiator can be used in two different ways. Firstly, one can define a set of top-level requirements together with a desired aircraft configuration. Here, the Initiator works both as a preliminary sizing and analysis tool. Secondly, a pre-defined geometry can be loaded so that the sizing modules are skipped and analysis on the existing geometry directly initiates. Figure 2.1 displays the aggregated process flow diagram of the Initiator when starting it from a set of top-level requirements. Hereby, various modules are shown (grey boxes) on the diagonal of this N2 chart.

The white boxes indicate the variables that serve as input and/or output to various modules. The large blue arrows indicate the feed forward and feedback directions, while the three colored square perimeters mark the three (partially nested) convergence loops that are present in the Initiator. The orange line in Figure 2.1 indicates the so-called Class 2 loop while the blue and green lines indicate the Mission Analysis and Class 2.5 loops respectively.

Consider the Class 2 loop which is indicated by the orange line. Initially, the set of top-level requirements together with Initiator's internal database are used to obtain an initial estimate of the Maximum Take-Off Mass (MTOM) with the *Class1WeightEstimation*-module. Here, Initiator's database contains a large set of data on commercial conventional, turboprop and business jet aircraft as well as data on engines and Auxiliary Power Units (APU's). Next, the predicted MTOM together with the top-level design requirements are passed to the wing-thrust-loading diagram to find the most optimal design point. To size the aircraft, the newly found optimal design point together with the MTOM-estimate are used by the *GeometryEstimation*-modules to establish a geometry estimate. The developed geometry is subsequently used by the *Class2WeightEstimation*-module together with both the fuel fractions and MTOM to obtain an estimate for the Operational Empty Weight (OEM). The geometry, MTOM, fuel mass and OEM are subsequently fed to the *Aerodynamics*-modules to obtain a set of aerodynamic polars and the lift-over-drag ratio.

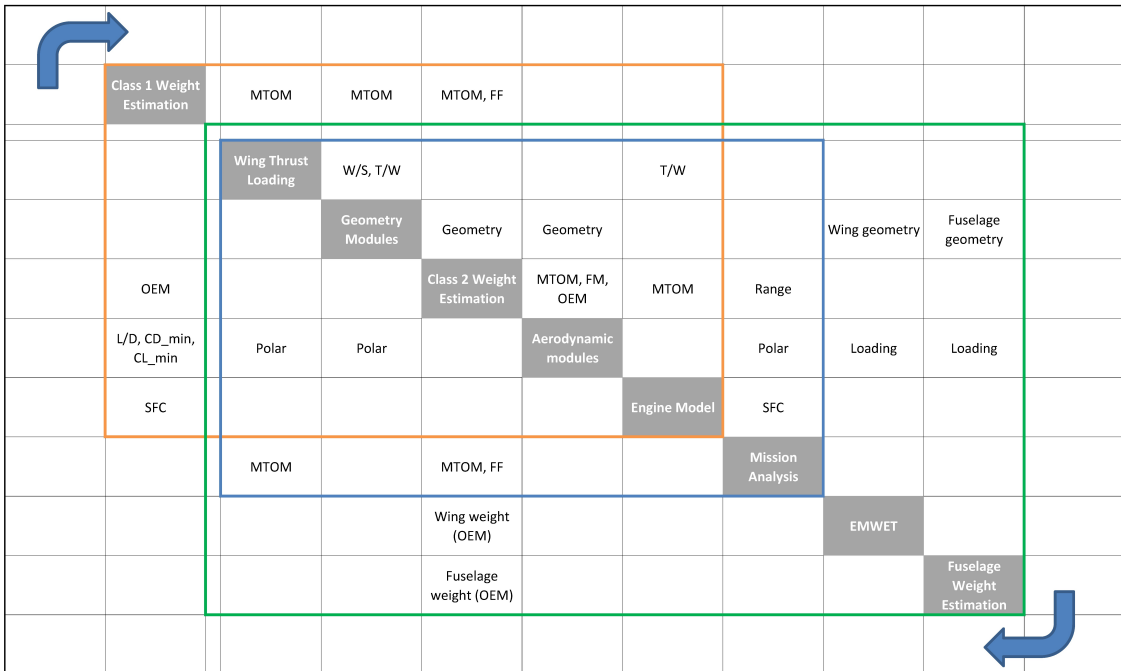


Figure 2.1: N2 diagram of the Initiator (version 2.9) showing the process flow of the automated synthesis of an aircraft

Within the *Aerodynamics*-modules the prediction of clean  $C_{L_{max}}$  resides. As will become evident, the clean  $C_{L_{max}}$  is currently overpredicted by around 190%. This has a consequence on the sizing of the wing in the *GeometryEstimation*-modules since the over-prediction of the clean  $C_{L_{max}}$  is fed back to the *GeometryEstimation*-modules with the aerodynamic polars. Subsequently, an over prediction of clean  $C_{L_{max}}$  will create a bigger wing than what actually is required. Hence, the weight is over estimated by the *Class2WeightEstimation*-module and later the *EMWET*-module and *FuselageWeightEstimation*-module when one follows the N2 chart of Figure 2.1. In fact, following the N2 chart reveals that an inaccurate approximation of  $C_{L_{max}}$  leaves its traces throughout the Initiator as a whole.

To validate the Initiator for  $C_{L_{max}}$  predictability, the Airbus A320-200 geometry is loaded in the Initiator as an existing geometry. Hereby, the Initiator bypasses the sizing modules to allow for a direct analysis on this aircraft. The main wing geometry of the airbus A320-200 is given in Table 2.1 and Initiator's computed aerodynamic and geometrical results are presented in Table 2.2 and Figure 2.2 respectively. To start, the geometrical

output of the Initiator that is depicted in Figure 2.2 has too many wheels. Secondly, the clean  $C_{L_{\max}}$  that can be found in Table 2.2 is overpredicted by 190%, since the actual clean  $C_{L_{\max}}$  amounts to 2.6 [10]. Hence, there is clearly a need to redesign the  $C_{L_{\max}}$  prediction method within the *Aerodynamics*-modules, since the current  $C_{L_{\max}}$  estimate appeared to be inadequate.

Table 2.1: Airbus A320-200 geometrical wing properties

Parameter	Value	Unit
Surface Area	110.4	[m <sup>2</sup> ]
Aspect Ratio	9.5	[–]
Taper Ratio	2.06	[–]
Quarter Chord Sweep	26.2	[deg]
Mean Aerodynamic Chord (MAC)	4.17	[m]
Tip chord	1.17	[m]
Tip t/c	0.01	[–]
Twist	0	[deg]
Dihedral	6	[deg]

Table 2.2: Aerodynamic properties of the Airbus A320-200 predicted by the Initiator for cruise conditions

Aerodynamic coefficient	Value	Unit
$C_{L_{\text{cruise}}}$	0.73	[–]
$L/D_{\text{cruise}}$	16.3	[–]
Oswald factor (e) (Clean)	0.76	[–]
Oswald factor (e) (Landing)	0.81	[–]
Oswald factor (e) (Take-off)	0.86	[–]
$C_{L_{\alpha}}$	5.07	rad <sup>–1</sup>
$C_{m_{\alpha}}$	–3.85	rad <sup>–1</sup>
$C_{L_{\max,\text{clean}}}$	4.92	[–]

## 2.2. MAXIMUM LIFT COEFFICIENT DESIGN TOPOLOGY

The Initiator has been introduced at this point. However, the design principles behind the maximum lift coefficient remain unexplored. Hence, the design topology of the maximum lift coefficient is dealt within the following Sections. Initially, the various definitions of  $C_{L_{\max}}$  together with a general mission requirement for an airliner are presented. This will lead to the need for  $C_{L_{\max}}$  in high-lift conditions. Finally, the effects of  $C_{L_{\max}}$  on the overall design process of an aircraft are discussed.

### 2.2.1. DEFINITION

This thesis focuses on the prediction of the maximum lift coefficient of an aircraft. However, the definition of this performance indicator is yet to be introduced. Hence, the following will give a definition of the maximum lift coefficient, which is regularly used throughout this thesis.

Figure 2.3 (left) depicts the lifting behavior of an aircraft with increasing angle of attack. Here, one can observe that the lift coefficient increases linearly with increasing angle of attack  $\alpha$ . The lift coefficient is a number that aerodynamicists use to model all of the complex dependencies of shape, inclination, and flow conditions on the lifting capabilities of an aerodynamic body. This linear behavior is halted when the aircraft goes into a stall. Here, the air flow over the wing starts to separate from the upper surface of the wing. Increasing the angle of attack further aggravates this separation; this leads to a reduction in the rate at which lift increases. I.e.  $dL/d\alpha$  in the left side of Figure 2.3 reduces with increasing inclination angle  $\alpha$  when stall initiates. At a certain point, the rate at which lift increases with angle of attack reduces to zero. This exact point defines the maximum lift coefficient since the maximum lifting capability of a lifting body is reached at this point [19]. This maximum lift point is designated by the dashed line at the peak of the lift polar on the left side of Figure 2.3.

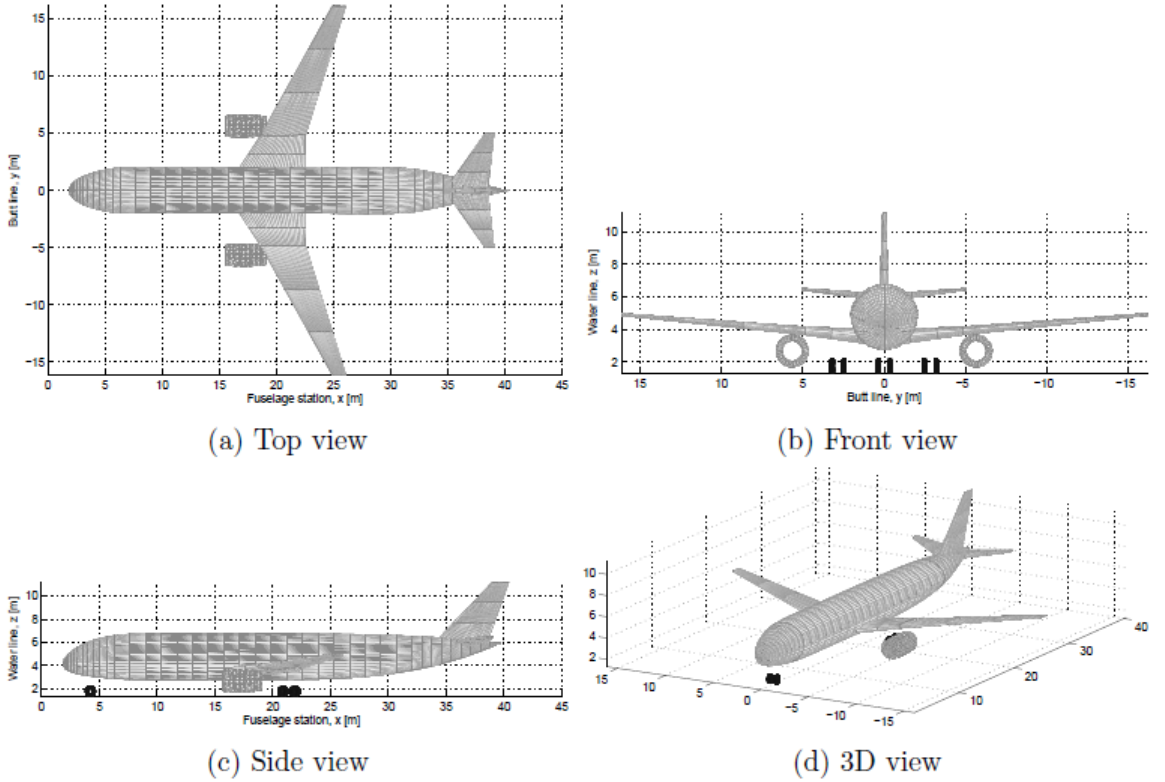


Figure 2.2: Initiator's computed aircraft geometry for the Airbus A320-200 (all dimensions in meters)

Increasing the angle of attack beyond the stall angle leads to the total breakdown of the lifting capabilities of an aircraft since the flow on the upper side of the wing is now completely separated. This goes hand-in-hand with an increase in drag and a distortion of the aircraft's moment balance as can be seen on the right side of Figure 2.3. Here, the tailplane creates a corrective nose-down pitching moment to reduce the angle of attack during stall. This starts a hysteresis loop (depicted on both sides of Figure 2.143) to recover the aircraft from stall [19].

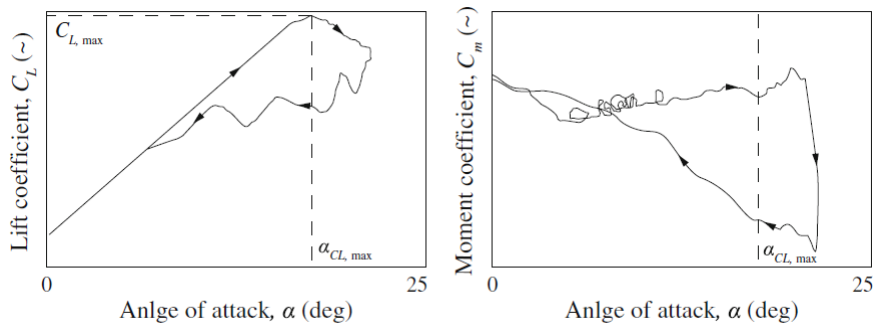


Figure 2.3: Typical stalling pattern for a passenger aircraft during flight. Data obtained from the work of Fischenberg and Jategaonkar as cited in (Vos and Farokhi [19]) for a Dornier 328. (left) Lift coefficient. (right) Moment coefficient

A qualitative definition of the maximum lift coefficient was presented. However, many abbreviations of the maximum lift coefficient are interchangeably used among aircraft designers and within the open literature. Therefore, the three definitions commonly used in aircraft design are presented.

The most common abbreviation is the maximum lift coefficient of an aircraft in steady rectilinear flight. This parameter is labeled as  $C_{L_{\max},1-G}$  and is the true maximum lift coefficient in a physical sense [3]. This measure for maximum lift determines the minimal steady flight speed at a given aircraft weight [3]. Therefore, the  $C_{L_{\max},1-G}$  abbreviation is inherently involved in aircraft design and is used interchangeably with the commonly known  $C_{L_{\max}}$  abbreviation for maximum lift coefficient.

Another abbreviation for maximum lift coefficient used by aircraft designers is  $C_{L_{\max,T-O}}$  (where T-O stands for tail-off). This is the maximum lift coefficient of the aircraft without a tail plane in steady flight. This is a measure of the maximum lift coefficient that is commonly utilized in the writing of this thesis.

The third abbreviation commonly used is the maximum lift coefficient at the minimum speed which, is measured in a stall manoeuvre  $C_{L_{\max,V_{\min}}}$  [3]. This is a measure often used for certification purposes which are regulated by the Federal Aviation Authority (FAA) and European Aviation Safety Agency (EASA).

Also, it is essential to distinguish between wing maximum lift and wing maximum usable lift. The maximum lift of the wing alone may be significantly modified by the presence of interference effects due to fuselages, nacelles, pylons, flap track fairings or other external additions to the configuration. Moreover, maximum usable lift may be limited by other effects associated with flow separation, such as pitch-up, buffet, or wing rock. For example, prior to the attainment of maximum lift it is often the case that the pitching moment curve is characterized by a pitch break, resulting in what can be a very marked and unacceptable change in longitudinal stability [20].

### 2.2.2. MISSION REQUIREMENTS

The design process of an aircraft usually starts at defining top-level design requirements. The most prominent of these requirements are the payload, cruise speed and the range the aircraft can cover. Hereby, the range is defined as the distance traveled between take-off and landing. Between these two phases of a flight, the aircraft follows a specific mission profile within the specified range. This can be seen in Figure 2.4, here it can be deducted that the cruise is the most prominent part of an aircraft's mission. Therefore, preliminary aircraft design processes mainly focus on cruise performance to construct a payload-range diagram and determine the fuel usage [21]. Likewise, the Initiator performs an extensive analysis and design routine to size the aircraft for cruise conditions.

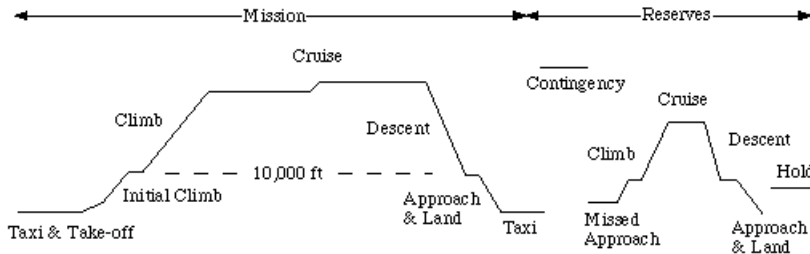


Figure 2.4: Typical flight profile of an airliner

The flight profile of Figure 2.4 also depicts the landing and take-off profiles. The present research aims to extend the design capabilities of the Initiator regarding take-off and landing performance since it has a large impact on the initial wing design, aircraft weight and airfield performance. For example, the landing procedure is depicted in Figure 2.5. Herein, the landing procedure is initiated at an altitude of 50ft. During this approach, the aircraft flies at an approach speed  $V_A$  and at a flight path angle  $\gamma_a$ . This is continued until the aircraft initiates a flaring procedure by pulling the aircraft's nose up. Hereby, the climb rate is decreased until touchdown. From this point onward, the aircraft utilized all the available braking mechanisms to reach a standstill. Until the aircraft reaches a full standstill, a distance is covered which ideally is brought to a minimum. This distance is not only dictated by the used breaking mechanisms but also the approach speed  $V_A$ . This approach speed is essentially the stalling speed of the aircraft multiplied by a safety factor. From Equation 2.1, we can deduct that the stall speed highly influenced by the aircraft's maximum lift coefficient and

surface area in landing. Hence, to enable a correct airfield performance within the Initiator, a proper estimate of  $C_{L_{\max}}$  both in clean and high-lift condition is required.

$$V_{\text{stall}} = \sqrt{\frac{W_{\text{Landing}}}{1/2\rho S C_{L_{\max}}}} \quad (2.1)$$

The mentioned take-off and landing performances are essentially the airfield performance of an aircraft [21]. The airfield performance is regulated by the European Aviation Safety Agency and the US Federal Aviation Regulations (FAR) where the specifications of transport aircraft is documented in Certification Specification 25 (CS-25) and amendment 25-120 respectively [3]. An example of the mentioned airfield performance requirements is conveniently summarized by van Dam [4], see Table 2.3.

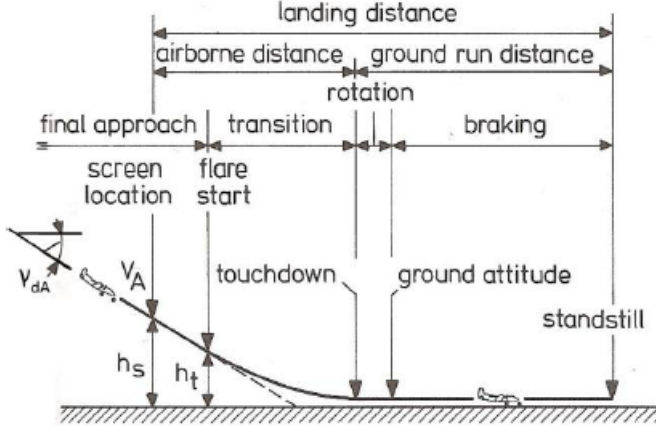


Figure 2.5: Typical landing procedure

Table 2.3: Airfield performance requirements for take-off and landing [4]

Landing	Take-off
$V_A$	$\tan(\gamma) \geq 0.024(3E, OEI)$
$\tan(\gamma) \geq 0.032(AEO, GD)$	$\tan(\gamma) \geq 0.027(3E, OEI)$
$\tan(\gamma) \geq 0.021(2E, OEI, GU)$	$\tan(\gamma) \geq 0.03(4E, OEI)$
$\tan(\gamma) \geq 0.024(3E, OEI, GU)$	$V_1 \geq V_{MC}$
$\tan(\gamma) \geq 0.027(4E, OEI, GU)$	$V_2 \geq 1.13 V_{S_{lg}}$ $V_2 \geq 1.10 V_{MC}$ $V_R \geq V_1$ $V_R \geq 1.05 V_{MC}$ $V_{LOF} \geq 1.10 V_{MU}(AEO)$ $V_{LOF} \geq 1.05 V_{MU}(OEI)$

### 2.2.3. THE NEED FOR HIGH-LIFT DEVICES

In the previous Section, the mission profile of an airliner was illustrated and the airfield performance was introduced. We also saw that the low-speed maximum lift coefficient is inherently involved in the airfield performance of an aircraft and that it dictates the required runway length for landing and take-off. This Section will elaborate on the need of high-lift devices and their impact on the optimal airfield- and cruise performance of an airliner.

To understand the need of high-lift devices, one needs to understand the historical development of the design of an aircraft's wing. Wing sweep at high speeds was first investigated in Germany as early as 1935 [3]. Continuous development and research on swept wings revealed that the shock waves occurring on the suction side of a swept wing, which are prevalent in transonic flow, were postponed to higher Mach numbers. This development made the swept wing a prerequisite for any modern aircraft developed for transonic flight

since airliners were now capable of increasing the cruise Mach numbers while still being economical. Due to this, wings with smaller wing areas and high wing loadings to reduce wing drag and fuel consumption during cruise became the norm of any transport aircraft.

However, the introduction of swept wings had an adverse effect on the achievable lift coefficients in landing and take-off. This led to difficulties in meeting airfield performance requirements. As a consequence, high-lift devices were required to temporarily alter the wing geometry during take-off and landing to obtain higher lift coefficients [3].

Due to this, it became clear that a wing optimized for cruise flight might not meet the airfield performance requirements, which are dictated by for example the EASA and FAA. To obtain a better insight in this, van Dam [4] utilized the Bréquet range equation, see Equation 2.2, to compare the aerodynamic efficiency of two different wings. One wing being optimized for cruise and the other for take-off and landing. Table 2.4 presents the results found by van Dam. It is evident that the aircraft optimized for take-off and landing performance (Aircraft B) yielded a much lower wing loading than Aircraft A. However, this went hand-in-hand with an increase in drag in cruise operation, which results in a reduction in range when Equation 2.2 is utilized. Therefore, the implementation of high-lift devices poses a solution to the prevalent compromise between cruise- and airfield performance efficiency.

$$R = \frac{V_\infty}{C_T} \frac{L}{D} \ln\left(\frac{W_t}{W_e}\right) \quad (2.2)$$

Table 2.4: Comparison of two wings, one optimized for cruise (Aircraft A), and one for take-off and landing (Aircraft B) at  $M_\infty = 0.8$  [4]

Performance Indicator	Aircraft A	Aircraft B
$C_{L_{max}}$	2.34	1.2
$C_L$	0.52	0.27
$C_{LA}$	1.55	0.79
$V_A$	145 knots	145 knots
$M_\infty \frac{L}{D}$	14.4	11.8
$(\frac{W}{S})_{TO}$	147 lb/ft <sup>2</sup>	75 lb/ft <sup>2</sup>
$(\frac{W}{S})_{Landing}$	110 lb/ft <sup>2</sup>	56 lb/ft <sup>2</sup>

The working principles and related aerodynamics of these high-lift devices are thoroughly discussed by both Smith [22] and Rudolph [23]. In general, modern high-lift devices can be classified in two different types. One being leading-edge devices and the other trailing-edge devices. Figure 2.6 illustrates the effects of deploying selected high-lift devices on the achievable lift coefficient and Figure 2.7 displays the geometries of widely used high-lift devices. From Figure 2.6, it is evident that deploying a slat does not generate more lift at a fixed angle of attack. Instead, slats postpone flow separation by lowering the suction peak on the main airfoil [3]. Therefore, the stall angle of attack becomes significantly higher which increases the usable maximum lift coefficient. On the other hand, deployed trailing-edge high-lift devices cause an upward movement of the lift polar as can be seen in Figure 2.6. The main reason for this is due to an increase in the effective chord if Fowler motion is present and an increase in a wing section's camber. Figure 2.6 also depicts an increase in maximum lift coefficient when the number of trailing-edge elements increases. This seems favorable at first, but increasing the number of high-lift elements yields higher system weight and complexity which need to be taken into account when designing an economically viable aircraft.

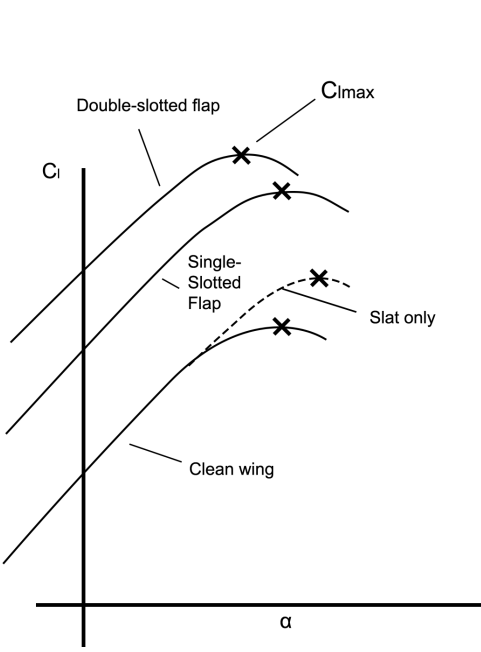


Figure 2.6: Effects on the lift polar by deploying selected high-lift devices [23]

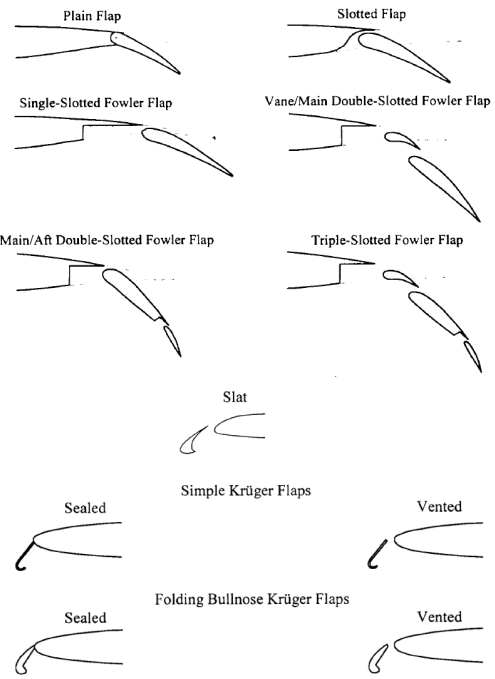


Figure 2.7: Commonly used high-lift devices and their geometries [24]

#### 2.2.4. DESIGN PRINCIPLES OF THE MAXIMUM LIFT COEFFICIENT

The mission profile and the need of high-lift devices are now apparent. However, it is still unclear how the maximum lift coefficient dictates the design of an aircraft. To understand this, one firstly needs to understand the conceptual design process of an aircraft. Herein, one is searching for the optimal thrust- and wing loading combination that meets the mission performance requirements. Hereby, the thrust loading is the ratio of the aircraft's thrust and loaded weight and the wing loading is the ratio between the loaded weight of the aircraft divided by the area of the wing. The optimal combination of these ratios will yield the lowest weight and cost. To achieve this, the highest possible wing loading and lowest possible thrust loading are desirable.

The reason for this is that a lower thrust loading is on par with a smaller engine. This has favorable consequences on the cost, weight and fuel consumption of the aircraft. Similarly, a high wing loading at a given value for aircraft weight implies a smaller wing. Again, beneficial consequences follow in terms of cost and weight of the aircraft as a whole. Also, a high wing loading includes benefits in cruise because a smaller wing (at a given lifting capability) generates less friction drag, which reduces operational costs.

Figure 2.8 depicts a typical wing loading vs thrust loading diagram for an airliner. Herein, it becomes evident that the optimal combination of the thrust loading and wing loading (the solution space) is actually constrained by requirements that are generated by the different phases of the mission profile. Hence, implementing the highest possible wing loading and lowest possible thrust loading yields an unfeasible design. The mentioned constraint are analytically derived by preliminary design strategies. For example, the *Landing* constraint is dictated by the stalling speed of the aircraft, see Equation 2.3. Here it is evident that the stalling speed is a function of both the wing loading and maximum lift coefficient at a given altitude.

$$V_{\text{stall}} = \sqrt{\frac{W}{S} \frac{2}{\rho} \frac{1}{C_{L_{\max}}}} \quad (2.3)$$

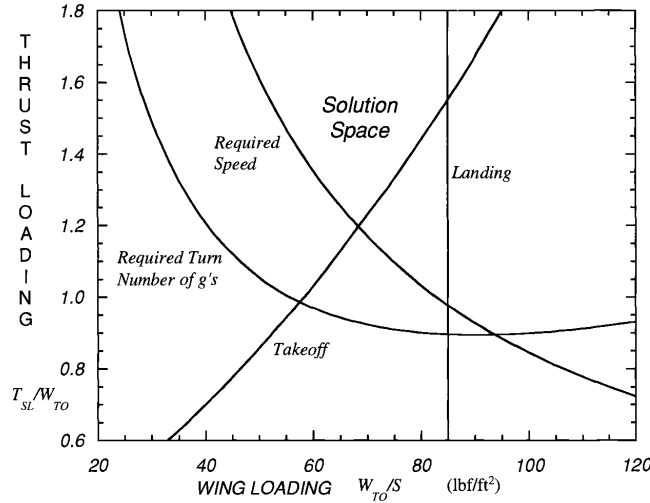


Figure 2.8: Typical constraint in a wing loading vs thrust loading diagram

Figure 2.9 displays a carpet plot of Equation 2.3 and illustrates how the wing area is affected by the maximum lift coefficient. Here, the Figure displays the regulatory FAR 23 stall speed limit of 61 KCAS for single-engine aircraft as an example. To meet this requirement the designer can either increase the maximum lift coefficient, decrease aircraft weight or increase wing area. On this behalf, an optimum between these parameters is required. Increasing the maximum lift coefficient is often done by implementing increasingly complex high-lift devices. These complex high-lift devices often come with additional weight, cost, maintainability, and are more sensitive to failure due to more implemented parts . Therefore, a compromise between the wing size and high-lift device complexity is required in order to obtain the most efficient aircraft design.

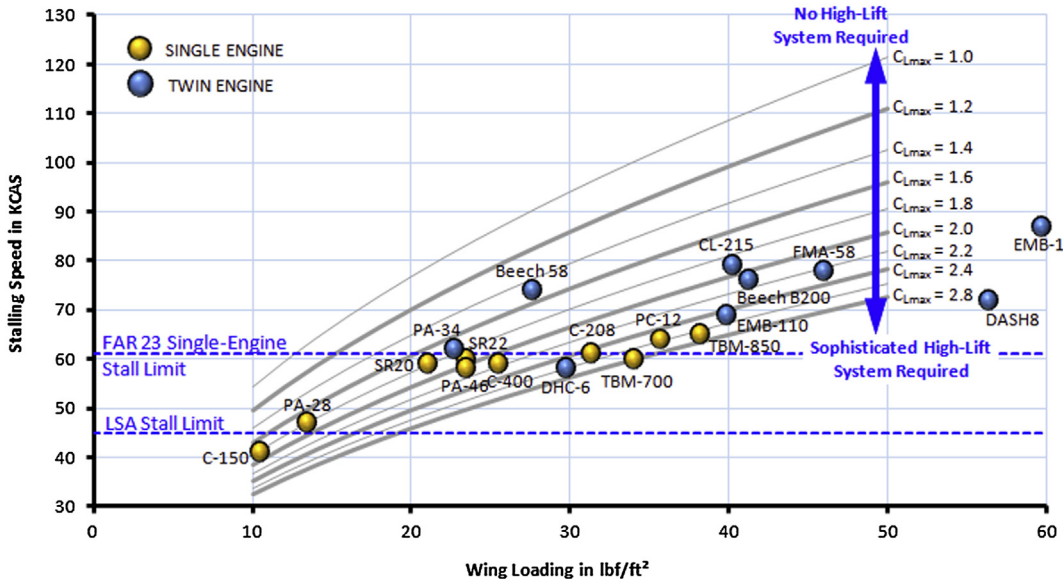


Figure 2.9: A carpet plot showing stalling speed as a function of wing loading and maximum lift coefficient for landing configuration at gross weight and standard sea level density

## 2.3. FLOW PHYSICS AT MAXIMUM WING LIFT

This section presents a broad overview of the viscous flow phenomena that collude with low-speed stall for both three- and two-dimensional lifting surfaces. Initially, the definition of stall is discussed. This is followed by a discussion on the stalling characteristics of both three- and two-dimensional lifting surfaces. Subsequently, the flow physics surrounding high-lift devices are presented. Finally, experimental Mach- and

Reynolds number versus maximum lift coefficient trends are examined.

### 2.3.1. DEFINITION OF STALL

In Section 2.2, the topology around the maximum lift coefficient was discussed. Here, the definition of maximum lift coefficient was denoted as a phenomena that is related to aircraft stall. However, the exact definition and working mechanisms of stall were omitted. Hence, the remainder of this Section will elaborate further on the definition of stall and will give a concise overview of the associated working principles.

The mechanisms of stall, in low-speed and high-speed flight, are somewhat identical. This is the case since stall is always the results of boundary layer that separates from a lifting-surface. Hereby, the boundary layer is a small viscous layer of fluid that is close to the surface of for example a wing. This boundary layer dictates the significant viscous effects, which include the generation of drag by a lifting surface but also the maximum lift coefficient. Figure 2.11 gives a graphical representation of a boundary layer around an airfoil alongside the different states in which the boundary layer can manifest.

At small angles of attack, the viscous flow around a lifting object is attracted to the curvature of a a surface. This attraction is labeled as the Coandă effect after Henri Coandă. This researcher identified that to turbine air was attracted to adjacent surfaces [19]. This effect was the cause of a fluid entertainment. Fluid entertainment is effectively a phenomenon where a jet of air moves through ambient air where the ambient are is pulled inward towards the jet. However, for the case of a lifting-surface, a wall retards this movement, therefore, the jet of air accelerates over the lifting-surface. Due to this, an effective pressure distribution is created over the lifting-surface due to the principles of Bernoulli [19].

Figure 2.10 depicts a typical pressure distribution over an airfoil. Here, the pressure coefficient decreases until the point of maximum airfoil thickness is reached and a suction peak is realized. Downstream of the suction peak, the pressure rises due to an adverse pressure gradient in the streamwise direction. Due to this, the Coandă effect diminishes. Also, the boundary-layer momentum reduces and reverse flow within the boundary layer initiates [19]. The conjunction of these phenomena marks the initialization of boundary layer separation. When the angle of attack is increased further, the strength of the adverse pressure gradient increases and the boundary layer separates and a full stall is achieved. This separated boundary layer steeply increases the drag due to the turbulent wake, which leaves the trailing edge of the airfoil, as can be seen in Figure 2.11.

Hence, stall is nothing more than a boundary layer that leaves the surface of an aerodynamic object. The separating of the boundary layer is affected by several geometrical and physical effects. Therefore, the following sections will address these effects accordingly.

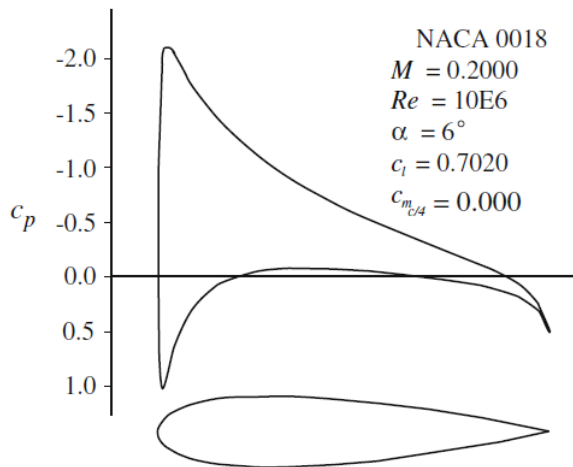


Figure 2.10: Typical pressure distribution over the NACA 0018 airfoil as computed by XFOIL

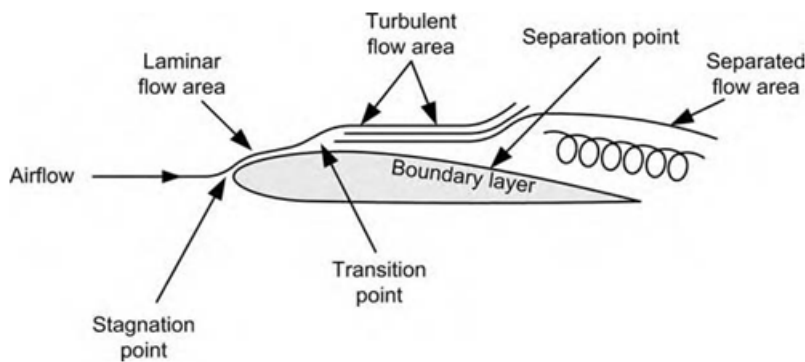


Figure 2.11: Manifestation of several states of a boundary layer around an airfoil

### 2.3.2. TWO-DIMENSIONAL SECTION STALLING CHARACTERISTICS

To start relatively simple, the stalling mechanisms of two-dimensional wing sections are discussed. McCullough and Gault [25] conducted an extensive research on different types of airfoil stall. Herein, they investigated the stall phenomenon on five symmetrical airfoil by testing them in the 7- by 10-foot wind tunnel of National Advisory Committee for Aeronautics (NACA). Their research revealed that the airfoil stall can be distinguished in three main types and one combination of stall mechanisms:

- **Trailing-edge stall** This type of stall is often found on thick airfoil sections having a  $t/c > 0.15$ . Trailing-edge stall has a continuous force variation with a well-rounded lift curve, even beyond the point of stall. This type of stall originates from a steady movement of the turbulent boundary-layer separation point toward the leading edge. A graphical representation of this stall type can be found in Figure 2.13a.
- **Leading-edge stall** This type of stall is generally inherent to airfoil sections that have a moderate thickness ( $0.09 < t/c < 0.15$ ). This stall type is often characterized by a lift curve slope that has no changes prior to stall. As stall initiates, an abrupt (often large) decrease in lift after maximum lift is generated. This type of stall originates due to the presence of a laminar separation bubble (of very small chordwise extent, typically  $0.005c$  to  $0.01c$ ) just aft of the suction peak. This bubble is created when the boundary layer is not able to cope with a large pressure gradient, which follows after a suction peak. As incidence angle is increased, the bubble moves towards the leading edge until it eventually bursts causing full chord flow separation. Figure 2.13b gives a graphical representation of this leading-edge bubble. The formation of the separation bubble is dictated by the nose radius of the airfoil, effective Reynolds number, surface roughness and effective angle of attack [26].
- **Thin-airfoil stall** This type of stall is often found on airfoils that have a sharp leading edge or on very thin airfoils ( $t/c < 0.09$ ). Often a rounded lift curve peak is realized. The physics behind this stall type is due to a laminar separation bubble. This bubble starts at the leading edge and re-attaches in the vicinity of the separation point. However, when the incidence increased, the re-attachment point moves towards the trailing edge until it coincides with the trailing edge. Hence, when it reaches the trailing edge, the entire flow over the airfoil is separated and the maximum lift is reached. The long bubble is represented by the dotted region in Figure 2.13c.
- **Combined trailing-edge and leading-edge stall** The airfoil in these cases exhibits the types of separation typical to both the leading- and trailing-edge stall. The shape of the lift polar at the maximum lift coefficient depends on the dominance of stalling type. The lift polar contains a gradual decrease in lift if the trailing turbulent flow type of stall dominates. The opposite is true if the leading-edge stall is the most prominent. A graphical representation of this stall type is presented in Figure 2.13d and typical lift polars representing this stall type are depicted in Figure 2.12. This stall type often sets the maximum lift coefficient of an airfoil as this type of stall often occurs in practical cases.

As mentioned before, the boundary layer effectively separates predominately due to a prevalent adverse pressure gradient. Therefore, the discussed stall types are each associated to a typical pressure distribution at stall. Figure 2.14 illustrates typical pressure distributions at various angles of attack until the onset of boundary layer separation. Just prior to total flow breakdown, the airfoil experiences a local flow separation. This

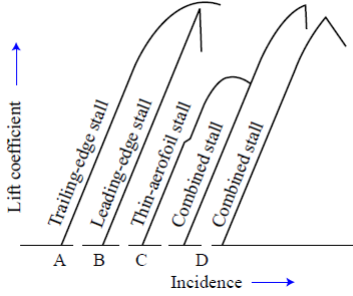


Figure 2.12: Typical lift polar at various stall types [27]

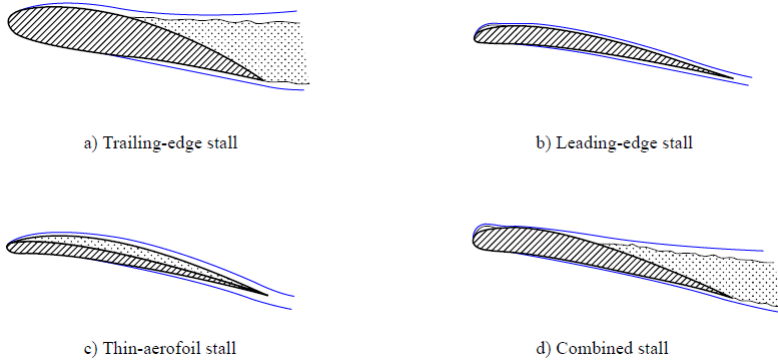


Figure 2.13: Flow characteristics of an airfoil at various stall types [28]

can be seen in Figure 2.14 as a local horizontal line on the trailing edge of the airfoil. This implies that the flow is detached from the airfoil surface. Therefore, no change in pressure can exist. Increasing the angle of attack further moves the point of separation upstream and stall is reached. From Figure 2.14 it is apparent that the suction peak collapses at stall onset. Also, a rapid increase in drag is realized as can be seen from the drag polar. Figure 2.15 depicts a similar schematic for a leading-edge stall. Again, the drag is rapidly increasing at this sudden stall. As can be seen, this type of stall is associated with a very peaky suction peak that increases with inclination angle. At stall onset, a rapid collapse of the suction peak follows. The magnitude of this collapse is apparently greater for this leading-edge type of stall when compared to the trailing-edge stall.

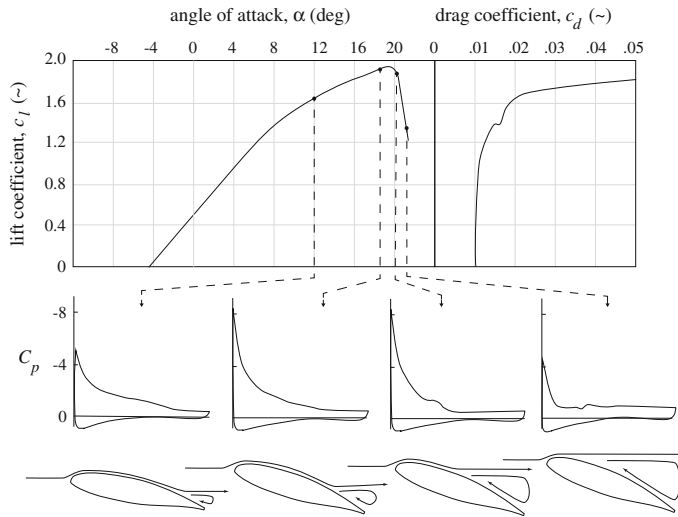


Figure 2.14: The lift and drag curves along side typical pressure distributions at various angles of attack for trailing-edge separation with associated upper-surface stream line at  $Re = 6.3 \cdot 10^6$ ,  $M = 0.15$ . Data obtained from McGhee and Beasley as cited in (Vos and Farokhi [19] )

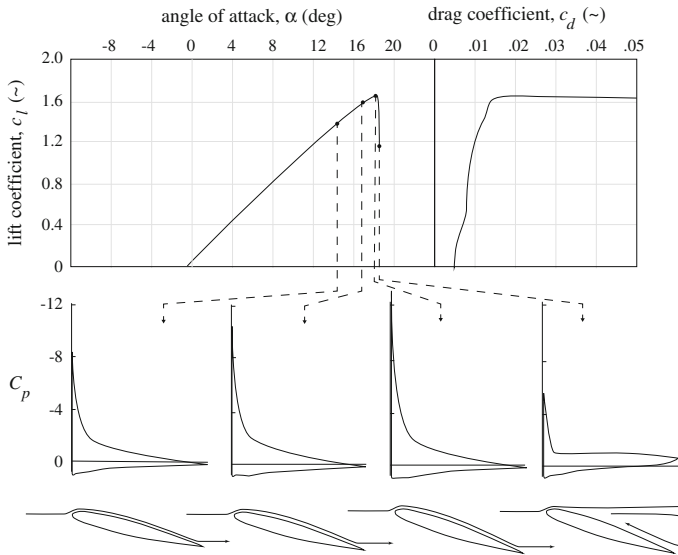
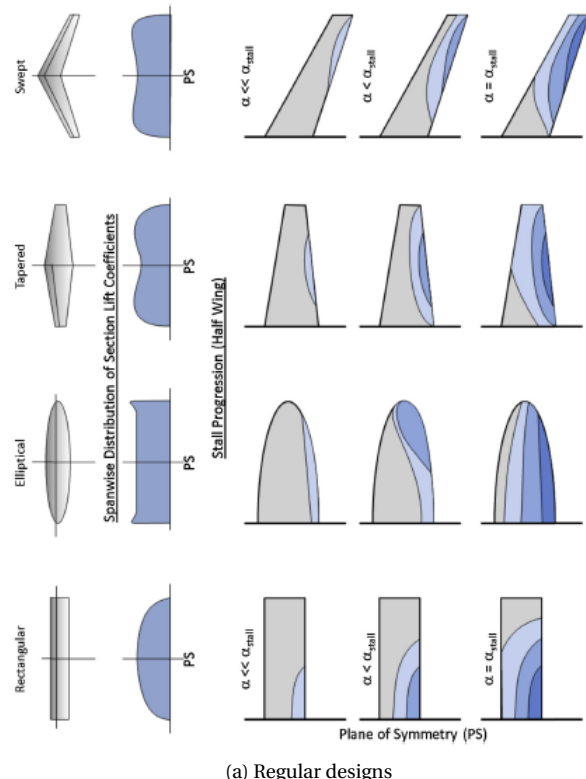


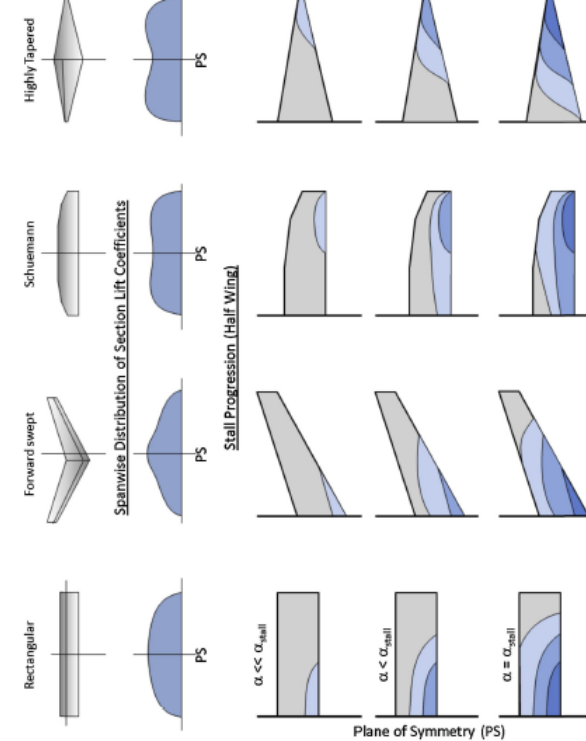
Figure 2.15: The lift and drag curves along side typical pressure distributions at various angles of attack for leading-edge separation with associated upper-surface stream line at  $Re = 4.0 \cdot 10^6$ ,  $M = 0.17$ . Data obtained from Maki and Hunton as cited in (Vos and Farokhi [19] )

### 2.3.3. THREE-DIMENSIONAL VISCOUS FLOW PHENOMENA

At this point, the stall phenomena pertaining two-dimensional wing sections have been discussed. However, these sections pertain to an actual position along the wing span of a finite three-dimensional wing. Due to this, the previously mentioned stall types are affected by three-dimensional effects. These three-dimensional effects are, among others, a function of a wing's planform shape. Hereby two-dimensional stall can be countered or even be aggravated depending on the wing geometry. Therefore, the relation between the wing planform and related wing stall is of utmost importance to determine the maximum lift coefficient of a wing. Gudmundsson [10] presented a graphical illustration of different stall phenomena for several planform types, as can be seen Figure 2.16a and Figure 2.16b. A favorable stall pattern should always begin at the wing root and progress toward the tip when the angle of attack is increased. This ensures that the wingtips will be the last part of the wing to stall, which provides essential maneuverability during a full aircraft stall. Hence, highly tapered wings should be avoided. This can also be concluded from Figure 2.16b.



(a) Regular designs



(b) Exotic designs

Figure 2.16: Illustration of boundary layer separation on various wing geometries during a three-dimensional stall. The dark blue regions represent separated flow [10]

The mentioned three-dimensional aerodynamic effects have been discussed thoroughly by Harper and Maki [29], Obert [3] and, Furlong [26]. To summarize their work, the following key three-dimensional effects that dictate the stall of a swept wing can be distinguished:

- Spanwise boundary layer flow due to the existence of a spanwise pressure difference.
- A spanwise induced camber which alters the effective camber of the local wing sections.
- Leading-edge vortex shedding on highly swept wings with a sharp leading edge at the wing root.
- The generation of a spanwise induced angle of attack due to the formation of counter-rotating vortices at the wing tips.

These key three-dimensional effects are to be fully understood if one wished to build a tool to predict a wing's maximum lift coefficient. Therefore, these prevalent three-dimensional effects are briefly discussed in following.

#### SPANWISE BOUNDARY LAYER FLOW

The current designs of airliners incorporate wing sweep to efficiently cope with transonic flow physics. This wing sweep introduces a staggering in chordwise pressure distribution across the wingspan. Due to this, on any line perpendicular on the plane of symmetry, the pressures on the upper side of the wing become increasingly more negative with an increase in distance towards the wing tip. Therefore, a spanwise pressure gradient between the wing root and wing tip exist as can be seen in Figure 2.17. This induces a spanwise boundary layer flow from root to tip, which has a prevalent effect on swept-wing stall [29].

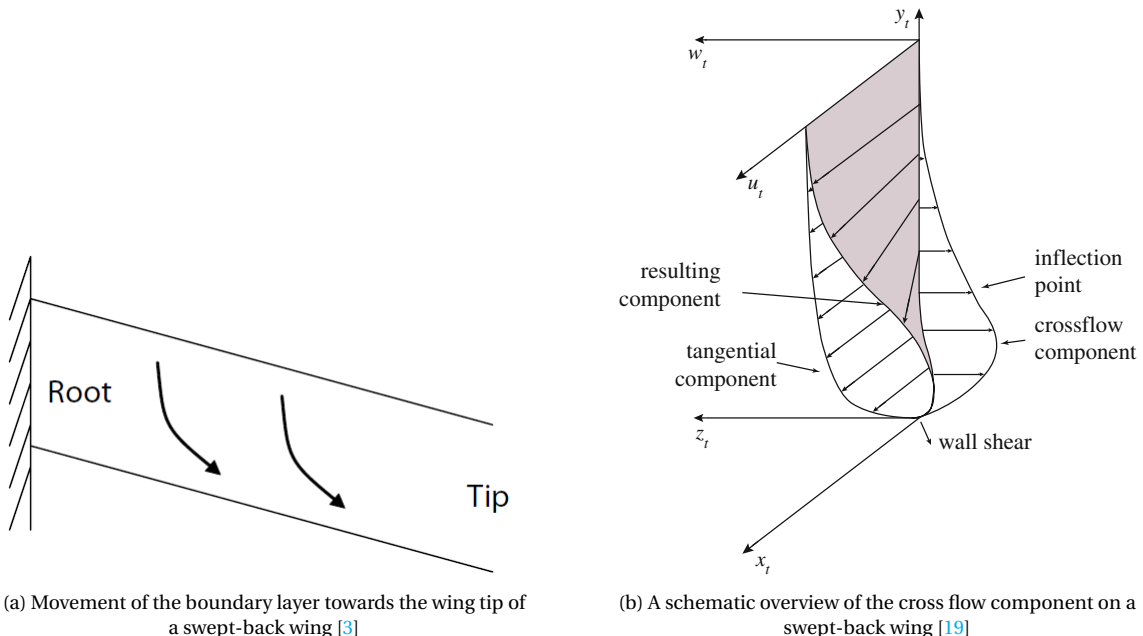


Figure 2.17: Spanwise cross flow over a swept-back wing

This spanwise boundary layer flow causes a variation in local spanwise boundary layer thickness where the inboard boundary layer is significantly thinner than the outboard boundary layer. This thickening of the boundary layer alters the effective shape of the local wing section. This is labeled as decambering, which leads to changes in local pressure distribution and a shift in aerodynamic center. Also, thicker boundary layers have less momentum close to the wall and therefore tend to separate more easily than thin boundary layers under an adverse pressure gradient [19]. This feature has therefore significant effects on various local aerodynamic parameters such as the achievable local  $c_{l_{\max}}$ , the local lift curve slope, effective chordwise

pressure distribution and the initiation and progression of stall. The magnitude of these effects depends significantly on the amount of wing sweep but also on aspect ratio, taper ratio and local leading-edge radii [29].

The effects of the boundary layer flow have been thoroughly studied by both Harper and Maki [29]. Here, they found that the thinner inboard boundary layer acts as a natural form of stall control. Hereby, they found that the local  $c_{l\max}$  reached higher values when compared to the two-dimensional  $c_{l\max}$  of the local airfoil. This feature is depicted in Figure 2.18.

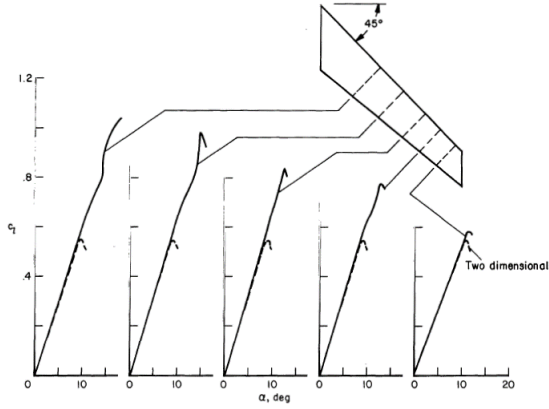


Figure 2.18: Comparison of two- and three-dimensional experimental lift curves of the NACA64A010 section on a  $45^\circ$  swept-back wing [29]

To this extent, Harper and Maki tested several swept-back wings to expose this act of natural boundary layer control. Their results are depicted in Figure 2.19. Apparently, the mentioned natural boundary layer control is aggravated as the sweep is increased. Also, the stall control is more present on wing having a reduced aspect ratio. Similarity, doubling the Reynolds number causes a thinner boundary layer at the wing tip. This thinner boundary layer is able to withstand the adverse pressure gradient and therefore an increased local  $c_{l\max}$  is observed.

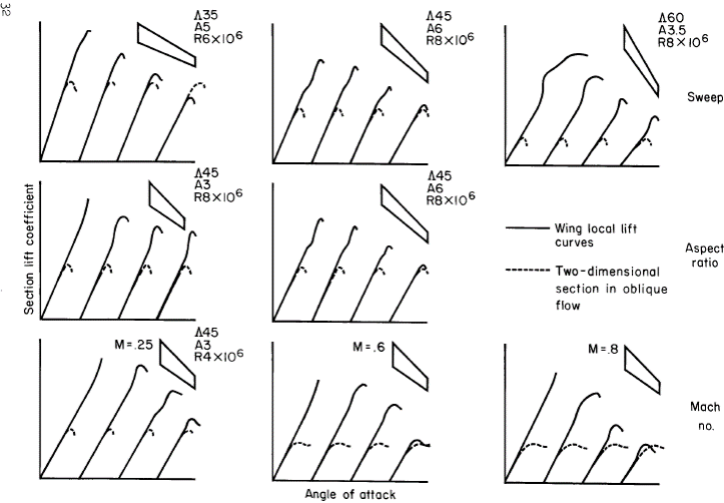


Figure 2.19: Effects of sweep, aspect ratio, and Mach number on the comparison between two- and three-dimensional lift curves [29]

The work of Harper and Maki was not limited to the analysis of local  $c_{l\max}$  values solely. They also scrutinized local pressure distributions on swept wings and compared them to the pressure distributions on equivalent two-dimensional wing sections prior to stall. An example of their observations is illustrated in Figure 2.20.

The two-dimensional pressure distributions shows the typical evidence of both leading- and trailing-edge types of separation. Here, both the loss of the sharp leading-edge peak and a lack of recovery at the trailing edge are observed. Pressure distributions for several stations on the span of the swept wing indicate the same type of separation pattern over the outboard part of the span. However, the inboard stall type changes to the thin airfoil, leading edge type of separation. From this it can be judged that the boundary layer control is increasingly effective for the trailing edge type of separation as the stations are nearer to the root. An equivalent analysis was conducted on the same wing with  $60^\circ$  back sweep. Here, Harper and Maki found that the local wing sections only showed leading-edge separation prior to section maximum lift. It appeared that the boundary layer control intensified at the trailing edge of the wing with increasing sweep angles.

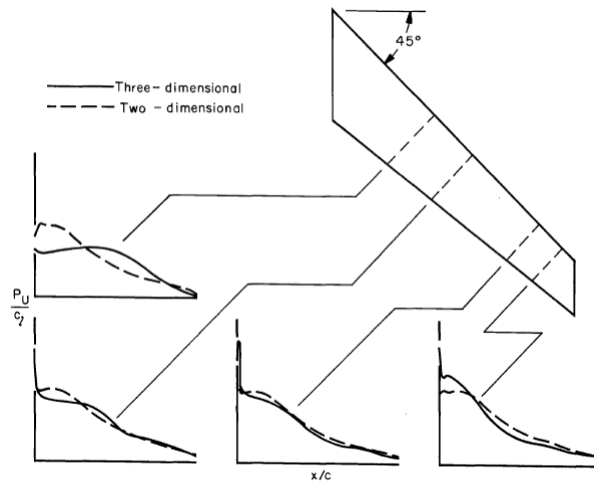


Figure 2.20: Comparison of two- and three-dimensional experimental pressure distributions at  $c_{l_{\max}}$  for the NACA64A010 airfoil [29]

#### LEADING-EDGE VORTEX SHEDDING

Occasionally a leading-edge canonical vortex is established, which is perpendicular to the leading-edge of a thin swept wing with a sharp leading edge. This vortex traverses over the upper surface of the wing and affects the local aerodynamic quantities. This phenomenon can be seen in Figure 2.21 for a swept wing with  $48^\circ$  leading-edge sweep. The diameter of the canonical vortex effectively increases towards the wing tip. This happens due to the fact that the vortex contains an accumulation of the dead air that has been drained from the more inboard wing sections. Increasing the geometrical angle of attack of the wing causes the canonical vortex to move to the inboard along the swept trailing-edge [26]

This vortex is instantiated due to both a leading-edge separation bubble and a spanwise pressure gradient that is inevitable on swept wings. Therefore, leading-edge vortices are common on swept wings which incorporate airfoils which exhibit pronounced leading-edge separation bubbles. Hence, the establishment of this vortex is highly dependent on the local Reynolds number, surface roughness and angle of attack.

The main effects of this vortex include an increase in leading-edge suction peak while increasing the local chordwise loading which causes a rearward shift in center of pressure as can be seen in Figure 2.21. The vortex postpones wing stall to higher angles of attack due to the fact that the vortex flow energizes the local boundary layer which allows the flow to cope with stronger adverse pressure gradients [3]. Also, the canonical vortex creates a induced angle of attack along the spanwise wing sections. This has significant effects on the total lift curve slope and local wing section  $c_{l_{\max}}$  [26]. The mentioned increase in local section  $c_{l_{\max}}$  can also be seen in Figure 2.21. Here, the wing sections at  $0.2b/2$  and  $0.4b/2$  show no signs of section stall. The magnitude of the mentioned effects increases with angle of attack and has shown to be more pronounced on wings that have a low aspect ratio.

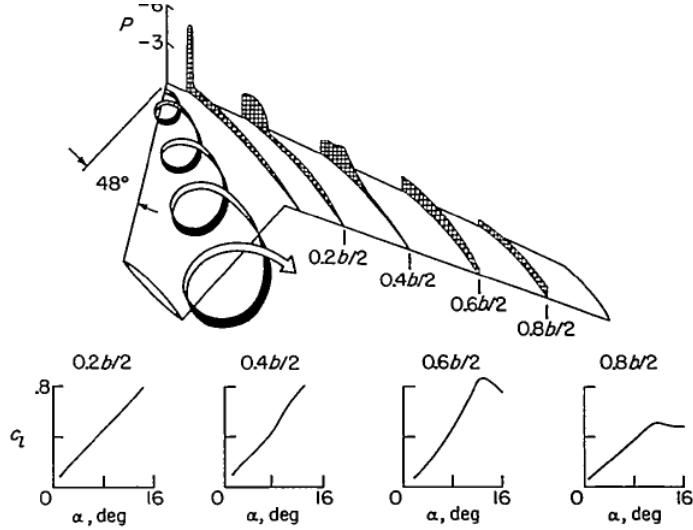


Figure 2.21: Schematic view of a leading-edge vortex flow and the associated effects on the local pressure- and lift distributions of a sweptback wing ( $\Lambda_{c/4} = 45^\circ$ ) of aspect ratio 3.5, which incorporates circular-arc airfoils at  $C_L = 0.67$  [26]

#### SPANWISE INDUCED ANGLE OF ATTACK

For a lifting wing, the air pressure on the top of the wing is lower than the pressure below the wing. Near the tips of the wing, the air is free to move from the region of high pressure into the region of low pressure. The resulting flow is depicted in Figure 2.22 by the two circular blue cones with the vertical arrowheads showing the flow direction. The blue cones represent the counter-rotating vortices that result from the moving air at the wing tips.

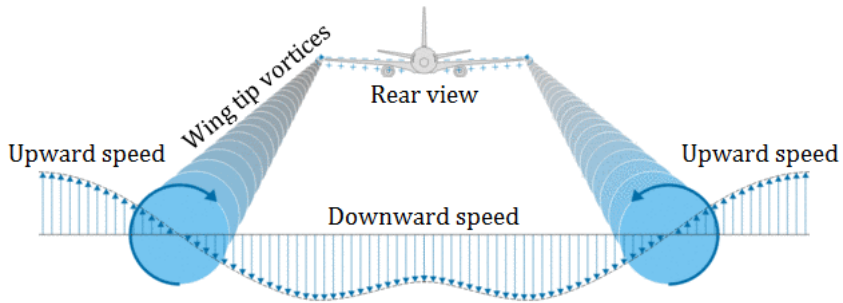


Figure 2.22: Graphical representation of the vortices which are generated at the wing tips with their associated effects on the local downwash velocity

These vortices at the wing tip produce a downwash of air behind the wing that is very strong near the wing tips and decreases toward the wing root. The downwash can also be viewed as the result of the lifting wing "pushing down" on the air, which results in the air having added downward momentum directly behind the wing. In other words, the wing operates in its own downwash. The apparent freestream velocity that the wing 'sees' is therefore tilted by the induced angle of attack. Therefore, the wing operates at an effective angle of attack which is smaller in magnitude. This is illustrated in Figure 2.23 and Equation 2.4. Therefore, the wing stall of a finite wing occurs at a higher geometrical angle of attack when compared to a similar infinite wing.

$$\alpha_{\text{eff}} = (\alpha + \epsilon) - \alpha_i \quad (2.4)$$

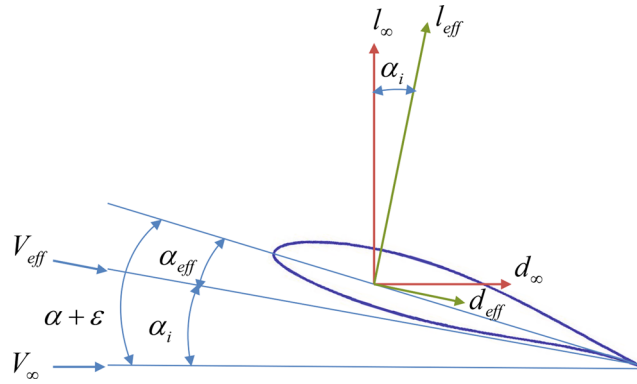


Figure 2.23: Graphical representation of the effects of the induced angle of attack on both the lift- and drag coefficient of a wing section and a representation of  $\alpha_{eff}$  [30]

#### 2.3.4. FLOW PHYSICS OF STALLING HIGH-LIFT CONFIGURATIONS

Previously, the flow separation mechanics of both airfoil sections and wings as a whole have been discussed. However, high-lift devices of course also suffer from stall, which limits their performance. The critical issue here is that high lift devices often consist out of multiple elements. Therefore, stall on a leading-edge device can aggravate stall on the subsequent downstream components. Also, the tendency to reduce downstream pressure peaks is lost when an upstream element of the high-lift configuration stalls. This happens because the effective downwash and upwash change due to a change in the generated circulation on each subsequent element [22].

Obert [3] provides a concise summary of separation phenomena, which are often found on high lift configurations. The following types of stall are common for trailing-edge devices:

- Flow separation may occur at the trailing edge of the flap at relative small angles of attack and large flap deflections. This phenomenon often sets the maximum flap angle. See Figure 2.24 for a graphical representation of this stall type.
- Trailing-edge separation can also occur on the trailing edge of the main wing. This wake of separated flow will influence the boundary layer on the trailing-edge device leading to a decrease of lifting capability on both the main part and trailing high-lift device. Figure 2.25 gives a graphical representation of this.
- Separation can also occur on the leading edge of the main component. This has been discussed before where it was found that this led to an abrupt stall. This decreases the effective downwash which is generated by the main component, therefore, a trailing-edge device becomes more effective because the effective deflection is increased. Hence, the trailing-edge device develops additional suction on the upper surface, see Figure 2.26.

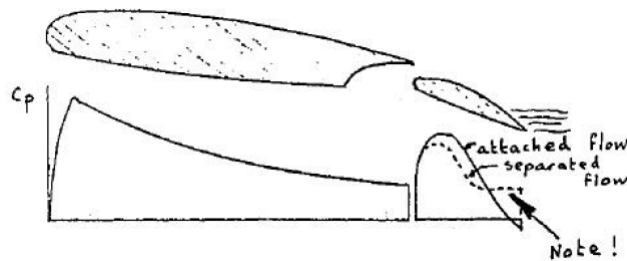


Figure 2.24: Trailing-edge stall on the flap of a two-element high-lift configuration [3]

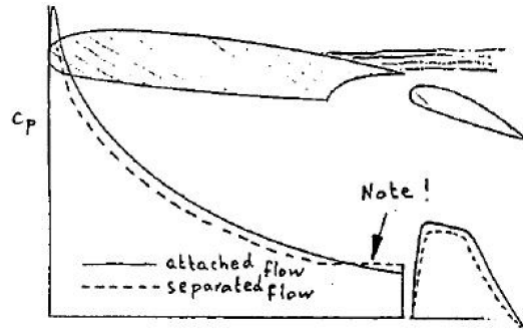


Figure 2.25: Trailing-edge stall on the main component of a two-element high-lift configuration [3]

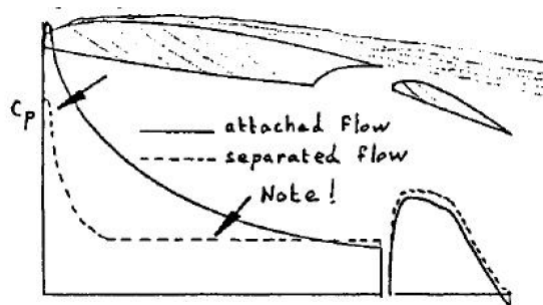


Figure 2.26: Leading-edge stall on the main component of a two-element high-lift configuration [3]

Similarly, Obert [3] also shows the different types of flow separation that may occur on three-element high-lift systems which consists out of a slat, main component and a flap. The stall types which are commonly found on the devices can be summarized as follows:

- Stall can initiate at the leading edge of the slat. This will result in a lower pressure peak on the leading-edge of the slat. This can be seen in Figure 2.27.
- Trailing-edge separation can occur on the main component when the slat angle exceeds the angle where stall will initiate on the slat itself, which can be seen in Figure 2.28.
- Large slat deflection angles can lead to two different types of flow separation. The flow may separate right at the leading edge of the main element resulting in a collapse of the leading-edge suction peak. Or separation can occur at the kink, which is created on the main wing to stow the leading-edge device. This kink acts like a convex surface and will thus create a pressure peak. The different pressure distributions that follow can be seen in Figure 2.29.

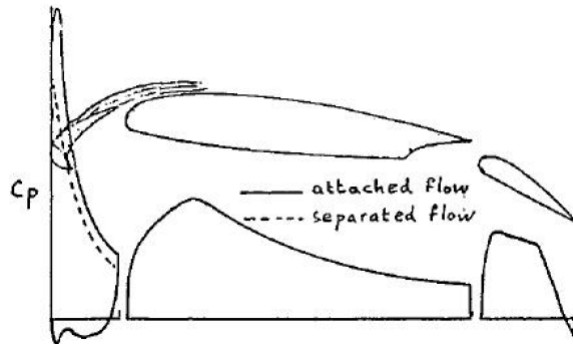


Figure 2.27: Flow separation on the slat of a three-element high-lift configuration [3]

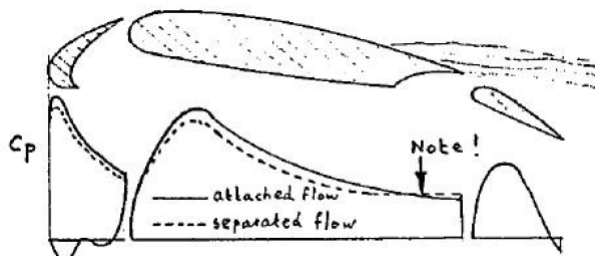


Figure 2.28: Trailing-edge stall on the main component of a three-element high-lift configuration [3]

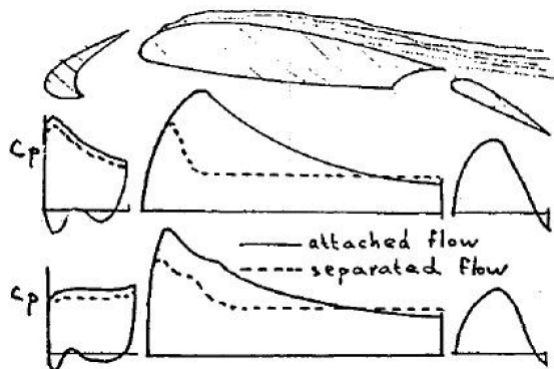


Figure 2.29: Leading-edge stall on the main component of a three-element high-lift configuration [3]

In contrast to single-element airfoils, multi-element airfoils deal with the interaction of various boundary layers and the merging of wakes. This feature can be seen in Figure 2.30, which depicts the Airbus A320 wing in landing configuration with both slat and flap deployed. Here, the dash-dotted lines indicate the edge of the various boundary layers that are formed on this multi-element airfoil. It is apparent that the slat wake merges with the boundary layer of the wing. This phenomenon is labeled as boundary layer confluence [19]. This also happens again over upper surface of the trailing-edge flap. Here, the merging of boundary layer causes reversed flow over the flap which marks the onset of stall. This can be seen at the foot of the combined velocity profile in Figure 2.30. Hence, the proper high-lift configuration design in terms of boundary layer guidance with adequate design of both slots and vanes are of utmost importance to achieve high maximum lift coefficients.

Another aspect that affects the lifting capabilities of multi-element airfoils is the generation of weak shocks on the leading-edge of slats. The nose of the slat often generates relatively high suction peaks due to the up-wash generated by the main airfoil element. Hence, local supersonic flow exists that is often terminated by a shock wave. Here, the shock interacts with the boundary layer, often boundary layer transitions from laminar to turbulent occurs at the foot of the shock. Increasing the Mach number aggravates the strength of the gen-

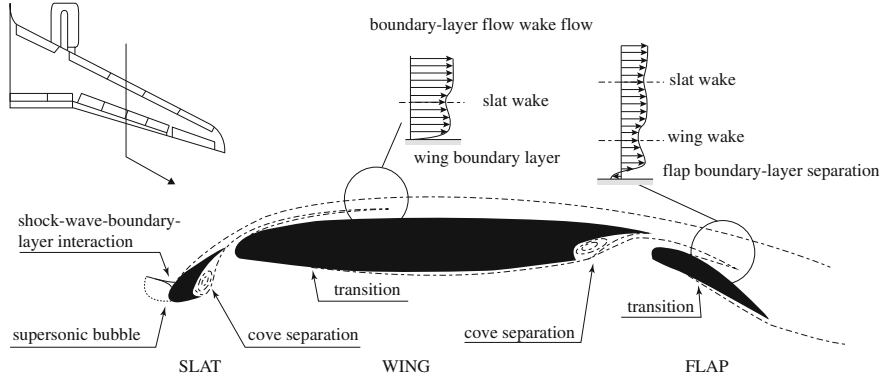


Figure 2.30: The airfoil of the Airbus A320 in landing configuration [19]

erated shock wave, which eventually leads to boundary layer separation at the shock foot. This phenomenon is depicted in Figure 2.30.

Also, high-lift devices often implement coves to efficiently store the devices in the wing during cruise. These coves often see a revered flow due to prevalent adverse pressure gradients that are generated due to rapid changes in local airfoil geometry. Therefore, coves are often subject to boundary layer separation. This reversed flow can be seen in Figure 2.30 on both the slat element and the trailing edge of the main wing element.

### 2.3.5. MAXIMUM LIFT COEFFICIENT EXPERIMENTAL TRENDS

Vos and Farokhi [19] illustrate the effects of Mach number on the section maximum lift coefficient, see Figure 2.31a. Here the research results on six different propeller-powered aircraft of Spreiter and Steffen [31] are displayed for both low-drag airfoils and conventional NACA-4 and 5 series. It is clearly evident that the behavior of maximum lift coefficient with Mach number varies for the considered airfoil types. The NACA-4 and 5 series show a somewhat linear decrease in maximum lift coefficient. In contrast, the low drag airfoils experiences a decrease in maximum lift coefficient initially whereas it slightly increases again around  $M = 0.6$ . Increasing the Mach number further shows detrimental effects on the maximum lift since the low drag airfoils show a very steep decrease post  $M = 0.6$ . This uniform lowering of maximum lift in the subcritical Mach number domain can be attributed to a steepened adverse pressure gradient resulting from compressibility effects. These steepened adverse pressure gradients make it difficult for the boundary layer to traverse its path over the surface. Therefore, the boundary layer flow tends to stall and separate earlier with higher Mach number and thus lower maximum lift coefficients are found. Obert [3] found similar results, which can be seen in Figure 2.31b. He also argues that the decrease in maximum lift coefficient is due to a steepened pressure gradient. However, he also mentions that the decrease in maximum lift coefficient is due to a suction peak that becomes less negative with increasing Mach numbers while the critical pressure coefficient remains unaltered.

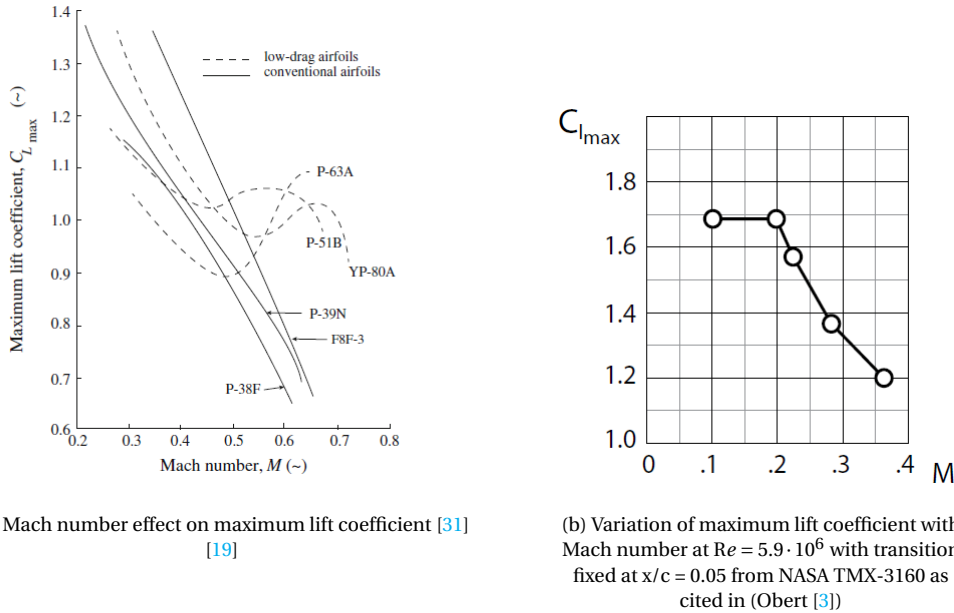


Figure 2.31: The effects of Mach number on the two-dimensional maximum lift coefficient

Also, Obert illustrates the effects of Reynolds number on the course of the maximum lift coefficient. This can be seen in Figure 2.32a. Here, Obert attributed the increase in lift by arguing that the boundary layer becomes thinner, which allows the boundary layer to tolerate larger adverse pressure gradients. Subsequently, higher maximum lift coefficients are reached. Vos and Farokhi [19] also illustrate the effects of Reynolds number on the maximum lift coefficient as can be seen in Figure 2.32b. Here, Vos and Farokhi also relate the increase of maximum lift to the larger adverse pressure gradient tolerance of a thinner boundary layer. However, they also argue that the increase in Reynolds number affects the chord wise position of transition and therefore the separation bubble physics on an airfoil surface. Subsequently, a switch from leading-edge stall to trailing-edge stall might occur as can be seen in Figure 2.32b.

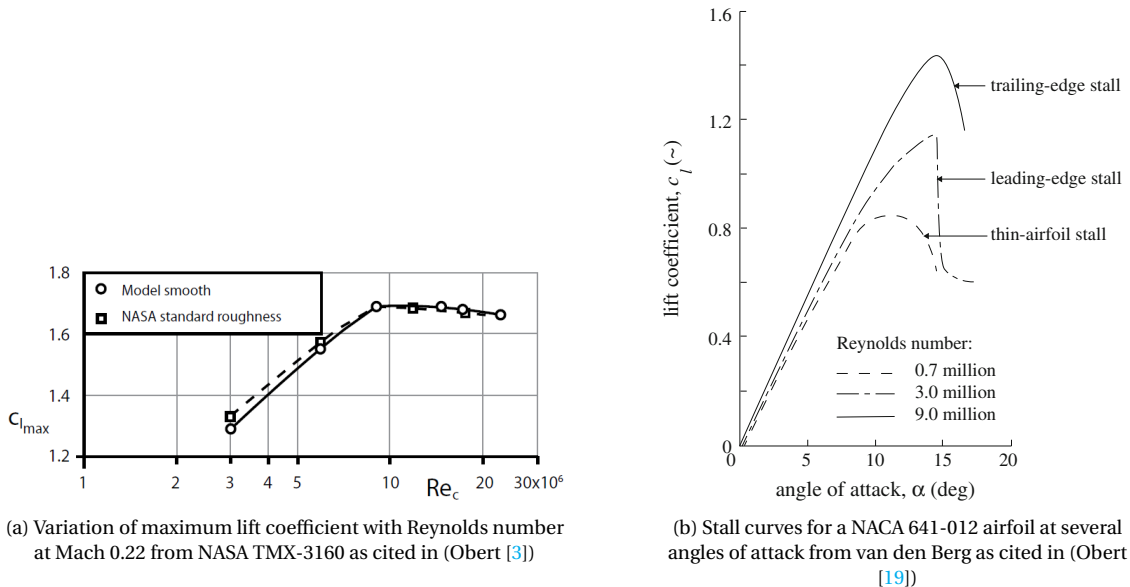


Figure 2.32: The effects of Reynolds number on the two-dimensional maximum lift coefficient

## 2.4. METHODS FOR LOW-SPEED WING MAXIMUM LIFT COEFFICIENT PREDICTION

In upcoming Sections, various methods to predict the tail-off maximum lift coefficient are discussed. These methods are divided between non-linear lifting line theories and (semi)-empirical methods. Next to this, the current state-of-the-art is examined to create a point of reference within this thesis. Subsequently, a trade-off between the various methods to predict the maximum lift coefficient is presented to assess the suitability of these methods with respect to the scope of this thesis.

### 2.4.1. STATE-OF-THE-ART

It is deemed important to first understand the state of the art in the field of maximum lift prediction before an attempt is made to develop a rapid  $C_{L_{\max}}$  prediction method. In 2002, Rumsey and Ying [6] reviewed the current (at that time) capabilities of Reynolds-Averaged Navier-Stokes (RANS) solvers to predict high lift flow fields. They accomplished this by analyzing research results that were published in the last ten to fifteen years which pertain to the application of RANS solvers to high lift applications. They found that the surface pressure, skin friction, lift and drag can generally be predicted with reasonable good accuracy for both two-dimensional and three-dimensional flows for angles of attack below stall. However, three-dimensional computations regarding the maximum lift coefficient seemed inconsistent and was often overpredicted. The origin of these inconsistencies was predominantly caused by the lack of modeling fidelity regarding the unsteady effects and the implementation of turbulence models.

A decade later, Rumsey et al [7] [8] summarized two workshops which were held to access the prediction capabilities of current generation CFD technology regarding swept, various aspect-ratio wings in high-lift flow fields. The research was focused on the three-element swept wing which was allegedly tested by the National Aeronautics and Space Administration (NASA) to obtain validation data. The workshop demonstrated the difficulty in modeling stalling flow. Due to this, the results of the workshop's participants showed additional spread among their solutions near stall. However, the stall angle and maximum lift coefficient could be predicted within a 5% – 9% error margin with the implementation of the SA turbulence model [8].

Hence, the current state of the art is able to predict the stall angle and associated maximum lift coefficient. However, intricate CFD schemes and complex turbulence models with specified grid refinements are necessary to converge to an accurate solution. It is generally known that this convergence takes excessive amount of computational time. Hence, the state-of-the art lies beyond the scope of this thesis work. In the following, methods with compensated fidelity are presented which allow for the prediction of the  $C_{L_{\max}}$  while being computationally cheaper.

### 2.4.2. ALPHA METHOD

The so-called  $\alpha$  methods are methods that apply corrections to the angle of attack of an inviscid three-dimensional aerodynamic analysis. One of these methods has been developed by van Dam [4] in order to compute a wing's maximum lift coefficient. Here, he utilizes two-dimensional viscous section data from either experiments or CFD tools to determine the effective angle of attack along a number of spanwise sections. Initially, the zero lift angle of attack  $\alpha_0$  and lift-curve slope  $C_{l_\alpha}$  at each section is computed with a vortex lattice method. Subsequently, the following iterative procedure is started:

1. The effective local angle of attack for each spanwise section at a specified geometrical angle of attack is computed using:

$$\alpha_{\text{eff}} = \frac{C_{l_{\text{inv}}}}{C_{l_\alpha}} + \alpha_0 - \Delta\alpha_{\text{corr}} \quad (2.5)$$

2. At this effective local angle of attack, the viscous lift coefficient is computed by a two-dimensional viscous analysis tool:

$$C_{l_{\text{visc}}} = \text{2DViscousAnalysis}(\alpha_{\text{eff}}, M_{\text{eff}}, Re_{\text{eff}}) \quad (2.6)$$

3. if  $|C_{l_{\text{visc}}} - C_{l_{\text{inv}}}| > \epsilon$ , where  $\epsilon$  is an user-selected convergence criteria which is typically around 0.01, the appropriate viscous correction angle is determined by:

$$\alpha_{\text{corr}} = \frac{C_{l_{\text{visc}}} - C_{l_{\text{inv}}}}{C_{l_{\alpha}}} \quad (2.7)$$

4. Using  $\alpha_{\text{corr}}$ , the Right Hand Side (RHS) of a vortex lattice analysis is adjusted and a new lift distribution and lift coefficient are computed.
5. if  $|C_{l_{\text{visc}}} - C_{l_{\text{inv}}}| \leq \epsilon$ , the procedure is halted and the next spanwise section is scrutinized.
6. If  $\alpha_{\text{corr}}$  is known for every spanwise station, the geometrical wing angle of attack is increased.

The  $\alpha$  method is represented graphically in Figure 2.33. The discussed procedure needs to be repeated for a complete range of angle of attacks to establish the wing's stall angle and maximum lift coefficient from the resulting lift polar. For two-dimensional viscous analysis, one can utilize the open source two-dimensional MSES code developed by Mark Drela of the Massachusetts Institute of Technology (MIT). The  $\alpha$  method is also capable of analyzing high-lift wings given that both the vortex lattice method and two-dimensional viscous analysis can cope with high-lift configurations.

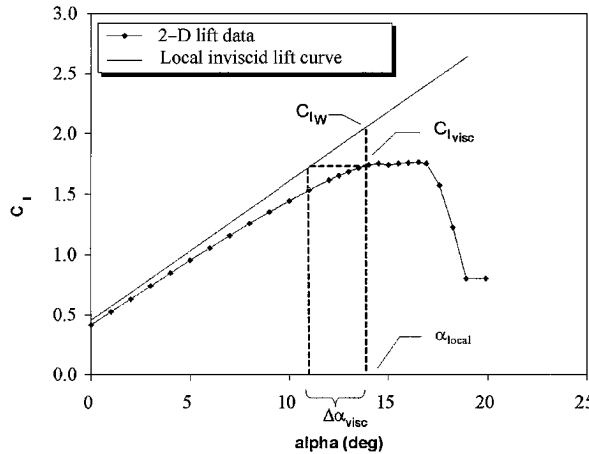


Figure 2.33: A visual of the  $\alpha$  method routine to approximate the non-linear part of a lift polar [4]

#### 2.4.3. ESDU 89034 METHOD

The IHS ESDU [20] developed a table-lookup method to empirically derive the clean maximum wing lift coefficient in their ESDU 89034 item. The method is applicable to straight-tapered wings with or without camber and a linear twist distribution provided that the local effective twist is not excessive. The method is able to cope with any section shape or camber line, both of which may vary across the span. The total design space of this method is given in Table 2.5. The method is restricted to wings with smooth surfaces or with a narrow band of roughness with height just sufficient to ensure boundary-layer transition [20]. The expression that they created is displayed in Equation 2.8.

$$C_{L_{\max}} = C_{L_m} / \mu_p + \Delta C_{L_M} + C_{L_R} + C_{L_A} + C_{L_T} \quad (2.8)$$

Here,  $C_{L_m} / \mu_p$  models the most highly loaded wing section. The subsequent correction factors  $C_{L_M}$ ,  $C_{L_R}$ ,  $C_{L_A}$  and  $C_{L_T}$  correct for Mach number, Reynolds number, sweep and twist effects respectively. The design space depicted in Table 2.5 indicates that this method is suitable for predicting maximum lift coefficient up to transonic conditions. However, with Mach numbers up to 0.8, the method assumes that the wing under scrutiny has a sufficient amount of wing sweep to avoid the formation of shock waves since shock wave boundary layer interaction is not discussed within this ESDU item. To obtain a glance of the implemented graphs depicting the empirical data, the reader is referred to [20].

Table 2.5: Design space of the ESDU 89034 prediction methodology

Geometry parameter	Range
Taper ratio	0.2 to 1.0
Aspect ratio	2 to 12
Leading-edge sweep	0 to 50°
Trailing-edge sweep	0 to 45°
Reynolds number	0.7 to $12 \cdot 10^6$
Mach number	0 to 0.8

#### 2.4.4. CRITICAL SECTION METHOD

Back in 1959, Abbott and von Doenhoff [32] suggested a semi-empirical method for predicting both high-lift and clean maximum wing lift coefficient. Herein, the point of stall is given by the spanwise location where the local section lift coefficient is equal to the maximum lift coefficient of the airfoil used at that same location. This basic rule for predicting wing stall lacks theoretical justification [11] but has shown to be effective in predicting the maximum wing lift coefficient when used correctly [33, 34]. Implementation of the so-called Critical Section Method approach can be summarized as follows:

1. For a specified Reynolds number and Mach number, plot the distribution of  $c_{l_{\max}}$  as function of spanwise position  $\eta = y/(b/2)$ .
2. Plot the theoretically calculated span loading distribution as a function of angle of attack  $\alpha$ . To obtain the span loading, higher order surface panel method or computational fluid dynamics can be implemented but simple vortex-lattice methods suffice.
3. The stall angle of attack is found when the difference between the curves of Step. 1 and Step. 2 are within an user-specified error margin, typically within an error margin of 1%.
4.  $C_{L_{\max}}$  is found by reading the wing's approximated lift polar at the computed stall angle.

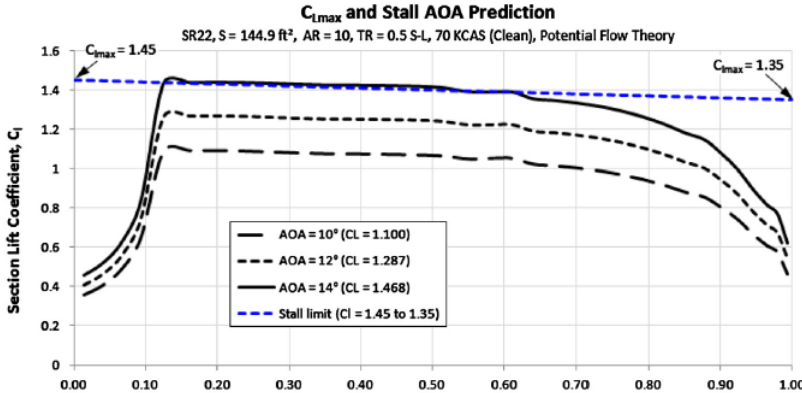


Figure 2.34: Lift distribution near stall as predicted by a vortex-lattice method and the distribution of section maximum lift coefficient[10]

This method has been scrutinized by Gudmundsson [10], here he calculated the maximum wing lift coefficient for the Cirrus SR22 and compared it to flight test data. His test indicated that the approximation differed by 4.1% when compared to the measurements, Which is fairly accurate. Therefore, this method is suitable for an conceptual approximation of maximum lift coefficient. Also, this method can be implemented by coupling the semi-empirical ESDU 84026 method for the prediction of the airfoil  $c_{l_{\max}}$  with a vortex lattice solver. Furthermore, the critical section method is applicable to high-lift wings if the effects of the high-lift devices on the local section  $c_{l_{\max}}$  are available.

### 2.4.5. UNITED STATES AIR FORCE DATCOM METHOD

A empirical table-lookup method is constructed by Datcom to determine the subsonic clean maximum lift coefficient. The method is derived empirically for high aspect ratio, untwisted and constant section wings [10–12]. To determine whether a wing complies with Datcom's definition of a high-aspect-ratio wing, the following relation must hold:

$$AR > \frac{4}{(C_1 + 1)\cos\Lambda_{LE}} \quad (2.9)$$

Here  $\Lambda_{LE}$  is the leading-edge sweep angle and  $C_1$  is an empirically determined parameter which is related to the wing's taper ratio  $\lambda$ , as can be seen in Equation 2.10.

$$C_1 = \frac{1}{2} \sin \left( \pi (1 - \lambda)^{1.5 + 0.8 \sin^{0.4}(\pi(1 - \lambda)^2)} \right) \quad (2.10)$$

The wing under scrutiny is labeled as a high aspect ratio wing if Equation 2.9 is satisfied. Subsequently, the maximum lift coefficient is determined with the following expression:

$$C_{L_{max}} = \left( \frac{C_{L_{max}}}{c_{l_{max}}} \right) c_{l_{max}} + \Delta C_{L_{max}} \quad (2.11)$$

Here,  $c_{l_{max}}$  is the section maximum lift coefficient, which is assumed to be constant for a given wing.  $\frac{C_{L_{max}}}{c_{l_{max}}}$  is an empirical ratio between the maximum wing and section lift coefficient. This empirically derived ratio is a function of the leading-edge sharpness parameter  $\Delta y$  and the leading-edge sweep angle, see Figure 2.35.  $\Delta C_{L_{max}}$  is a correction factor for Mach numbers exceeding 0.2. This correction variable is a function of leading-edge sweep angle and the leading-edge sharpness parameter  $\Delta y$ , as can be seen in Figure 2.36.

Again, Gudmundsson [10] tested this method with the Cirrus SR22 wing. The findings showed that the implementation of this method yielded an error 11.6%. This still adheres to the limit of acceptability in a conceptual design framework. However, the main bottleneck of this method is the inability to analyze wings having either a low aspect ratio, twist or variable airfoil sections throughout the wing span.

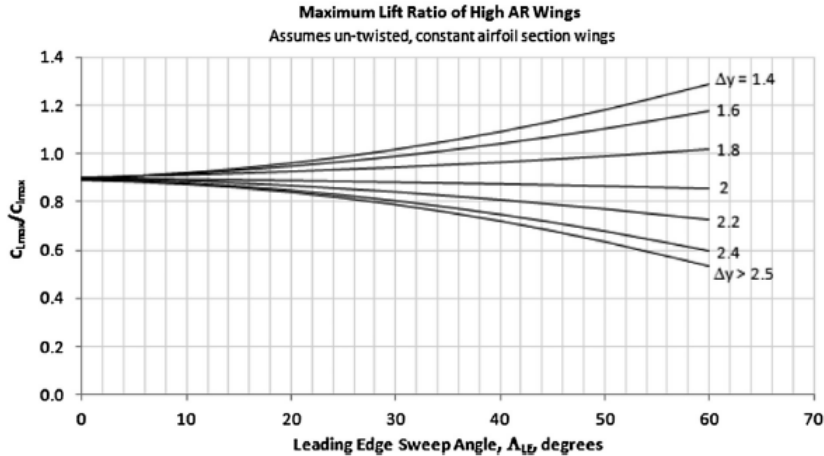


Figure 2.35: Empirical  $\frac{C_{L_{max}}}{c_{l_{max}}}$  ratio determined by USAF Datcom [10, 12]

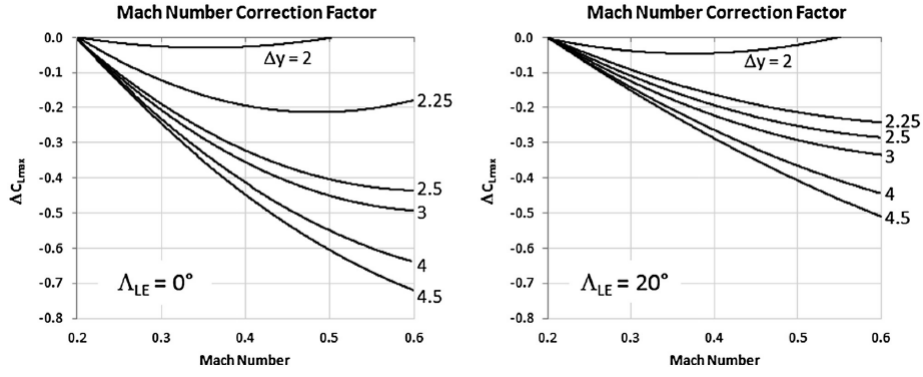


Figure 2.36: Empirical  $\Delta C_{L\max}$  as determined by USAF DATCOM for  $\Lambda_{LE} = 0$  and  $\Lambda_{LE} = 20$  [10, 12]

#### 2.4.6. PHILLIPS AND ALLEY'S METHOD

Phillips and Alley [35] present a method for estimating the clean maximum wing lift that is based on the classical lifting line theory. Their approach involves providing correction factors for the effects of twist and sweepback on the span loading of unswept, untwisted, tapered wings. The correction factors are developed with the aid of CFD panel method computations for a variety of conventional wing planforms. Curves for the correction factors are presented for a number of specific taper and aspect ratios along with the general method for calculating these effects for other wing geometry [10]. The main expression to determine the maximum lift coefficient is given by the following:

$$C_{L\max} = \left( \frac{C_L}{\tilde{c}_{l\max}} \right)_{\Omega=0}^{\Lambda=0} \cdot k_{L_s} k_{L_\Lambda} (\tilde{c}_{l\max} - k_{L_\Omega} C_{L\alpha} \Omega) \quad (2.12)$$

Here,  $k_{L_s}$  accounts for unsymmetrical wing stall. Alley, Phillips and Spall [36] implemented CFD to develop an algebraic correlation for the stall factor as a function of geometric wing parameters. In their model, they utilized the NACA 0012 airfoil as the base wing section for the 2-D and 3-D computations at a constant Reynolds number of  $3 \cdot 10^6$ . All computations were performed with the Fluid dynamics code CFL3D, they found that the stall factor  $k_{L_s}$  could be approximated by the following:

$$k_{L_s} = 1 + (0.0042 \text{AR} - 0.068)(1 + 2.3C_{L\alpha})\Omega / \tilde{c}_{l\max} \quad (2.13)$$

The sweep correction factor has also been described by the work of Phillips and Alley (2007) [35]. Herein, they introduce a numerical approximation to the sweep correction factor  $k_{L_\Lambda}$ . This numerical approximation depends on the quarter chord sweep angle, taper ratio and aspect ratio, see the following:

$$k_{L_\Lambda} = 1 + \kappa_{\Lambda 1} \Lambda_{c/4} - \kappa_{\Lambda 2} \Lambda_{c/4}^{1.2} \quad (2.14)$$

Here, empirical data on  $\kappa_{\Lambda 1}$  and  $\kappa_{\Lambda 2}$  can be found in Figure 2.37. The twist correction factor  $k_{L_\Omega}$  was readily determined by Phillips and Alley. They found that the twist correction factor can be expressed by the following:

$$k_{L_\Omega} = \left[ 1 - \frac{C_L}{\tilde{c}_{l\max}} / \left( \frac{C_L}{\tilde{c}_{l\max}} \right)_{\Omega=0} \right] / \frac{C_{L\alpha} \Omega}{\tilde{c}_{l\max}} \quad (2.15)$$

Phillips and Alley compared the proposed lifting line method against results that are obtained from grid resolved CFD solutions. They tested 25 different wing configurations that had aspect ratios ranging from 4 to 20, taper ratios from 0.5 to 1.0, quarter-chord sweep angles from 0 to 30 deg and a linear geometric washout ranging from 0 to 8 deg. They found that the results obtained from Equation 2.12 agreed well with CFD solutions, the error was typically within error margin of 1%. This is rather suspect for a method based on a lifting line method. For more information regarding this method, the reader is referred to [35] and [36].

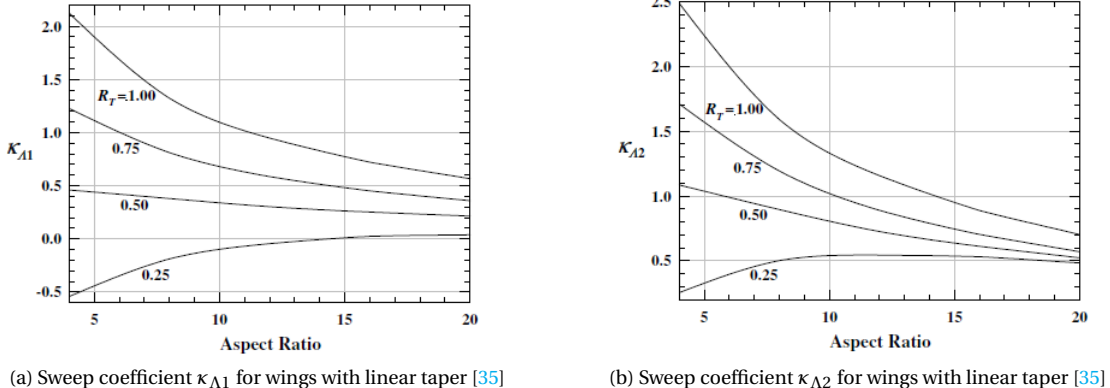


Figure 2.37: Behavior of sweep coefficients

#### 2.4.7. PRESSURE DIFFERENCE RULE

The Pressure Difference Rule (PDR) is a cost effective semi-empirical method for the prediction of a wing's maximum lift. It is a combination of an empirically derived phenomenon which occurs at maximum wing lift and practical CFD technology. The method revolves around the spanwise distribution of pressure differences between the suction peak and trailing edge of chordwise wing sections. Maximum wing lift coefficient is reached when this pressure difference reaches a critical value, which is dependent on both the Reynolds number and Mach number. This dependence is also illustrated in Figure 2.38. The method is suitable for the prediction of maximum lift on both clean and complex multi-element wing configurations and is therefore interesting for the current research. The discussed method is developed and validated by Valerzo and Chin [37] and showed remarkably good results. The pressure difference rule can be outlined by the following:

1. The wing geometry under consideration is divided in several wing stations. At these stations, the effective Reynolds number based on clean wing chord and effective Mach number are computed, See Equation 2.16 to Equation 2.18.

$$V_{\text{eff}} = \frac{V_{\perp}}{\cos(\alpha_i)} \quad (2.16)$$

$$M_{\text{eff}} = \frac{V_{\text{eff}}}{a} \quad (2.17)$$

$$Re_{\text{eff}} = Re_{\infty} \frac{V_{\text{eff}}}{V_{\infty}} \frac{c_{\perp}}{c} \quad (2.18)$$

2. The effective Mach number and Reynolds number are used in conjunction with Figure 2.38 to construct the critical pressure difference distribution over the wing.
3. The spanwise distribution of chordwise pressure differences is obtained at increasing angles of attack for the wing geometry under consideration. Valerzo and Chin suggest the usage of a higher order surface panel method for this step.
4. This process is repeated for a range of angles of attack until the curves of Step. 2 and Step. 3 are within an user-specified error margin, typically within an error margin of 1%. The  $C_L$  at which this occurs is the  $C_{L\max}$ .

An example of this method is depicted in Figures 2.39 and 2.40 for a swept high-lift wing configuration with a trailing-edge flap. From these Figures it can be deduced that the PDR approximation agrees remarkably well with experimental results. To reduce computational expense, van Dam [4] suggests the coupling of a two-dimensional vortex panel method and a downwash model to approximate the chordwise pressure difference at several wing stations.

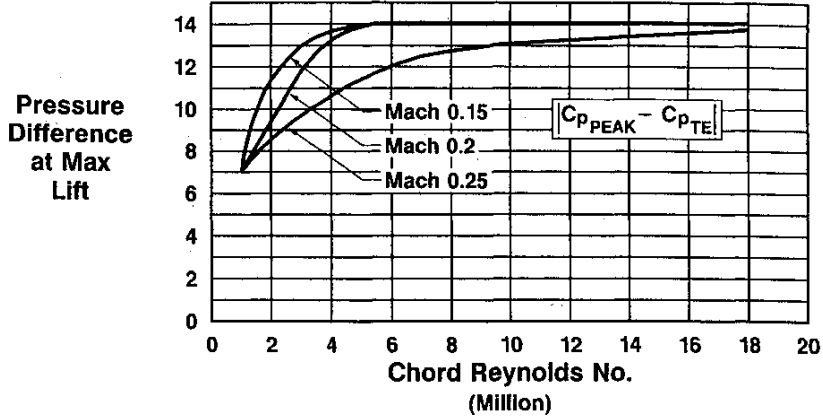


Figure 2.38: Critical pressure difference for given Mach number and chordwise Reynolds number [37]

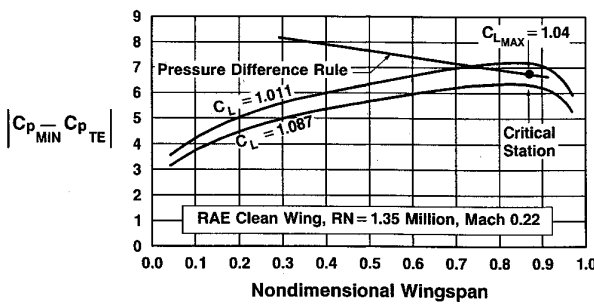


Figure 2.39: Example pressure difference distribution on a swept high-lift wing [37]

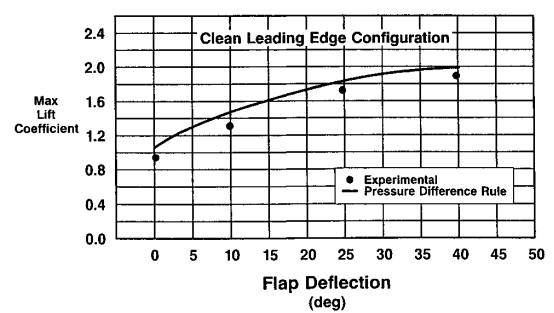


Figure 2.40: Pressure Difference Rule validation against wind tunnel measurements [37]

#### 2.4.8. EMPIRICAL HIGH-LIFT INCREMENT FACTORS

The presented empirical methods are only capable of determining the clean maximum lift coefficient of a wing. This applies to the Datcom and ESDU method as well as the method devised by Phillips and Alley. To complement these methods for high-lift  $C_{L_{\max}}$  predictability, one can utilize empirical  $\Delta C_{L_{\max}}$  increment factors to account for the increase in maximum lift coefficient by deploying high lift devices.

Both the Datcom and IHS ESDU devised empirical databases to establish this  $\Delta C_{L_{\max}}$  increment. Datcom proposed the following increment factor to account for a flap deflection [12]:

$$\Delta C_{L_{\max,f}} = c_{l_{\max}} \frac{S_{wf}}{S} K_{\Lambda} \quad (2.19)$$

where  $c_{l_{\max}}$  is the incremental effect of the high-lift device on the respective wing section, see Figure 2.41. The ratio  $\frac{S_{wf}}{S}$  is the wing area effected by the high-lift device over the total wing area. The effected wing area is depicted by the shaded area in Figure 2.42.

Subsequently, the high-lift increment of Equation 2.19 is added to the clean maximum lift coefficient that is determined by the presented empirical methods:

$$C_{L_{\max,high-lift}} = \Delta C_{L_{\max,clean}} + \Delta C_{L_{\max}} \quad (2.20)$$

Datcom also established a similar correction increment for deploying leading-edge devices, this method is elaborately discussed in their design handbook [12] and by Sforza [11]. Similarly the IHS ESDU wrote several articles on behalf of this topic. For interested readers, one is referred to the ESDU 91030 paper [38] and affiliated research items.

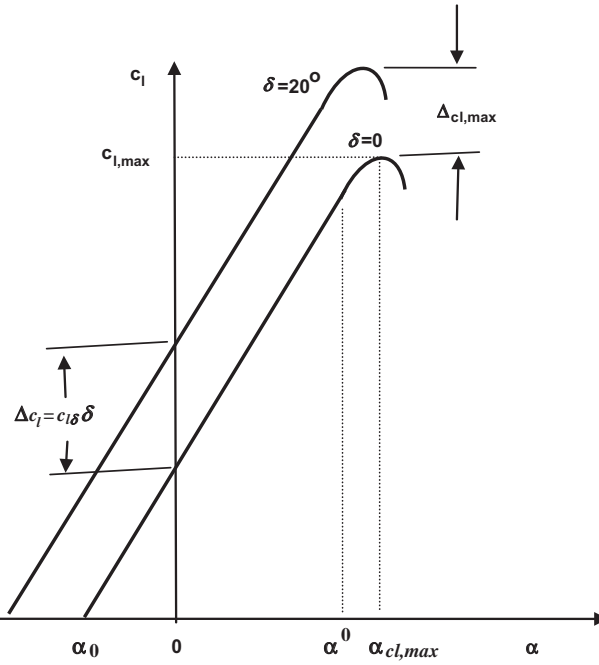


Figure 2.41: Upward increment in airfoil lift polar due to the deployment of a flap by  $20^\circ$  [11]

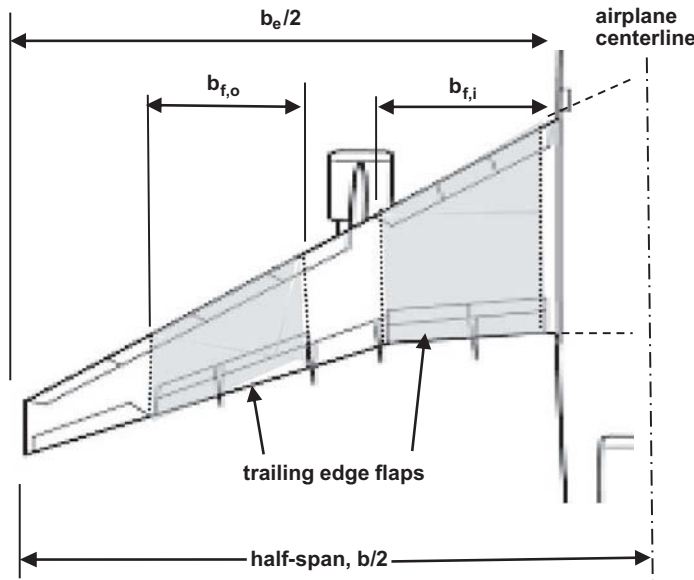


Figure 2.42: Planform of a wing where the shaded area is the portion of the wing planform area affected by deployed flaps [11]

#### 2.4.9. METHOD TRADE-OFF

At this point, several methods to predict the maximum lift coefficient have been introduced. A trade-off has been conducted to select appropriate methods to support the development of a maximum lift coefficient prediction method. Within the trade-off, the presented methods are criticized against key criteria points that are set-up in the research goal. Table 2.6 summarizes the presented and therefore considered methods for the development of a  $C_{L\max}$  prediction tool. Here, the various approaches are labeled accordingly to improve the readability. Table 2.7 devises a scoring outline for this trade-off. Hereby, it is chosen to grade every criteria point with a number between -2 and 2. The implementation of this system will award points to methods which excels in meeting key criteria points and penalize them if they fails to do so.

The key criteria points are presented in Table 2.8 along side the total scoring results. The run time is a measure which criticizes the computational expense of the method. Hereby, a score of -2 is rewarded if the method is unable to yield results within 15 seconds, e.g. RANS-solver. The  $\alpha$  method is rewarded a score of -1, this is because it is not totally depreciated since an approach to cut computational expense might be required to make this method viable. The other methods are all rewarded 2 points since they are either table-look up methods, which are fairly rapid. Or methods that use an empirical database alongside computationally cheap panel methods.

For the complexity criteria, the presented methods are criticized against the complexity of the method's implementation. The RANS-solver is rewarded a score of -2 since difficult mesh generations and turbulence models are required to achieve a  $C_{L_{max}}$  prediction. The  $\alpha$  method obtains a score of -1 because the method itself might be straightforward but generalizing a two-dimensional viscous convergence analysis, which is also rapid, raises this method's complexity. The table-lookup methods are all awarded 2 points since they are straightforward to use, since they revolve around reading tables and graphs. Both the pressure difference rule and critical section method are awarded 1 point since their implementations are significantly easier than the  $\alpha$  method but are more complex than the simple table-lookup methods.

The methods are also assessed against the compatibility within the Initiator. As was mentioned previously, the Initiator is written in MatLab. Hence, a seamless implementation between the method and MatLab should exist. The RANS-solver is penalized by 2 points since it is impossible (within the best knowledge of the author) to batch run or incorporate a full RANS-solver within the MatLab environment. All other methods are rewarded 2 points since the either the method itself or tools required by the method are implementable within MatLab or have a batch run available.

Next, the accuracy of the methods is scrutinized. Here, the RANS-solver scores the highest grade since it applies the most complex analysis and the state-of-the-art showed accurate  $C_{L_{max}}$  predictions. The  $\alpha$  method is given 1 point since it is able to incorporate viscous effects to a certain degree. The table-lookup methods are all penalized since they only yield accurate results when the conditions considered are in par with the design space upon which these methods are build. The pressure difference rule and critical sections method both have a neutral score since they also suffer from the fact that they are based on an empirically derived design space or phenomena. However, both methods model the wing as a whole, hence, minimal changes to the wing geometry can be captured by these methods.

Finally, the methods are judged against their versatility to analyze a broad selection of wing and aircraft geometries. Hereby, the methods that build the wing or aircraft as a whole to predict  $C_{L_{max}}$  excel. Therefore, they are awarded 2 points. The ESDU 89034 method is penalized by 1 point since it is only applicable to wings having a linear twist distribution; this is often not the case for actual wing designs. Both the Datcom and Phillips and Alley's method have an unacceptable versatility. This is because Datcom's method is only for wings which are build from one airfoil and wings without twist. Phillips and Alley's method incorporates a stall correction factor that is based on a constant Reynolds number analysis. Therefore, this method lacks generality. The pressure difference rule is awarded 1 point since it is based on a limited design space, which ranges between a Mach number of 0.15 to 0.25 and a Reynolds number between 0 to  $20 \cdot 10^6$ .

To conclude, the critical section method and pressure difference rule yield relative striking trade-off results with an aggregate of 7 and 6 points respectively. Because their respective final results lie in close proximity, both methods are considered as the basis of the  $C_{L_{max}}$  prediction tool.

Table 2.6: High-lift maximum lift coefficient prediction method implementation outline

Method label	Prediction method	Method Implementation
$\alpha$	$\alpha$ method	Three-dimensional vortex lattice solver with a two-dimensional Euler code having a boundary layer model.
$\beta$	RANS-solver	Three-dimensional Reynolds-Averaged Navier-Stokes solver with turbulence model.
$\gamma$	ESDU 89034 method	Empirical table-lookup model with high lift increment factor.
$\delta$	Critical section method	Three-dimensional vortex lattice solver with empirical $c_{l_{max}}$ model.
$\epsilon$	USAF Datcom method	Empirical table-lookup model with high lift increment factor.
$\zeta$	Phillips and Alley's method	Empirical model with a CFD based stall correction factor and high lift increment factor.
$\eta$	Pressure difference rule	Two-dimensional vortex panel method with three-dimensional downwash model.

Table 2.7: High-lift maximum lift coefficient prediction method scoring outline

Score label	Value
Superior	2
Acceptable	1
Neutral	0
Poor	-1
Unacceptable	-2

Table 2.8: High-lift maximum lift coefficient prediction method trade-off results

Prediction method	Run time	Complexity	Initiator compatible	Accuracy	Versatility	Total score
$\alpha$	-1	-1	2	1	2	3
$\beta$	-2	-2	-2	2	2	-2
$\gamma$	2	2	2	-1	-1	4
$\delta$	2	1	2	0	2	7
$\epsilon$	2	2	2	-1	-2	3
$\zeta$	2	2	2	-1	-2	3
$\eta$	2	1	2	0	1	6

## 2.5. ROOT FINDING ALGORITHMS

As the title and purpose of this thesis suggests, we are interested in a method that determines the  $C_{L_{max}}$  of an aircraft with an emphasis on rapidity. Considering that a significant amount of factors and design variables affect the prediction of  $C_{L_{max}}$ , it is efficient to consider optimization algorithms to achieve an efficient prediction method. The need for these optimization algorithms is established due to the nature of the considered  $C_{L_{max}}$  prediction routines. Both the critical section method and pressure difference rule embed a scheme that both require an iterative process which lasts until a critical condition depicting wing stall is reached. These iterative processes can be optimized by implementing root-finding routines with the aggregates of either the distribution of spanwise maximum section lift coefficient or spanwise pressure difference.

Essentially, root-finding algorithms are numerical algorithms for finding a value  $x$  such that  $f(x) = 0$ , for a generic function  $f(x)$ . Similarly, finding the root of  $f(x) - g(x) = 0$  is equal to solving the equation  $f(x) = g(x)$ . Here,  $x$  is labeled as the unknown of the equation, e.g. the stall angle of attack. Numerical root-finding methods are based on iterative procedures, producing a sequence of iterations that hopefully converge towards the root as a limit. They require one or more initial guesses of the root as initial values to determine the interval that encloses a root. Then each consecutive iteration of the algorithm produces a successively more accurate approximation of the root. As of today, many root-finding algorithms exist, each with their own perks and characteristics. Desirable characteristics include a rapid rate of convergence and robustness at roots in close proximity. In the following, two root-finding methods are discussed, namely the bi-section method and Newton-Raphson method. Each method is assessed against the previously described desirable characteris-

tics.

### 2.5.1. BI-SECTION ALGORITHM

The bisection method in mathematics is a root-finding method that repeatedly bisects an interval and then selects a subinterval in which a root must lie for further processing. It is a relatively simple and robust method, but it is also relatively slow since it has a linear convergence rate of 1/2. The method is applicable for numerically solving the equation  $f(x) = 0$  for a real variable  $x$ , where  $f$  is a generic continuous function defined on an interval  $[a, b]$  and where  $f(a)$  and  $f(b)$  have opposite signs, as can be seen in Figure 2.43.

At each step the method bisects the interval in two by computing the midpoint  $c = (a + b)/2$  of the interval and the value of the function  $f(c)$  at that specific point. There are now only two possibilities: either  $f(a)$  and  $f(c)$  have opposite signs and bracket a root, or  $f(c)$  and  $f(b)$  have opposite signs and bracket a root. The method selects the subinterval in which the root resides and subsequently uses this new interval in the next step. This process is iterated until the difference between the approximated roots of two consecutive iterations is smaller than a predefined error margin (typically 1% relative difference) [39].

The method is laid out in the following scheme where a generic function is used to define function values, which in this case, represents the spanwise lift- and pressure difference distributions.

1. An initial angle of attack range is selected that contains the stall angle. Here, the function values at the outer edges of the interval are computed,  $f(\alpha_i)$  and  $f(\alpha_{i+1})$ .
2. Now, the initial interval is bisected:  $\alpha_{i+2} = \frac{\alpha_i + \alpha_{i+1}}{2}$ . At this point, the function value  $f(\alpha_{i+2})$  is computed.
3. A sign check is performed with the calculated function values to find the subinterval that includes the extremum. This interval becomes the new interval under scrutiny.
4. Step. 2 and Step. 3 are iterated until the interval is sufficiently small and the stopping criterion is met.

A problem that might occur with the implementation of this method is that it has a poor robustness when multiple roots are enclosed in the initial interval. Here, the method will converge only to a single root. However, this is not the case for the current purpose since there is only a single stall angle.

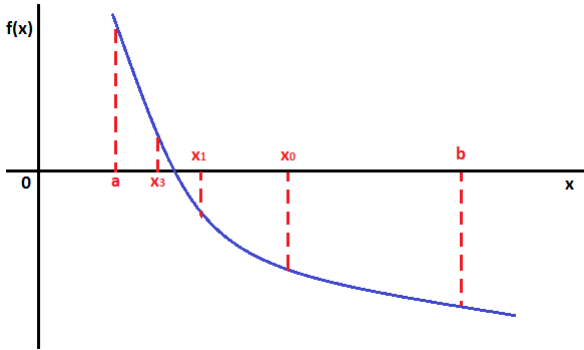


Figure 2.43: Graphical representation of the bisection method

### 2.5.2. NEWTON-RAPHSON ROOT FINDING ALGORITHM

Another method to find the root of a real-valued function is the Newton-Raphson algorithm. Herein, The method starts with a function  $f(x)$  defined over the real numbers  $x$ , the function's derivative  $df(x)/dx$ , and an initial guess  $x_0$  for a root of the function  $f(x)$ . Subsequently, the function is approximated by its tangent line at  $x_0$ , and one computes the x-intercept of this tangent line. This x-intercept will typically be a better approximation to the function's root than the original starting point. This scheme is mathematically expressed in Equation 2.21 and depicted in Figure 2.44.

$$x_{n+1} = x_n - \frac{f(x_n)}{f'(x_n)} \quad (2.21)$$

This is a powerful method with a convergence that is generally quadratic. For a full derivation of the convergence of this method, the reader is referred to the book of Whittaker and Robinson [40]. The applicability of this method is only valid for differentiable functions that are definable and well behaved on the initial interval. Care should be taken when stationary points are considered, the derivative of the considered function will be zero that leads to the failure of the method. However, this is unlikely to happen with the aggregate of the spanwise lift- and pressure difference distribution.

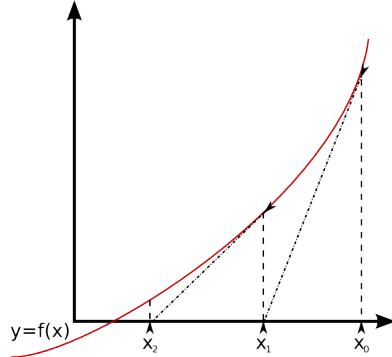


Figure 2.44: Graphical representation of the Newton-Raphson algorithm



# 3

## METHODOLOGY

Within this Chapter, the applied methodology to build a low-speed maximum lift coefficient prediction method is described. In Sections 3.1 and 3.2, the implementations of the so-called Critical Section Method and Pressure Difference Rule are presented. Then in Section 3.3, the implementation of the Pressure Difference Rule for high-lift configurations is described. This is followed by a description on the modification of the Initiator in terms of airfoil shape generation in Section 3.4. Hereafter, empirical corrections for the effects of the fuselage is described in Section 3.5. Finally, the working principles behind the rapidity of the  $C_{L_{\max}}$  prediction method are discussed in Section 3.6 while the verification of the developed method is described in Section 3.7.

**Key words**—Critical Section Method, Pressure Difference Rule, AVL, Parsing, Smoothing, Newton-Raphson, Convergence, Verification, Downwash, Panel method, Vortex

### 3.1. CRITICAL SECTION METHOD IMPLEMENTATION

In Section 2.4.9, a trade-off between several methods to predict maximum wing lift coefficient in both clean and high-lift configuration has been conducted. Herein, it was evident that both the Critical Section Method and the Pressure Difference Rule were suitable for predicting low-speed maximum wing lift coefficient within the scope of this thesis. In this Section, the implementation of the Critical Section Method for clean  $C_{L_{\max}}$  prediction is described in an effort to explore the suitability of this method for the development of a  $C_{L_{\max}}$  prediction method.

Recalling from Section 2.4.4, the working principles of the Critical Section Method are repeated here:

1. For a specified Reynolds number and Mach number, plot the distribution of  $c_{l_{\max}}$  as function of spanwise position  $\eta = y/(b/2)$ .
2. Plot the theoretically calculated span loading distribution as a function of angle of attack  $\alpha$ . To obtain the span loading, higher order surface panel method or computational fluid dynamics can be implemented but simple vortice lattice methods suffice.
3. The stall angle of attack is found when the difference between the curves of Step. 1 and Step. 2 are within a user-specified error margin, typically within an error margin of 1%.
4.  $C_{L_{\max}}$  is found by reading the wing's approximated lift polar at the computed stall angle.

Mark Drela's vortex-lattice code Athena Vortex Lattice (AVL) [41] is proposed to perform the inviscid three-dimensional wing analysis, see Section 3.1.2 for an elaborate description of AVL. The reason for this is that this software is already inherently incorporated within the Initiator. In regards to this, AVL has proven to be quick, effective, and easily coupled to MatLab due to the availability of a batch run. To estimate the maximum section lift coefficient, use have been made of the semi-empirical ESDU 84026 [42] method. This is a table-lookup method which implements a combination of airfoil geometry and experimental trends for the prediction of  $c_{l_{\max}}$ . This method is addressed in the following section.

### 3.1.1. MAXIMUM AIRFOIL LIFT COEFFICIENT

The IHS ESDU provides validated design methods, data and software tools covering a wide range of engineering disciplines. These design methods are monitored and validated to ensure correctness. In IHS ESDU 84026 [42], Hollis and Williams present a semi-empirical method for the prediction of the maximum airfoil lift. Herein, they found that the airfoil's nose thickness,  $z_{u1.25}/c$ , and the trailing-edge boat angle,  $\tau_u$ , both play a pivotal role in determining an airfoil's  $c_{l_{\max}}$ . The geometrical airfoil nomenclature used by ESDU 84026 is illustrated in Figure 3.1.

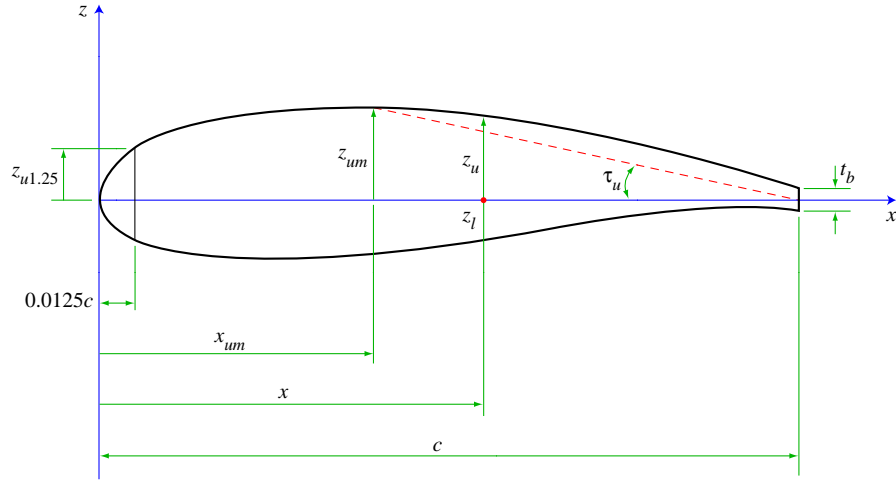


Figure 3.1: Airfoil geometry nomenclature as per IHS ESDU [42]

They found that the correlation for the maximum lift coefficient of an airfoil can be split in two separate groups. Those with  $z_{u1.25}/c < 0.017$  and those with  $z_{u1.25}/c \geq 0.017$ . Herein,  $z_{u1.25}$  is the upper surface coordinate at  $x/c = 0.0125$  as can be seen Figure 3.1. Hereby, the trailing-edge and leading-edge separation types are effectively distinguished. With this, IHS ESDU established a single correlation, presented in Equation 3.1, for both stall types while using the geometrical parameters which are depicted in Figure 3.1.

$$c_{l_{\max}} = (C_{l_0} + \Delta C_l) F_M F_S \quad (3.1)$$

Hereby,  $C_{l_0}$  is the lift coefficient at zero incidence,  $\Delta C_l$  is an incremental lift coefficient increase. The factor  $F_S$  is a correction for airfoils having a rearward loading and  $F_M$  is a correction for compressibility effects. On behalf of this, their proposed model is applicable to cambered, symmetrical and more modern airfoil which have a pronounced rearward loading. In the following, a brief explanation of the relevant factors is presented.

#### LIFT COEFFICIENT INCREMENT $\Delta C_l$

The empirical parameter  $\Delta C_l$  essentially provides an incremental increase from the lift at zero incidence towards  $c_{l_{\max}}$ . Hollis and Williams [42] found that this parameter differs for the stalling types considered during their analysis of experimental data. In Figure 3.2a the lift increment in case of leading-edge separation is given. Here, William and Hollis found that this parameter was effectively dictated by both the Reynolds number and the leading edge thickness. On the other hand, the lift increment of airfoils suffering from trailing-edge stall was dictated by both the trailing-edge boat angle, see Equation 3.2 and the Reynolds number, as can be seen in Figure 3.2b. These conclusions are in agreement with the findings of Section 2.3.2.

$$\tan(\tau_u) = (z_{um}/c)/(1 - x_{um}/c) \quad (3.2)$$

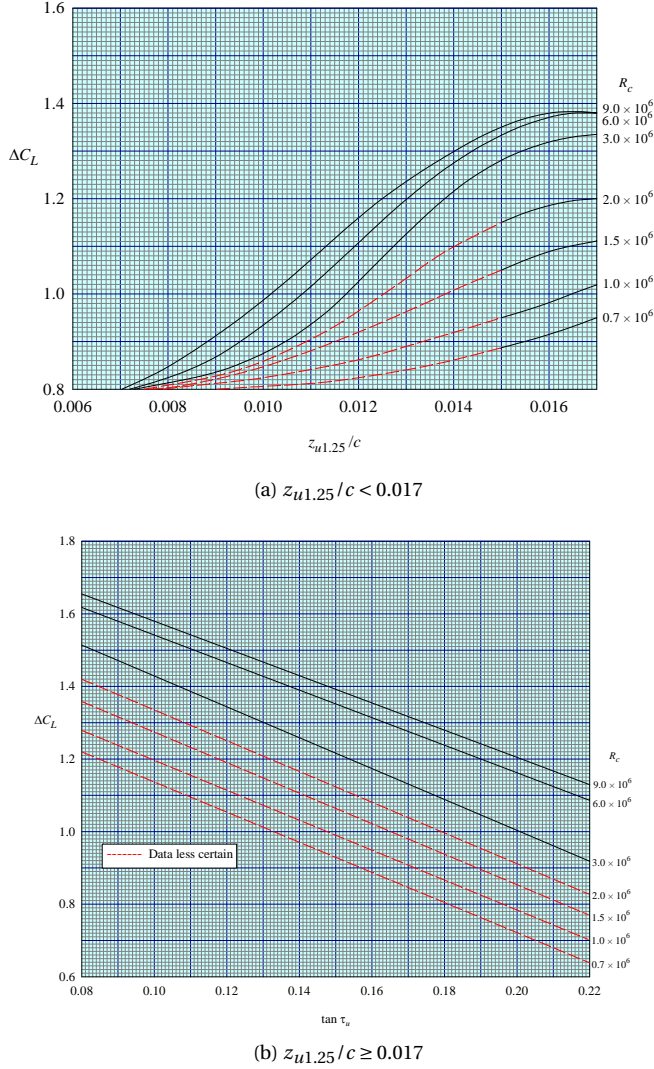


Figure 3.2: Lift coefficient increment for airfoils with smooth leading edges [42]

#### LIFT COEFFICIENT AT ZERO INCIDENCE $C_{l0}$

The coefficient  $C_{l0}$  is obtained by combining the lift-curve slope  $(a_1)_0$  for incompressible flow with the angle at zero-lift  $\alpha_0$ . The zero lift angle is obtained by using the method which is presented in the paper of Pankhurst's (cited in ESDU 84026, 1984, p.10):

$$\alpha_0 = \frac{\pi}{90} \sum_{i=1}^{14} (B_i z_{ci}/c) \quad (3.3)$$

where  $B_i$  are weights which are given in the data file and where  $z_{ci}$  is defined by the following:

$$z_{ci} = [z_u(x_i/c) + z_l(x_i/c)]/2 \quad (3.4)$$

Finally, the lift coefficient at zero angle of attack is given by the following:

$$C_{l0} = -\alpha_0(a_1)_0 \quad (3.5)$$

Here, Pankhurst suggests the usage of thin airfoil theory's  $2\pi$  approximation for the inviscid lift curve slope  $(a_1)_0$ . In this thesis work, it is suggested to replace thin airfoil theory's  $2\pi$  with an empirical method to obtain a better approximation of the lift at zero incidence. Hereby, the empirical table-lookup method of Datcom [12] is suggested. Datcom's approach to determine the theoretical lift curve slope is given as follows:

$$(c_{l\alpha})_{\text{theory}} = 6.28 + 4.7t/c(1 + 0.00375\phi_{\text{TE}}) \quad (3.6)$$

Hereby, the theoretical lift curve slope is corrected for both compressibility effects and viscous effects which depend on Reynolds number, see Equation 3.8 and the trailing-edge airfoil angle  $\phi_{\text{TE}}$ , see the following equation:

$$c_{l\alpha} = \frac{1.05}{\sqrt{1 - M^2}} \left[ \frac{c_{l\alpha}}{(c_{l\alpha})_{\text{theory}}} \right] (c_{l\alpha})_{\text{theory}} \quad (3.7)$$

$$Re = \frac{\rho V l}{\mu} \quad (3.8)$$

The viscous effects are included within the  $\frac{c_{l\alpha}}{(c_{l\alpha})_{\text{theory}}}$  correction factor which is based on a large body of experimental data. The empirical data obtained for this ratio is depicted in Figure 3.3 for a regular and cusped trailing edge. As such, the effects of Mach number, airfoil thickness, trailing edge geometry and, Reynolds number are, to a certain degree, accounted for in the analysis of the lift at zero incidence when this scheme is implemented.

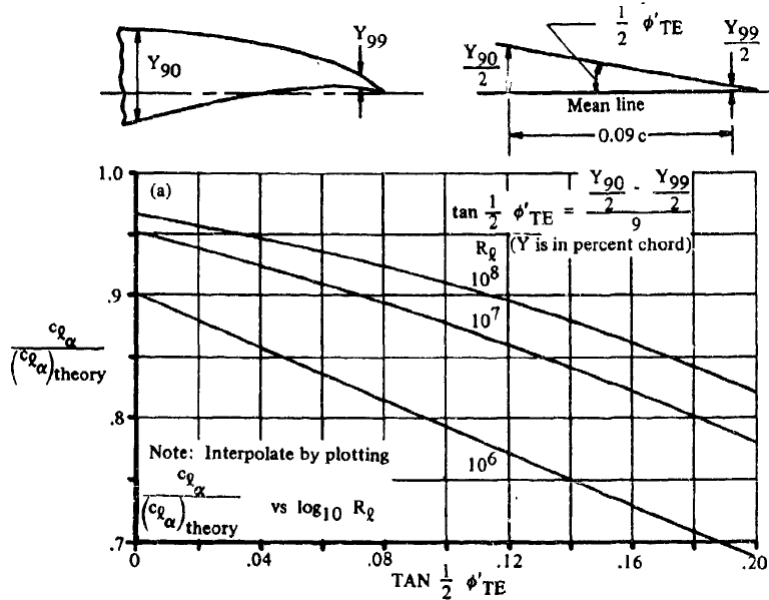


Figure 3.3: Correction factor for the theoretical lift curve slope according to Datcom [12]

#### MACH FACTOR $F_M$ AND MODERN AIRFOIL FACTOR $F_S$

Analysis of measured data has revealed that modern rear loaded airfoils that terminate with a weak trailing-edge shock, have a higher maximum lift coefficient than conventional airfoil with similar  $z_{u1.25}/c$  and  $\tau_u$  values. Therefore, Hollis and Williams [42] introduced the factor  $F_S$  which accounts for this effect. This factor can be obtained from Figure 3.4 as function of Reynolds number and is equal to one for conventional airfoils. Similarly, the compressibility effects on the  $c_{l\max}$  which were discussed in Section 2.3.5 are accounted for accordingly. Hereby, Hollis and Williams correlated experimental data which resulted in the following relation:

$$F_M = 1 - F_1 F_2 \quad (3.9)$$

Hereby, the factors  $F_1$  and  $F_2$  can be read from Figure 3.5a and Figure 3.5b respectively. From these Figures it is also evident that both  $F_1$  and  $F_2$  are positive in the considered Mach number range which indicates that  $F_M < 1$ .

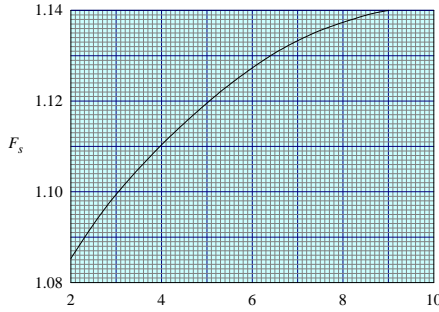
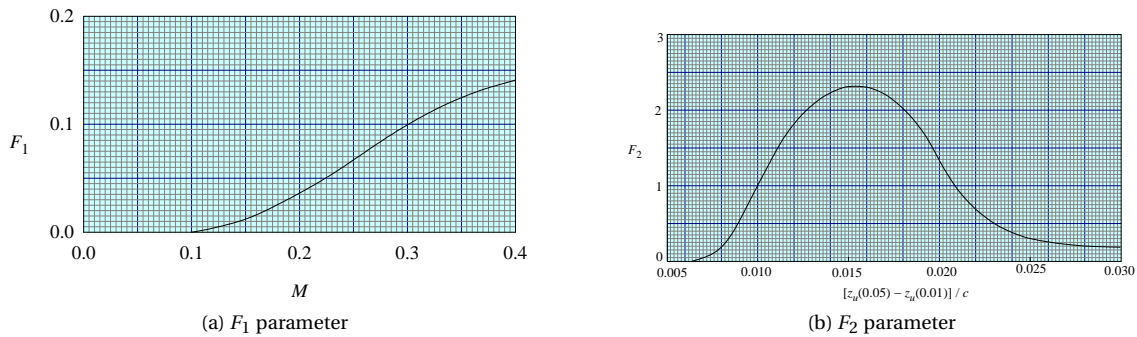
Figure 3.4: Correction factor on the  $c_{l_{\max}}$  for airfoils with rear loading [42]

Figure 3.5: Factors that correct the computed maximum lift coefficient for Mach number effects [42]

## DISCUSSION

The presented  $c_{l_{\max}}$  prediction method has also been validated by Hollis and Williams. Hereby, experimental  $c_{l_{\max}}$  data had been grouped by airfoil type and surface conditions. This yielded a data-set of 220 different airfoils which have been utilized to validate ESDU's empirical  $c_{l_{\max}}$  prediction method. The conducted validation showed an average standard deviation of 0.08, which is deemed acceptable for a conceptual design approach.

Datcom [12] also conducted research on the current matter. Hereby, Finck [12] also established an empirical table-lookup method for the prediction of  $c_{l_{\max}}$ . However, this method omits the effects of compressibility and does not distinguish between front-loaded and rear-loaded airfoil. Therefore the  $c_{l_{\max}}$  prediction method established by IHS ESDU is preferred.

A critical view on the method developed by Hollis and Williams reveals that the implementation of this method, as discussed in this section, incorporates several bottlenecks. For one, the data presented in both Figure 3.2a and Figure 3.2b incorporate an amount of uncertainty. This region of uncertainty is depicted by the dashed red lines in both these figures. Also, implementing this method to determine the maximum wing section lift coefficient on a swept-back wing is impossible. Section 2.3.3 revealed that the local maximum lift coefficient on a swept-back wing differs from two-dimensional computations due to a natural boundary layer control phenomena. This effect is omitted within this empirical two-dimensional method when it is implemented at various spanwise sections of a swept-back wing. Therefore, the implementation of this two-dimensional  $c_{l_{\max}}$  prediction method within the Critical Section Method is only applicable to either straight wings or swept-back wings with fences [29].

### 3.1.2. AERODYNAMIC LOADING ANALYSIS USING ATHENA VORTEX-LATTICE SOLVER

It is suggested to use the publicly available vortex-lattice code AVL [41], which is written by Mark Drela, for performing the inviscid three-dimensional wing analysis in the Critical Section Method. This vortex-lattice tool is widely used among aircraft designers since it has shown to be both robust and rapid due to the availability of a batch run [30]. In this Section, the principles behind vortex-lattice methods for wings in clean con-

figurations are briefly discussed. Subsequently, the implementation of AVL is thoroughly discussed, where wing model generation within AVL and the load extraction from AVL are scrutinized. In the following, a brief introduction to vortex-lattice methods is provided.

#### INTRODUCTION TO VORTEX-LATTICE METHODS

A vortex-lattice method is a numerical approach to analyse the inviscid aerodynamic properties of finite wings [43]. Hereby, a finite amount of horseshoe vortices filaments,  $\Gamma_i$ , are superimposed on a paneled grid that represents the wing. A schematic of this can be seen in Figure 3.6. Initially, the strengths of the superimposed vortices filaments are unknown. The goal here is to determine the normal velocity that is induced by the lattice of horseshoe vortices on every panel. To this extent, a bound vortex is located at the panel 1/4 chord position with two trailing vortex lines that are shed from each end towards  $+\infty$ . A schematic overview of this is given in Figure 3.6a. Also, a control point is placed at 3/4 of the panel length.

The normal velocity is made up of a freestream component and an induced flow component. This induced component is a function of strengths of all vortex panels on the wing. Thus for each panel, an equation can be set up which is a linear combination of the effects of the strengths of all panels. Hereby, a matrix of influence coefficients is created which is multiplied by the vortex strengths and equal to a right hand side vector of freestream effects:

$$\sum_{j=1}^N A_{ij} \Gamma_j = -V_\infty \sin(\theta) \quad (3.10)$$

The influence coefficient  $A_{ij}$  will represent the induced flow on panel i due to the vortex on panel j. By applying the flow-tangency boundary conditions at the control points a system of equations is obtained which can be solved for the unknown horseshoe vortex strengths  $\Gamma_i$ . Subsequently, the Kutta-Joukowski theorem can be implemented, see Equation 3.11, to obtain the aerodynamic properties of a wing at a defined freestream condition.

$$L_i = \rho_\infty V_\infty \Gamma_i \quad (3.11)$$

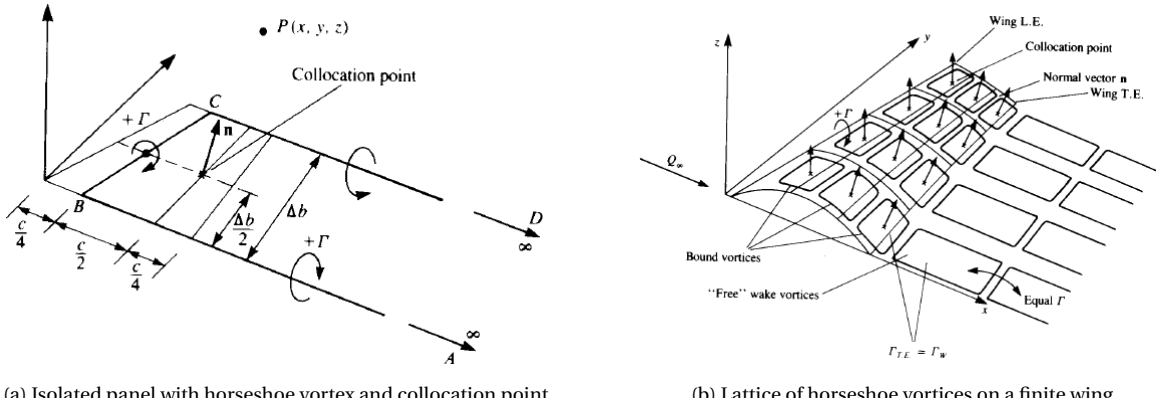


Figure 3.6: Schematic overview of a vortex-lattice method [43]

While implementing an inviscid vortex-lattice method, one needs to take the following assumptions into account [41].

- A vortex-lattice method is best suited for configurations consisting mainly of thin lifting surfaces at small angles of attack and sideslip angles.
- Surfaces and trailing wakes are represented as single-layer vortex sheets, the trailing legs of horseshoe vortex filaments are assumed parallel to the x-axis. This is illustrated in Figure 3.6b.
- Quasi-steady flow is assumed. Whereby, unsteady vorticity shedding is neglected.
- Compressibility effects are treated by implementing the Prandtl-Glauert compressibility correction. This is expected to be valid for a Mach number up to 0.6.

### AVL SOFTWARE SET-UP

AVL is a Fortran based [41] source code for the inviscid aerodynamic analysis of lifting surfaces. Two methods exists for the implementation of AVL, one is using AVL through a command window where commands are directly entered after which an analysis is performed by AVL. The second, and most attractive method, is to run AVL in batch mode from within MatLab. Hereby, a set of commands are documented in a text file and are subsequently passed to the Fortran code of AVL.

For both application methods, a set of input files need to generated prior to the analysis. A brief summary is provided in the following:

- **Geometry input file (.avl):** the geometrical input file describes the complete wing geometry and the settings of the grid generation.
- **Airfoil data file (.dat):** contains all the normalized and derotated airfoils shapes to determine the local wing camber. These coordinates files are subsequently loaded in the geometry input file.
- **Runcase input file (.run):** in the runcase file, the flight conditions are specified.
- **Mass input file (.mass):** in the optional mass input file all the respective component weights are documented to enable the estimation of the center of gravity.
- **Command file (.dat):** contains the running commands for AVL. Hereby, the geometry file along with the runcase input file are loaded. Also, commands are provided to save computed analyses.

In order to successfully implement AVL, one has to adhere to modeling rules which pertain to every vortex-lattice model, i.e. ensuring a proper lattice structure and smooth vortex spacing [41]. Hereby, proper is defined as vortex-lattices having a smooth vortex spacing at locations where rapid changes in vortex-strengths occur. Also, a proper vortex-lattice avoids vortex legs passing through collocation points that are downstream of the wing. Taking these into account, the following function has been written in MatLab in order to be able to perform a batch run within the Initiator:

$$[\text{Aerodynamic Properties}] = \text{AVL}(\text{Wing Geometry}, M_\infty, \alpha, c_{l_a}) \quad (3.12)$$

### VORTEX-LATTICE MODEL GENERATION FOR AVL

An equivalent wing is build to approximate the geometry of an actual wing. The required geometric features are documented within the mentioned geometry input file. To build the equivalent wing, the following steps are taken:

- Initially, the freestream conditions at which the wing is to be analyzed is documented in the runcase file.
- Then, the symmetry cases are specified. Hereby, one can specify run cases for both a mirrored or isolated full span wing.
- Subsequently, the reference wing area, mean aerodynamic chord and reference wing span are documented. AVL uses these parameters to determine the aerodynamic characteristics of the wing under scrutiny.
- This is followed by the definition of the wing shape. Hereby, a wing section geometry file is defined at every spanwise discontinuity. Discontinuities such as kink breaks, wing root, wing tip and local taper change all require an airfoil definition.
- Along side these wing section geometry files, the local chords, lift curve slopes and inclination angles of the respective airfoils are defined.
- Then, a vortex-lattice grid is created between all the defined wing sections by linear interpolation. Here, the chordwise and spanwise spacing setting of vortices is defined. Hereby, a cosine spacing setting is applied to bunch vortex panels at positions where large vortex strength changes occur.

A successful implementation of this scheme yields the vortex-lattice grid which is depicted in Figure 3.7. In AVL, surfaces and trailing wakes are represented by single-layer vortex sheets where trailing vortex legs are parallel to the x-axis. This implicates that the geometry of the wing itself is not rotated due to airfoil incidence angle or wing angle of attack. Instead, the flow-tangency boundary condition is modified on the airfoil camber line. As an example of this modelling technique, Figure 3.8 clearly shows the rotation of strip camber lines of a wing with multiple surfaces.

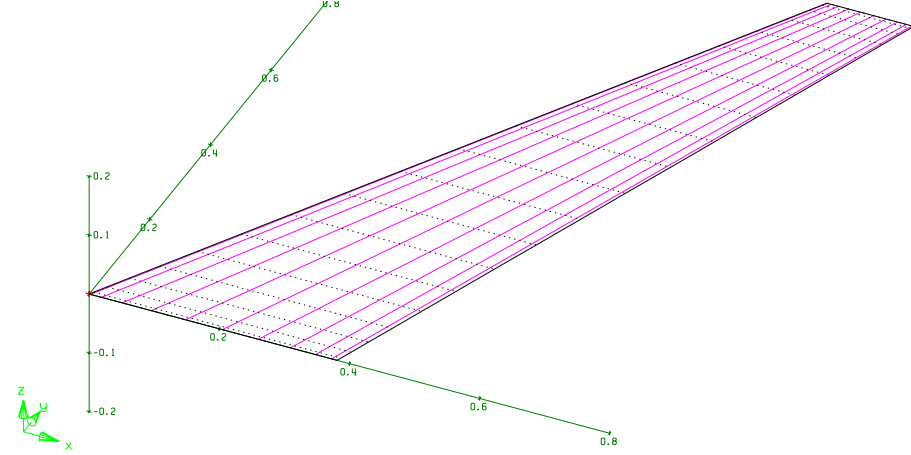


Figure 3.7: Vortex-lattice grid for a clean wing with a surface area of  $0.55 \text{ m}^2$ , span of 2.15m, a taper ratio of 0.35, quarter chord sweep of  $28^\circ$  and an aspect ratio of 8.35

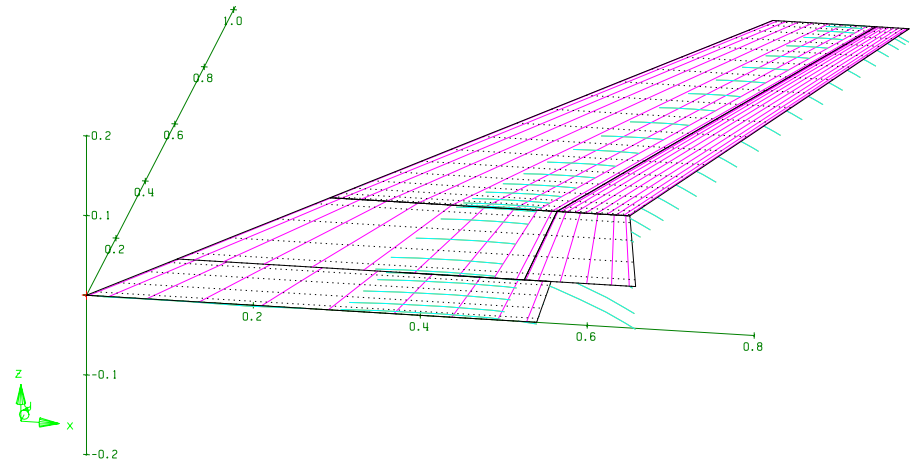


Figure 3.8: Change in flow-tangency boundary condition for a multi-surface wing where the trailing surface is deflected by  $40^\circ$ . The wing has a surface area of  $0.61 \text{ m}^2$ , span of 2.15m, a taper ratio of 0.25 and an aspect ratio of 7.53

For the proper modelling of a wing using vortex-lattice methods, one needs to adhere to a set of rules [41]. To summarize, Trailing vortex legs are not allowed to closely pass downstream control points. This implies that surfaces which are lined up in the chordwise-direction must have the exact same spanwise vortex spacing. Also, spanwise vortex spacing must be smooth, no sudden changes in strip width are allowed. Bunched spacing is required at positions where the circulation changes rapidly; i.e. at taper, dihedral and chord brakes, as well as at control surface ends and especially at wing tips. On behalf of this, a cosine distribution can be successfully implemented. Finally, if a control surface is present, the discontinuity in camber line angle needs to be modelled with an adequate amount of chord wise vortices at the hinge line. Again, a chordwise cosine distribution of control points is suggested.

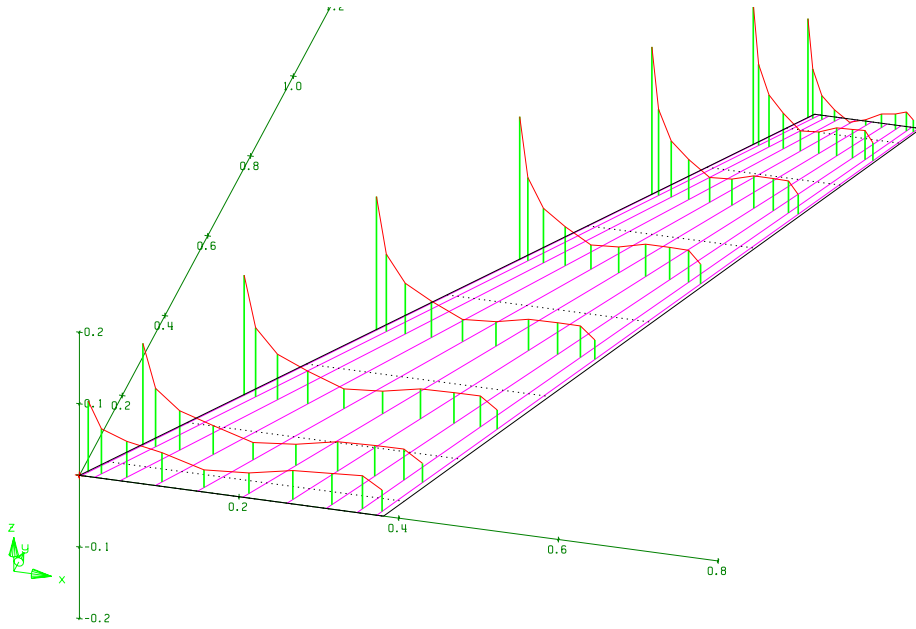


Figure 3.9: Spanwise loading on a clean wing at  $\alpha = 5^\circ$ . The wing has a surface area of  $0.61 \text{ m}^2$ , span of 2.15m, a taper ratio of 0.25, quarter chord sweep of  $28^\circ$  and an aspect ratio of 7.53

### 3.1.3. COUPLING OF AVL AND THE $c_{l_{\max}}$ ANALYSIS

At this points, a method to determine a section's maximum lift coefficient and a method to perform an aerodynamic analysis have been discussed in Section 3.1.1 and Section 3.1.2 respectively. To couple them, several function are developed within MatLab. The function depicted in Equation 3.13 is written to determine the lift curve slope of a wing section. This function is based on the theory that is presented in Section 3.1.1.

$$[C_{l_\alpha}] = \text{SectionLiftCurveSlope}(\text{Airfoil Coordinates}, Re, M_\infty) \quad (3.13)$$

The output of this lift curve slope function is coupled to a MatLab function to batch run AVL, see Equation 3.14. This function is based on the previous discussion on Athena Vortex Lattice and accounts for all the discussed limitations while adhering to the rules of creating vortex-lattice models. Also, it can be seen that AVL requires an angle of attack input to obtain data on both the span loading and wing lift coefficient. The angle of attack is increased in an iterative manner until the computed span loading is tangent to the spanwise distribution of  $c_{l_{\max}}$ .

$$[\text{Spanloading}, C_L] = \text{AVL}(\text{Wing Geometry}, M_\infty, \alpha, C_{l_\alpha}) \quad (3.14)$$

To this extent, a function has been written to determine the spanwise  $c_{l_{\max}}$  at several wing stations,  $\eta = y/(b/2)$ . At these stations, the lift curve slope is determined with Equation 3.13. Then, Equation 3.15 is used along with the lift curve slope at every station to obtain a spanwise distribution of local maximum lift coefficient. Finally, the local  $c_{l_{\max}}$  at every wing station is corrected for sweep effects by using the simple-sweep theory as can be seen in Equation 3.16.

$$[c_{l_{\max}}] = \text{Airfoilclmax}(\text{Airfoil Coordinates}, Re, M_\infty, C_{l_\alpha}) \quad (3.15)$$

$$(c_{l_{\max}})_\perp = c_{l_{\max}} \sec^2(\Lambda_{c/4}) \quad (3.16)$$

A thorough explanation of these MatLab functions is given in the part II of this thesis. A flow chart of the implementation of the Critical Section Method is presented in Figure 3.10.

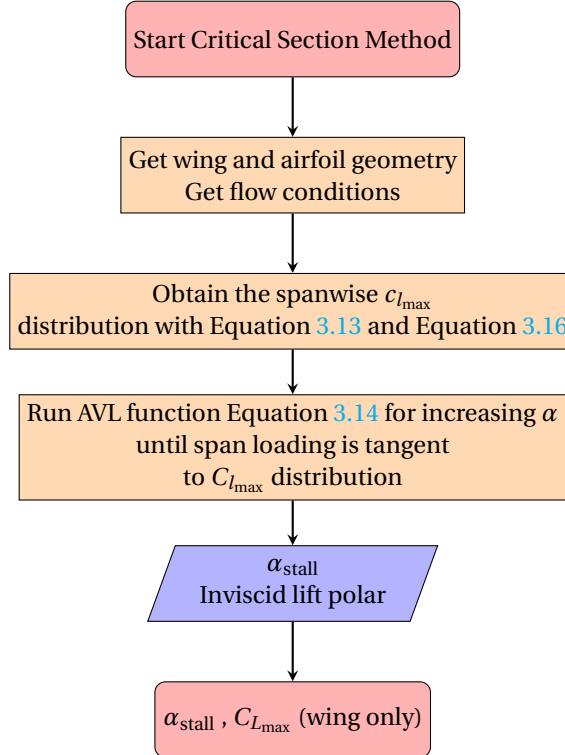


Figure 3.10: Flow chart of the Critical Section Method for clean  $C_{L\text{max}}$  prediction as implemented in this thesis

### 3.2. PRESSURE DIFFERENCE RULE IMPLEMENTATION

In Section 2.4.9, a trade-off between several methods to predict maximum wing lift coefficient was conducted. Here, it was found that not only the Critical Section Method was suitable for predicting maximum lift within the bounds of this thesis, but also the Pressure Difference Rule. This semi-empirical method was introduced in Section 2.4.7. Here, it became evident that both the effective Reynolds number and Mach number are required. Also, an analysis method to determine the effective chordwise pressure difference along the wing span is necessary. To reduce computational expense, van Dam [4] suggests the coupling of a two-dimensional vortex-panel method and a downwash model to approximate the chordwise pressure difference at several wing stations. On behalf of this, the function in Eq 3.17 has been written from the PDR relation from Figure 3.11.

$$\Delta C_{P\text{crit}} = \text{PDR}(M_{\text{eff}}, Re_{\text{eff}}) \quad (3.17)$$

Here the effective Mach number and Reynolds number can be computed from Equations 3.36 and 3.37. In order to account for downwash angle  $\alpha_i$ , the iterative method of Elham [44] is suggested in Section 3.2.2. To obtain an effective pressure difference, a constant vortex-panel method has been constructed that is based on the work of Katz and Plotkin [43] in Section 3.2.1.

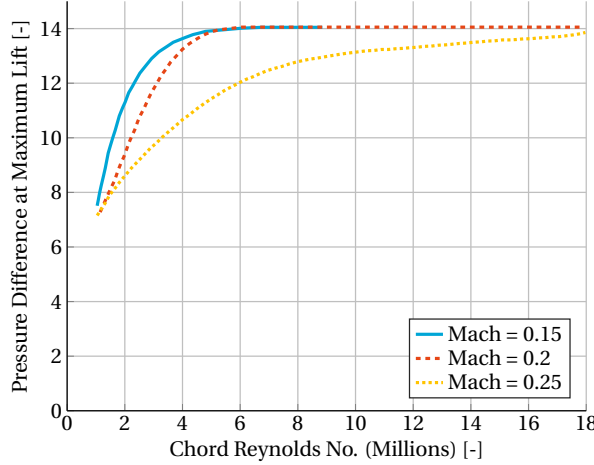


Figure 3.11: Pressure Difference Rule for maximum lift [37]

### 3.2.1. CONSTANT-VORTEX PANEL METHOD

It was decided to write a rapid vortex-panel method within MatLab which is based on the work of Katz and Plotkin [43]. Herein, they discuss several panel methods of which the constant-vortex panel method was selected since it is both rapid and is as accurate as any other low-order panel method. A graphical representation of the constant-strength vortex distribution over an airfoil is presented in Figure 3.12a and a schematic overview of the panel nomenclature is given in Figure 3.12b. Here, the perturbation velocities in the global coordinate system on any collocation point are defined at the center of the panels and are given by Equation 3.18 and Equation 3.19. Solving these perturbation velocities at every panel yields the Aerodynamic Influence Matrix (AIC) where the influence coefficient  $a_{ij}$  is calculated with Equation 3.20. The influence coefficient of a panel on itself is given by Equation 3.21.

$$u_i = \frac{\Gamma_i}{2\pi} \left[ \tan^{-1} \frac{z-z_2}{x-x_2} - \tan^{-1} \frac{z-z_1}{x-x_1} \right] \cos(\alpha_i) - \frac{\Gamma_i}{4\pi} \ln \frac{(x-x_1)^2 + (z-z_1)^2}{(x-x_2)^2 + (z-z_2)^2} \sin(\alpha_i) \quad (3.18)$$

$$w_i = -\frac{\Gamma_i}{2\pi} \left[ \tan^{-1} \frac{z-z_2}{x-x_2} - \tan^{-1} \frac{z-z_1}{x-x_1} \right] \sin(\alpha_i) - \frac{\Gamma_i}{4\pi} \ln \frac{(x-x_1)^2 + (z-z_1)^2}{(x-x_2)^2 + (z-z_2)^2} \cos(\alpha_i) \quad (3.19)$$

$$a_{ij} = (u, w)_{ij} \cdot \vec{x}_p \quad (3.20)$$

$$a_{ii} = -1/2 \quad (3.21)$$

The Right Hand Side (RHS) for every panel is determined by transforming the freestream velocities to the global coordinate system with Equation 3.22. Here, the definition of the tangential vector  $\vec{x}_p$  is given in Figure 3.12b. Finally, the strengths of the vortices are determined by solving Equation 3.23 which is expanded in Equation 3.24. To obtain a solvable systems, the Kutta condition in Equation 3.25 has been utilized.

$$\text{RHS} = -(U_\infty, W_\infty) \cdot \vec{x}_p \quad (3.22)$$

$$\text{AIC} \cdot \Gamma = \text{RHS} \quad (3.23)$$

$$\begin{pmatrix} a_{11} & \dots & \dots & a_{1N} \\ a_{21} & a_{22} & \dots & a_{2N} \\ \vdots & \vdots & \ddots & \vdots \\ a_{N-1,1} & a_{N-1,2} & \dots & a_{N-1,N} \\ 1 & 0 & 0 & 1 \end{pmatrix} \cdot \begin{pmatrix} \gamma_1 \\ \gamma_2 \\ \gamma_3 \\ \vdots \\ \gamma_N \end{pmatrix} = \begin{pmatrix} \text{RHS}_1 \\ \text{RHS}_2 \\ \vdots \\ \text{RHS}_{N-1} \\ 0 \end{pmatrix} \quad (3.24)$$

$$\gamma_1 + \gamma_N = 0 \quad (3.25)$$

Once the strength of the vortices  $\gamma_j$  is known on every panel, the velocities at each collocation point can be determined with Equation 3.26. Also, the pressure coefficient on every panel is determined with Equation 3.27. Finally, the load on every panel is calculated with Equation 3.28.

$$(U_\infty + u, W_\infty + w)_i \cdot \vec{x}_p = 0 \quad (3.26)$$

$$C_p = 1 - \left[ \frac{V_\infty \cos(\alpha + \alpha_1) + \gamma_j/2}{V_\infty} \right]^2 \quad (3.27)$$

$$\sum_{j=1}^N = \rho V_\infty \gamma_j \Delta c_j \quad (3.28)$$

This routine is coded within a MatLab function, see Equation 3.30 and Equation 3.29. Herein, the Aerodynamic Influence Matrix is treated as a constant since it solely depends on wing section geometry. Hence, to save computational expense, the AIC is determined once on every wing span station while the RHS of Equation 3.30 is determined for a spectrum of angles of attack.

$$[\text{AIC}] = \text{InfluenceMatrix}(\text{Airfoil Coordinates}) \quad (3.29)$$

$$[\Delta C_{p_{\text{eff}}}] = \text{ConstantVortex2D}(\text{Airfoil Coordinates}, \alpha_{\text{eff}}, M_{\text{eff}}, \text{AIC}) \quad (3.30)$$

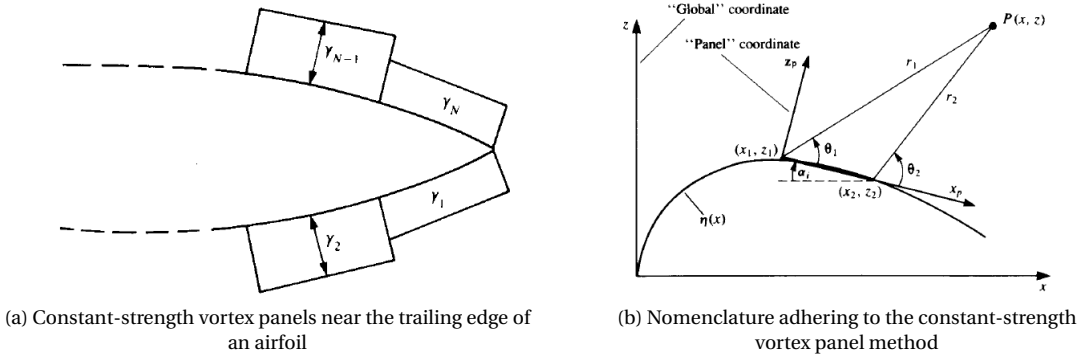


Figure 3.12: Schematic overview of a constant-strength vortex panel method [43]

### 3.2.2. DOWNWASH MODEL

As became apparent, the effective angle of attack is required to obtain the effective pressure difference on a wing section. On this behalf, a downwash model is implemented to determine the effective angle of attack. Hereby, the work of Elham [44] is considered and modified to the current application of the Pressure Difference Rule. The original iterative scheme to determine a wing section's induced angle of attack, as developed by Elham, is depicted in Figure 3.13. Here, it is suggested to implement one of Mark Drela's viscous airfoil analysis tools such as Xfoil [45] and MSES [46]. However, a vortex-panel method implementation is used within this thesis to decrease computational expense because this scheme has an iterative nature.

In the following, the modified downwash model is explained which pertains to a single wing section at constant wing angle of attack. Initially, the span loading at a given geometrical wing angle of attack with respect to the body axis of the aircraft is obtained. To obtain the span loading, the previously discussed vortex-lattice method AVL, which is thoroughly discussed in Section 3.1.2, has been used. This function is conveniently rephrased in Equation 3.31. Hereby, the section lift curve slopes is again determined with the empirical Datcom method which is discussed in Section 3.3.

$$[\text{Spanloading}, C_L] = \text{AVL}(\text{Wing Geometry}, M_\infty, \alpha, c_{l_\alpha}) \quad (3.31)$$

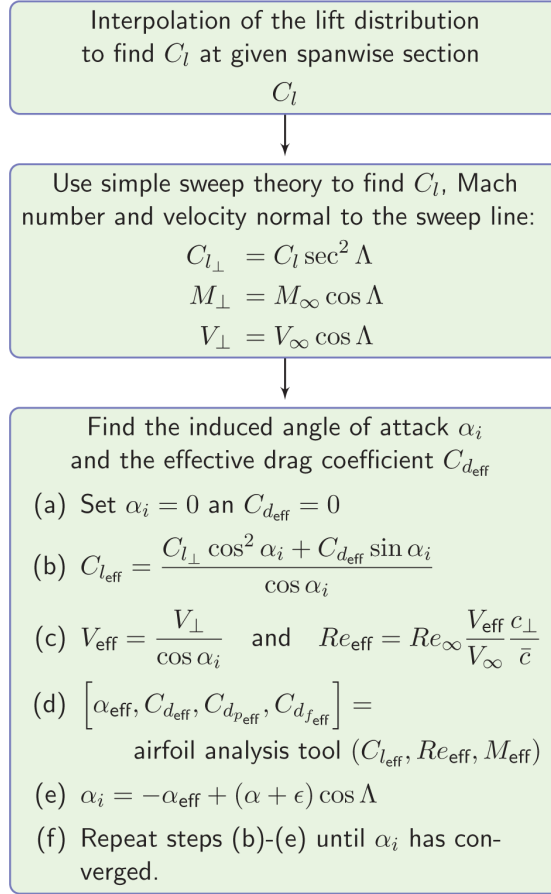


Figure 3.13: Scheme presented by Elham [44] to determine the spanwise downwash distribution

To start, the computed span loading is interpolated to find the local lift coefficient of the scrutinized spanwise wing section. If the wing is swept, use simple-sweep theory to obtain the lift coefficient, Mach number and freestream velocity perpendicular to the wing's quarter chord line. The simple-sweep transformation is given in Equation 3.32.

$$\begin{aligned} C_{l\perp} &= C_l \sec^2(\Lambda_{c/4}) \\ M_{\perp} &= M_{\infty} \cos(\Lambda_{c/4}) \\ V_{\perp} &= V_{\infty} \cos(\Lambda_{c/4}) \end{aligned} \quad (3.32)$$

The induced angle of attack  $\alpha_i$  is initially set to zero within the iterative process, see Equation 3.33. Here, the effective drag coefficient is omitted since the PDR is a purely inviscid method.

$$(\alpha_i)_{\text{initial}} = 0 \quad (3.33)$$

Next, the effective lift coefficient is determined by applying a transformation which depends on the induced angle of attack. This transformation is also done to determine the effective velocity in Equation 3.35. The effective Mach number is determined by dividing the effective velocity  $V_{\text{eff}}$  with the speed of sound  $a$  in Equation 3.36. Similarly, the effective Reynolds number is determined with Equation 3.37.

$$C_{l_{\text{eff}}} = C_{l\perp} \cos(\alpha_i) \quad (3.34)$$

$$V_{\text{eff}} = \frac{V_{\perp}}{\cos(\alpha_i)} \quad (3.35)$$

$$M_{\text{eff}} = \frac{V_{\text{eff}}}{a} \quad (3.36)$$

$$Re_{\text{eff}} = Re_{\infty} \frac{V_{\text{eff}}}{V_{\infty}} \frac{c_{\perp}}{c} \quad (3.37)$$

To determine the wing section's effective angle of attack, the previously described constant-strength vortex panel method is utilized. Hereby, the panel method is utilized to determine the local inviscid lift polar to determine  $\alpha_{\text{eff}}$  at the value of  $C_{l_{\text{eff}}}$ . The function pertaining to this step is given in Equation 3.38.

$$[\alpha_{\text{eff}}] = \text{ConstantVortex2D}(\text{Airfoil Coordinates}, C_{l_{\text{eff}}}, M_{\text{eff}}) \quad (3.38)$$

The induced angle of attack is determined by implementing Equation 3.39. Hereby,  $\epsilon$  is the local twist and the term  $\frac{(\alpha + \epsilon)}{\cos(\Lambda_{c/4})}$  is the geometrical section angle of attack normal the wing's quarter chord line. With this implementation, the induced angle of attack normal to the wing's quarter chord line is obtained. Equation 3.34 until Equation 3.39 encompass a scheme which requires iterations until  $\alpha_i$  has converged. Convergence is reached when the error margin between  $\alpha_i$  and  $\alpha_{i-1}$  is within 1%. A flowchart of this process in presented in Figure 3.14.

$$\alpha_i = -\alpha_{\text{eff}} + \frac{(\alpha + \epsilon)}{\cos(\Lambda_{c/4})} \quad (3.39)$$

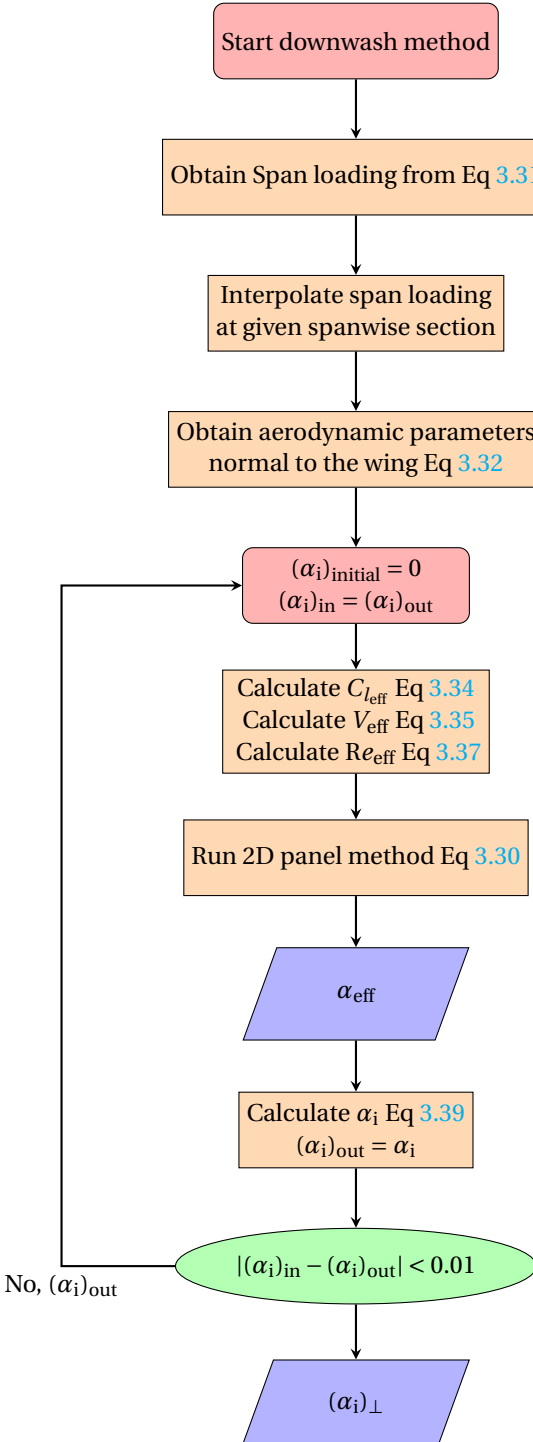


Figure 3.14: Flow chart of the downwash model for the calculation of the induced angle of attack as implemented in this thesis

### 3.2.3. COUPLING OF THE DOWNWASH MODEL AND INVISCID PANEL METHOD

Up until this point, the downwash model and constant-strength vortex-panel method have been thoroughly discussed. This section discusses the coupling of both these schemes to effectively utilize the Pressure Difference Rule. The following goes through the steps that are taken to couple the mentioned methods.

1. Initially, the wing is subdivided by an user-specified amount, usually around 20, of strips. These strips

are bunched at the wing root and wing tip by using a spanwise cosine distribution. See the following figure for a schematic overview:

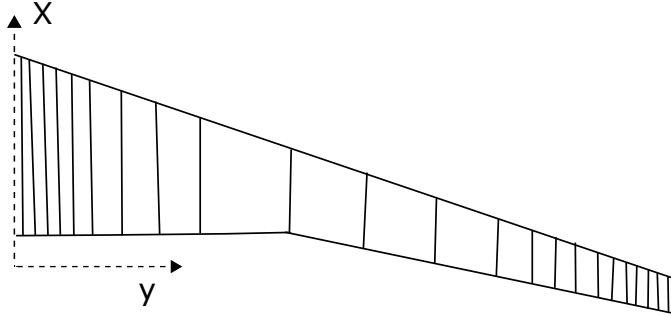


Figure 3.15: Schematic of cosine distributed wing strips at which  $\Delta C_{P_{\text{crit}}}$  and  $\Delta C_{P_{\text{eff}}}$  are to be determined

2. At these strips, the local section lift curve slope is determined with the Datcom method which is discussed in Section 3.3. Also, the Aerodynamic Influence Coefficients are determined at each strip since they solely depend on the local wing geometry with Equation 3.29.
3. Now, the wing angle of attack is set to an initial value, typically around  $0^\circ$ . For subsequent iterations, the wing angle of attack is slightly increased.
4. At the given wing angle of attack, AVL is executed with Equation 3.14 to determine the wing's span loading and inviscid lift coefficient.
5. With the span loading and local, sweep corrected, airfoil geometry, the local induced angle of attack distribution is determined with the scheme that is depicted in Figure 3.14. Hereby, the effective Reynolds number and Mach number are determined for every spanwise wing strip. The critical pressure difference distribution is determined with Equation 3.17.
6. The induced angle of attack at every spanwise location is subsequently used to determine the spanwise distribution of local, sweep corrected, effective angle of attack, see Equation 3.40. The effective angle of attack at every wing strip is used in conjunction with the constant-strength vortex-panel method of Equation 3.30 to determine the effective, sweep corrected, local pressure difference at the given wing angle of attack. Then, both the critical- and effective pressure difference at every wing strip are translated to the freestream direction with Equation 3.41.

$$\alpha_{\text{eff}} = \frac{(\alpha + \epsilon)}{\cos(\Lambda_{c/4})} - (\alpha_i)_\perp \quad (3.40)$$

$$\begin{aligned} (\Delta C_{P_{\text{crit}}})_\infty &= \Delta C_{P_{\text{crit}}} \cos(\Lambda_{c/4}) \\ (\Delta C_{P_{\text{eff}}})_\infty &= \Delta C_{P_{\text{eff}}} \cos(\Lambda_{c/4}) \end{aligned} \quad (3.41)$$

7. Now a check is performed on all spanwise strips to see whether the difference between the local effective pressure difference and critical pressure difference is within an user-specified error margin, which is typically around 1%. If the difference on a spanwise wing strip is within the specified error margin, wing stall is imminent. Else, the wing angle of attack is increased in Step 3 and Step 4 till Step 6 are repeated again until the PDR converges.

Note that the simple-sweep theory has been used within the Pressure Difference Rule implementation to determine the induced angle of attack. A critical attitude is taken towards this. Usage of the simple-sweep theory is only valid in the linear range of the lift polar. However, here it is implemented to determine the maximum wing lift, which is a highly non-linear phenomenon. To justify this, it is argued that the Pressure Difference Rule is a method purely based on inviscid computations while the non-linearities are accounted for by the empirical relations of Figure 3.17. Figure 3.16 displays a flowchart of the Pressure Difference Rule to estimate a wing's clean  $C_{L_{\max}}$ .

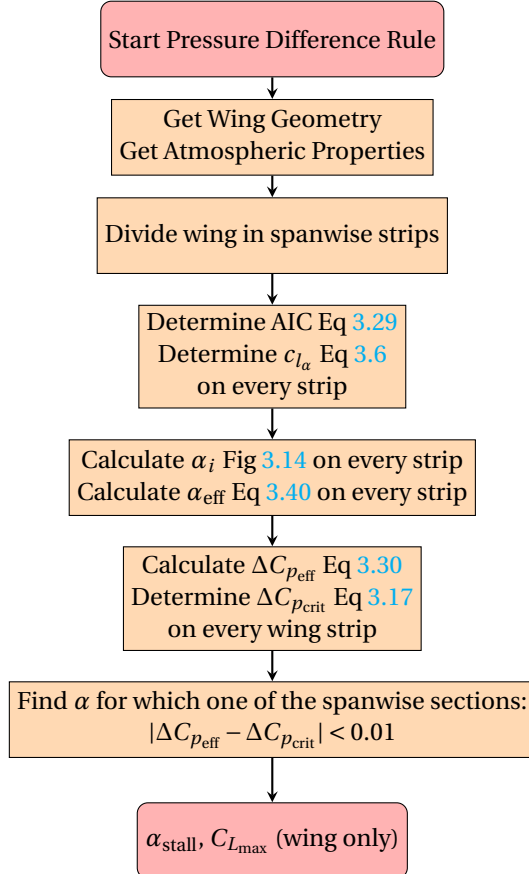


Figure 3.16: Pressure difference rule flow chart for a clean  $C_{L\text{max}}$  prediction

### 3.3. MAXIMUM LIFT COEFFICIENT IN HIGH-LIFT SETTING

At this point, the methodology to approximate the clean maximum lift coefficient has been discussed. However, in Section 2.2.3 we clearly saw that there is a need for high-lift lift device for optimal wing design. Therefore, this section will elaborate further on the methodology to obtain the high-lift maximum lift coefficients.

It was chosen to again utilize the Pressure Difference Rule because it showed remarkably good results when predicting high-lift maximum lift coefficient [37]. However, to implement the Pressure Difference Rule, certain modifications to the clean PDR implementation of Figure 3.16 had to be applied. These modifications include the following:

- A modification to the implemented vortex-lattice to allow for the modelling of multi-element lifting surfaces.
- Extension of the two-dimensional vortex-panel method to model high-lift airfoils.
- Modification of the lift curve slope analysis to account for Fowler motion and flap deflection.
- As purely inviscid methods are utilized, means to distinguish between and effective and geometrical flap deflection was introduced.

In following sections, the stated modifications are thoroughly explained.

#### 3.3.1. HIGH-LIFT VORTEX-LATTICE MODEL

The deflection of a high-lift device effectively changes the local camber of the wing. Also, Fowler motion increases the wing area by translating a flap rearward. Hereby, a gap is formed between the trailing edge of the wing and the leading edge of the trailing flap. The resulting gaps which are created due to Fowler motions on

a Boeing 747-400 are illustrated in Figure 3.17. To account for the effective change in chordwise camber distribution, chord and surface area within the generation of the vortex-lattice grid, the work of Moerland [47] is consulted. Herein, an analysis on trailing edge flap modeling in VLM's is presented. Here, Moerland tested two different gap filling methods, this is graphically shown in Figure 3.18. Here, Moerland found that filling any gap ('grid method 02' in Figure 3.18), with an additional vortex-lattice grid, between the main wing and trailing edge flap resulted in improved spanwise load predictions when compared to actual gap modelling within a VLM. Therefore, in this thesis work, gaps formed due to Fowler motions are filled with additional surfaces.



Figure 3.17: The slotted Fowler flaps of a Boeing 747-400

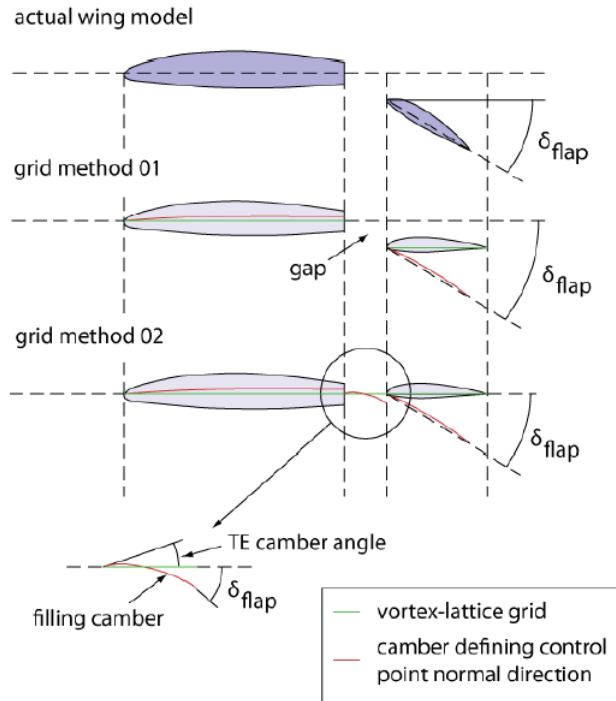


Figure 3.18: Gap filling methods in a vortex-lattice method as been tested by Moerland [47]

A number of restrictions limit the geometrical modelling of the high-lift vortex-lattice grids. As mentioned before, for clean wing vortex-lattice grids in Section 3.1.2; trailing vortex legs are not allowed to closely pass downstream control points, spanwise vortex spacing must be smooth and both spanwise and chordwise dis-

continuities in the wing model locally require denser grid spacing [41]. Also, surfaces which consist out of multiple chordwise surfaces require perfectly aligned grid surfaces to obtain adequate loading results at the flap-wing junction. Hence, the following will discuss the generation of a high-lift vortex-lattice while adhering to the mentioned modelling restrictions.

To build up a high-lift vortex-lattice grid, the wing area is subdivided into multiple surfaces as shown in Figure 3.19. Hereby, an user-specified number of spanwise and chordwise panels are selected per individual surface. A cosine spacing setting is again required to bunch vortex panels at positions where large vortex strength changes occur. The overlap of the clean wing portion to the flapped wing portion is a location where large changes in vortex strength occurs. Hence, applying a cosine spacing on the involved surfaces will yield a bunching of the vortex panels at this overlap. This feature is schematically represented in Figure 3.19.

Care should be taken with spacing the vortex outlining for high-lift wings. Figure 3.22 clearly depicts that a trailing flap surface comes behind the main wing. In order to obtain sensible results, the local vortex spacing on the main wing and the flap surface should be aligned to avoid vortex legs passing through the control points that are located on the flap surface. A schematic of this is presented in Figure 3.19. Here, the vortex legs of the clean surface that lies upstream of the flap, are aligned with the vortex legs of the flap. This can effectively be done by subdividing the high-lift segment of the wing in two separate surfaces, as can be seen in Figure 3.19. Here, the flapped segment of the wing is divided in the "Main flap surface" and the "Flap surface". Subsequently, both these surfaces are given the same spanwise cosine distribution of vortex panels. Because the two surfaces start and end at the same spanwise wing locations, indicated by the red lines in Figure 3.19, the vortex legs will automatically be aligned.

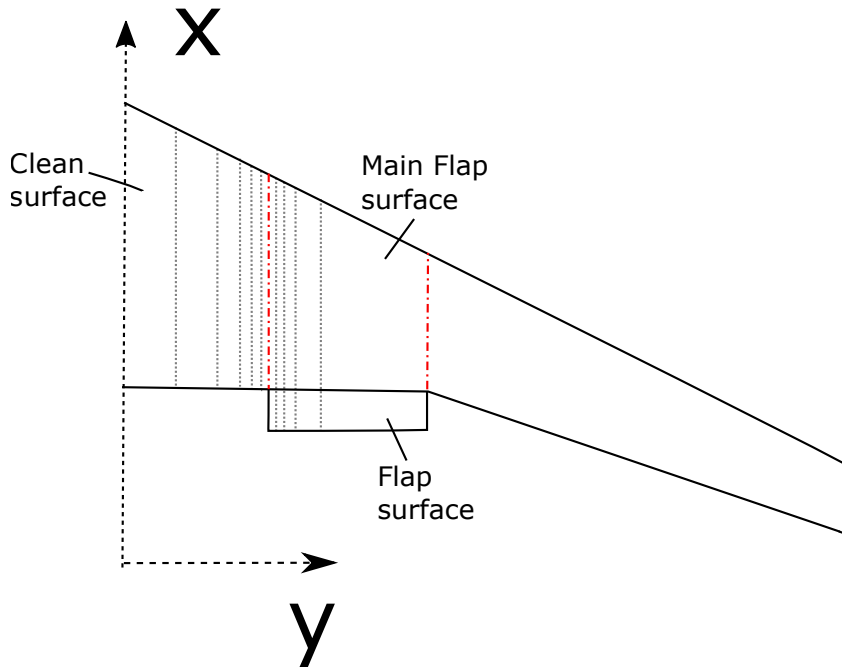


Figure 3.19: Bunching of vortex panels at the overlap of the clean and high-lift wing surfaces. The red lines indicate the junction of two different surfaces and the grey dotted lines represent vortex legs

Also, every implemented surface also requires the definition of a wing section to determine the local camber distribution of the surface. For a multi-element flap, the main airfoil is used to build the surface which lies upstream of the flap. For the flap surfaces itself, the trailing high-lift elements need to be specified at both ends of the flap surfaces. Similarly, the clean airfoil definition is used to build the clean wing surfaces. The mentioned airfoil definitions can also be seen in Figure 3.20 and the spanwise locations of the mentioned wing sections is given in Figure 3.21.

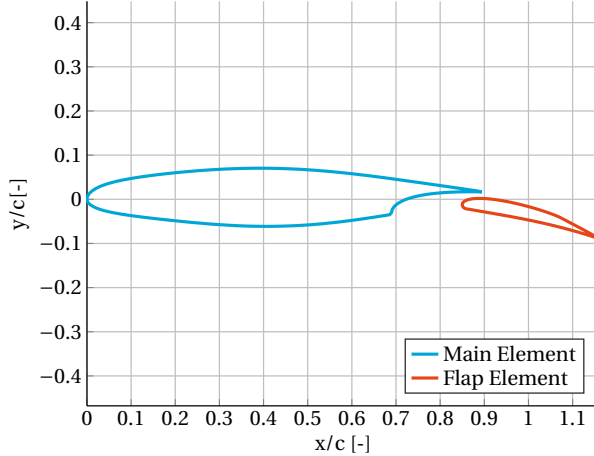


Figure 3.20: Representation of a single-slotted flap with multiple airfoil definition for both the main and flap element

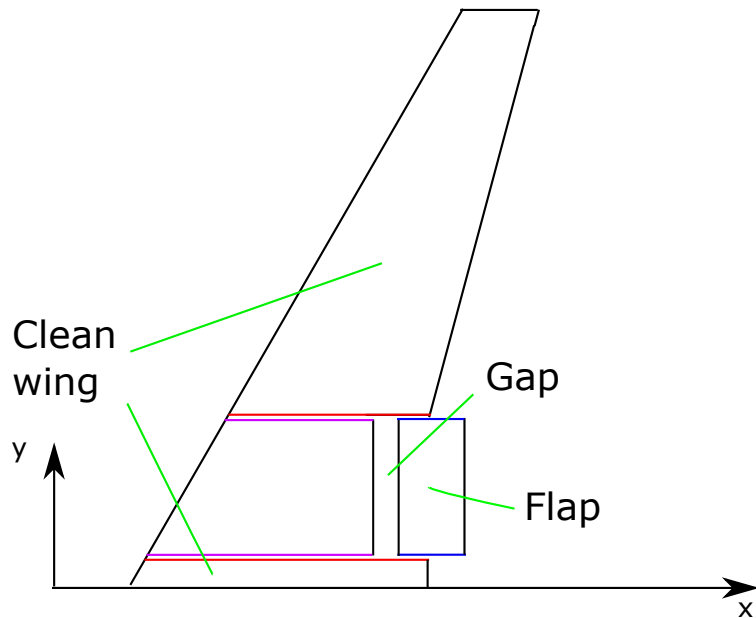


Figure 3.21: Graphical representation of used airfoil definitions at spanwise locations. The red lines indicate the implementation of the clean airfoil. At the blue lines, the flap airfoil is utilized. The main airfoil of the high-lift airfoil configurations is located at the purple lines

Applying the mentioned high-lift vortex-lattice method within AVL yield the vortex lattice that is depicted in Figure 3.22. Here, a typical vortex-lattice as generated by AVL is illustrated. In this figure, the vortex legs of upstream surface are in alignment with the downstream surface that represents the flap. Furthermore, the generated loading on a high-lift kinked wing with a full span trailing-edge Fowler flap is illustrated in Figure 3.23. Here, it can be seen that an effective loading on every individual surface is created, where the depicted spanwise loading distributions all terminate at the leading- and trailing edge of every surface. It is to be tested whether these spanwise loading distributions will yield an adequate inviscid approximation of the lift polar of a high-lift wing. For the interested readers, the geometry file (.avl) to build the high-lift vortex lattice of Figure 3.23 in AVL is given in Appendix A.

Furthermore, since vortex-lattice methods are based on potential flow theory, viscous flow effects are absent in the vortex-lattice flow field. Therefore, the viscous interaction between boundary layers of every high-lift element due to wake shedding is neglected. Also, boundary layer refreshment due to boundary-layer

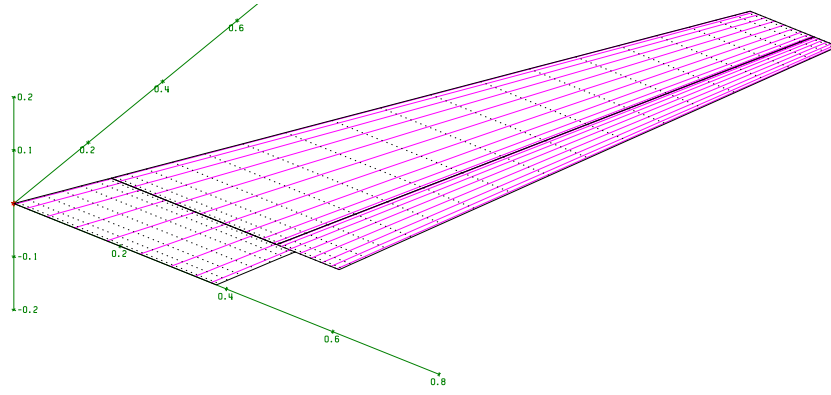


Figure 3.22: Vortex-lattice grid for a high-lift wing with a full span trailing-edge flap. This wing has a surface area of  $0.55 \text{ m}^2$ , span of 2.15m, a taper ratio of 0.35, quarter chord sweep  $28^\circ$  and an aspect ratio of 8.35

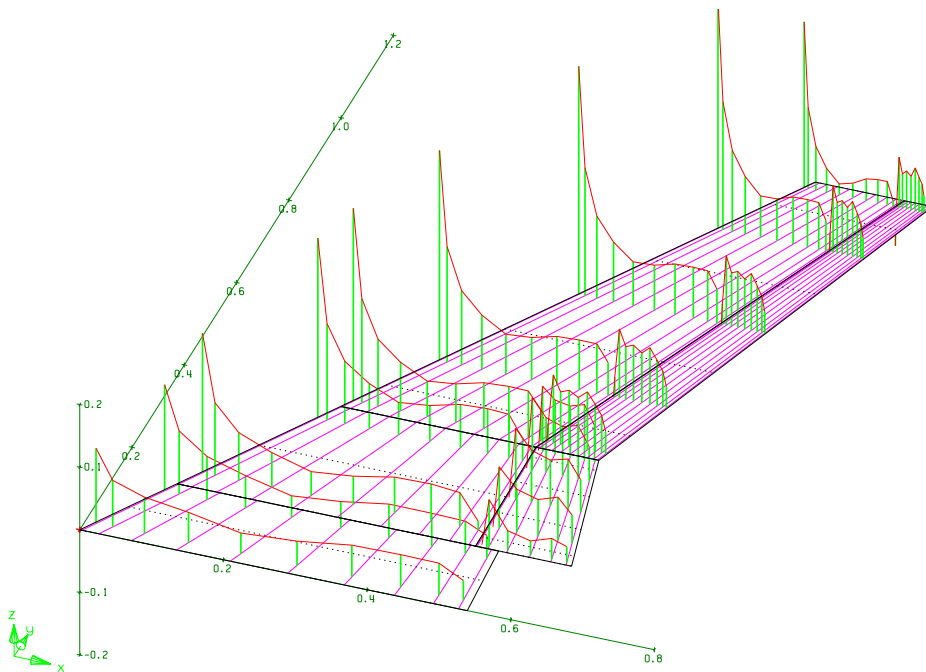


Figure 3.23: Spanwise loading on a multi-surface wing at  $\alpha = 15^\circ$  where the trailing surface is deflected by  $40^\circ$ . The wing has a surface area of  $0.61 \text{ m}^2$ , span of 2.15m, a taper ratio of 0.25 and an aspect ratio of 7.53

flow through slots is completely omitted. However, the circulation effect on both upstream and downstream elements can be successfully captured with this vortex-lattice implementation. This is because the mutual effects of additional circulation due to the deflection of a flap propagates over the total vortex-lattice. Hence, it is to be validated whether the negligence of the viscous effects surrounding high-lift devices is justifiable to determine a high-lift wing's maximum lift coefficient.

### 3.3.2. MULTI-ELEMENT LINEAR-STRENGTH VORTEX PANEL METHOD

The constant-vortex panel method has been extended to determine the pressure distributions over multi-element wing sections. The work of both Cox [48] and again Katz and Plotkin [43] have been consulted in order to build the necessary method. Here, Cox argues that a linear-strength vortex-panel method is necessary to obtain an adequate pressure distribution over a multi-element airfoil. The linear strength-vortex differs from the constant-strength vortex-panel method in the fact that the vortex strength,  $\Gamma$ , is different on both side of the panels. A graphical representation of the linear-strength vortex distribution over a panelled airfoil is presented in Figure 3.24a and a schematic overview of the panel nomenclature is given in Figure 3.24b.

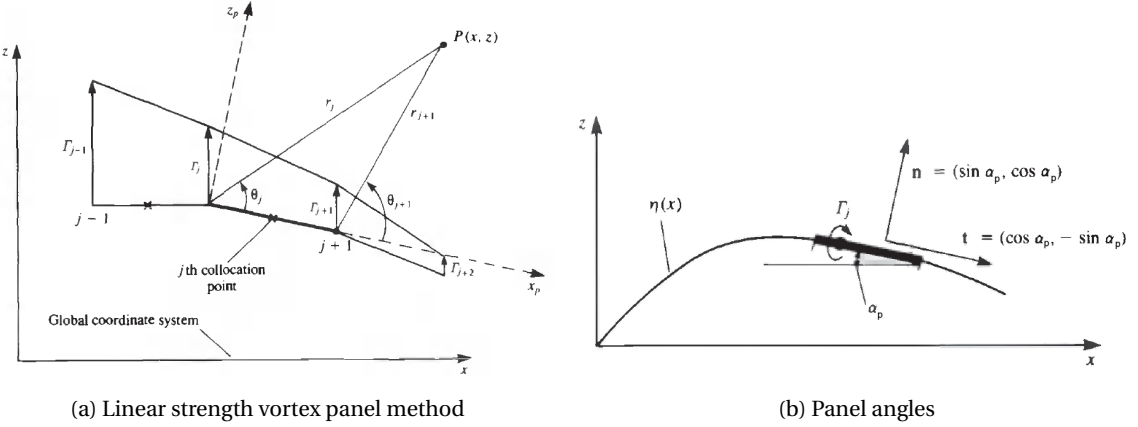


Figure 3.24: Nomenclature used in the linear-vortex panel method [43]

While utilizing the nomenclature given in Figure 3.24b, the perturbation velocities at a specified collocation point are determined at the center of a panel with Equation 3.42 and Equation 3.43.

$$u_p = \frac{z}{2\pi} \left( \frac{\Gamma_2 - \Gamma_1}{x_2 - x_1} \right) \ln \left( \frac{r_2}{r_1} \right) + \frac{\Gamma_1(x_2 - x_1) + (\Gamma_2 - \Gamma_1)(x - x_1)}{2\pi(x_2 - x_1)} (\theta_2 - \theta_1) \quad (3.42)$$

$$w_p = -\frac{\Gamma_1(x_2 - x_1) + (\Gamma_2 - \Gamma_1)(x - x_1)}{2\pi(x_2 - x_1)} \ln \left( \frac{r_2}{r_1} \right) + \frac{z}{2\pi} \left( \frac{\Gamma_2 - \Gamma_1}{x_2 - x_1} \right) \left( \frac{x_2 - x_1}{z} + (\theta_2 - \theta_1) \right) \quad (3.43)$$

Subsequently, the perturbation velocities are transformed from the panel coordinate system to the global coordinate system. Hereby, the coefficients of the Aerodynamic Influence Coefficients (AIC) matrix and the Right Hand Side (RHS) vector are computed with:

$$\mathbf{a} = (u, w) \cdot \vec{\mathbf{n}} \quad (3.44)$$

$$\text{RHS} = -(U_\infty, W_\infty) \cdot \vec{\mathbf{t}} \quad (3.45)$$

Here, the vectors  $\vec{\mathbf{n}}$  and  $\vec{\mathbf{t}}$  are the vectors that are normal and tangential to the local panel respectively. This can also be seen in Figure 3.24b. As in the constant-strength vortex-panel method, a system of equations is obtained, as in Equation 3.24, to solve the vortex strengths on every panel. Therefore, solving Equation 3.46 yields the strengths of the vorices at every panel.

$$\text{AIC } \Gamma = \text{RHS} \quad (3.46)$$

With this, the perturbation velocities at every collocation point on a panel is determined with:

$$V_t = \Gamma \cdot (u, w) \cdot \vec{\mathbf{t}} \quad (3.47)$$

Subsequently, the pressure coefficient at each collocation point is calculated with:

$$C'_p = 1 - \left( \frac{V_{t_\infty} + V_t}{V_\infty} \right)^2 \quad (3.48)$$

Finally, the airfoil's lift coefficient is calculated by summing the lift coefficient contribution of every  $j$ -th panel as shown below:

$$C_l = \sum_{j=1}^N = -C_p \Delta l \cos(\alpha) \quad (3.49)$$

This routine is again coded within a MatLab function, see Equation 3.50 and Equation 3.51. Herein, the Aerodynamic Influence Matrix is treated as a constant since it solely depends on wing section geometry and

flap geometry. Hence, to save computational expense, the AIC is determined only once on every wing span station while the RHS of Equation 3.51 is determined for a spectrum of angles of attack.

$$[\text{AIC}_{\text{linear}}] = \text{InfluenceMatrix}(\text{Airfoil Coordinates}, \text{Flap Coordinates}) \quad (3.50)$$

$$[\Delta C_{p_{\text{eff}}}] = \text{LinearVortex2D}(\text{Airfoil Coordinates}, \text{Flap Coordinates}, c_f, \alpha_{\text{eff}}, M_{\text{eff}}, \text{AIC}_{\text{linear}}) \quad (3.51)$$

### 3.3.3. MULTI-ELEMENT LIFT CURVE SLOPE

The lift curve slope is affected by flap deflections due to several phenomena. To start, the chord extension due to Fowler motions increases the effective airfoil chord. Also, flap deflections alter the effective camber distribution over a multi-element airfoil [3]. In a potential flow point of view, adding and deflecting a flap changes the effects of the singularity distributions on both itself and all other singularities [43]. Finally, The flap's lift effectiveness decreases with angle of attack and flap deflection due to boundary layer interference [49].

In order to obtain an adequate approximation of the high-lift polar of a wing using a vortex-lattice, the effects of deflecting a flap on the lift curve slope should be accounted for. These effects are tackled in a step wise manner in the Pressure Difference Rule approach. To start, the two dimensional lift curve slope of a multi-element wing section is required for the vortex-lattice method. Torenbeek [49] developed a method to both account for the chord extension and flap deflection, see Equation 3.52. Herein, the decrease in lift curve slope due to flap deflection is modeled by a sine function. The accompanied nomenclature of a single-slotted Fowler flap is presented in Figure 3.25.

$$\frac{(C_{l_\alpha})_{\text{high-lift}}}{(C_{l_\alpha})_{\text{clean}}} = \frac{c'}{c} \left( 1 - \frac{c_f}{c'} \sin^2(\delta_f) \right) \quad (3.52)$$

This method is coupled with Datcom's airfoil lift curve slope approximation Equation 3.3 to solve the Left Hand Side (LHS) of Equation 3.52. In this model, the reduction in lift curve slope at large flap angles and high angles of attack due to viscous effects are omitted. Hence, this approach is solely applicable to the linear part of the lift polar.

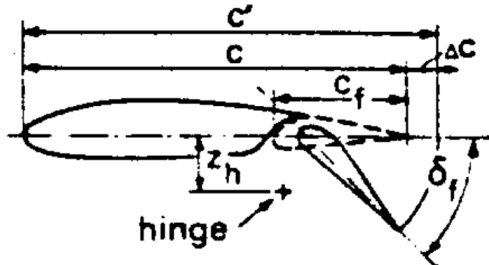


Figure 3.25: Nomenclature used to determine the lift curve slope for single-slotted Fowler flaps [49]

### 3.3.4. FLAP DECAMBERING ANALYSIS

The multi-element vortex-lattice implementation as well as the multi-element vortex-panel method have been discussed. The effective flap angle deflection is another point of discussion. Obert [3] revealed a contrast between the geometrical and effective flap deflection. This contrast originates from effective decambering and flow separation effects which alter the effective viscous camber shape and effective flap deflection [50]. Figure 3.26 depicts a representation of the decambering effect that is caused by boundary layer separation on the trailing edge of the flap. As can be seen from Figure 3.26, the separated wake causes a counter-clockwise rotation of the viscous mean line, which decrease the geometrical flap angle. In the current application of the Pressure Difference Rule, purely inviscid methods are utilized. Therefore, boundary layers are omitted, which also implies that the mentioned flap decambering and boundary layer separation on the flap are omitted.

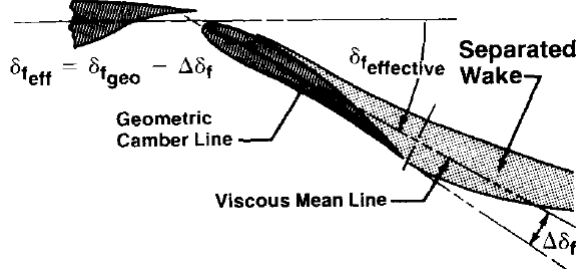


Figure 3.26: Flap decambering reduction curves [50]

To account for these effects, the nominal flap angle versus effective flap angle curves, which are experimentally established by several researchers are scrutinized, see Figure 3.27. These curves are tested accordingly to see which experimental curve yields the most accurate representation of the lift polar for wings in high-lift setting.

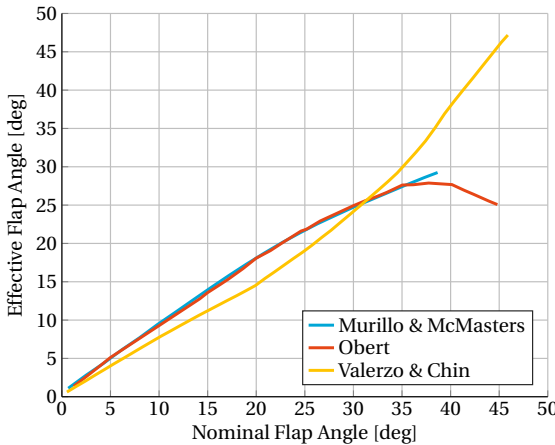


Figure 3.27: Flap angle reduction curves for single-slotted- and plain flaps as per the indicated researchers [3, 37, 50]

### 3.4. AIRFOIL SMOOTHING

It is evident that the current implementation of the PDR heavily depends on inviscid vortex-panel methods. Hereby, the shape of an airfoil is used to obtain the inviscid pressure distribution at a defined angle of attack and Mach number. The distribution of Cartesian coordinates that define the airfoil shape are a point of interest because they dictate the fidelity of the vortex-panel solution.

The mentioned airfoil coordinates are often defined as a list of data points that are sorted by upper- and lower side. Online databases often contain sets of airfoil coordinates that are ranked for every airfoil type. Hereby, it is usually the case that the airfoil coordinates are concatenated within a data- (.dat) or text (.txt) file which starts and ends at the trailing edge of the airfoil. The Initiator uses these airfoil coordinate files abundantly throughout the design routine of an aircraft. Unfortunately, the order of the coordinates, which are given in the data file, do not always start and end at the trailing edge or lack smoothness at the leading- and trailing edge. In rare occasions, there are not enough points to accurately model an airfoil profile.

Therefore, a generic parsing routine is implemented to be able to handle different file formats. Also, a fitting and sampling routine is implemented to ensure airfoil smoothness at the leading- and trailing edge. This effectively increases the fidelity of the computed pressure coefficient distributions which are to be determined with the vortex-panel methods.

Initially, it was considered to implement a Class-function/Shape-function Transformation (CST). This is a

well known method to resample airfoil shapes that found many usages in optimization problems. However, the problem with this method is that it revolves around an optimization procedure to fit the specified CST coefficients to a profile. This showed to be time consuming, therefore, the following is proposed:

### 3.4.1. AIRFOIL PARSING

Initially, the airfoil coordinates are imported within MatLab's working directory. Hereby, the upper- and lower sides of the airfoil coordinates are identified. Subsequently, the airfoil coordinates are rotated and scaled to ensure that the leading edge is located at  $(0, 0)$  and the trailing edge is located at  $(1, 0)$ . Then, the airfoil coordinates are reordered to a concatenation of coordinates which starts with the upper trailing-edge coordinates and ends with the lower trailing-edge coordinates of the airfoil. While doing so, the leading-edge point  $(0, 0)$  is only included once to ensure the continuity of airfoil coordinates.

If the scrutinized airfoil has a blunt or open trailing edge, the airfoil is subsequently closed. This has been done by again rotating and scaling the airfoil. Then, the trailing edges of both the upper-and lower sides are placed symmetrically around  $(1, 0)$ . Subsequently, the airfoil is closed by adding a coordinate point at  $(1 + 10^{-6}, 0)$  for both the upper- and lower airfoil surface. The small increment in x-direction ensures a monotonic increase of x-coordinates, a feature that is necessary for interpolation and extrapolation schemes. Hereby, it is assumed that the incremental increase in chord is small enough to be ignored. This routine has been written as a MatLab function within the airfoil geometry class of the Initiator, the function definition can be seen in Equation 3.53.

$$[(\text{Airfoil Data})_{\text{parsed}}] = \text{AIRFOILPARSE}(\text{Airfoil Data}) \quad (3.53)$$

### 3.4.2. AIRFOIL SAMPLING

To obtain a smooth airfoil, the mean camber line of the airfoil is subtracted and the airfoil coordinates are transformed to radial coordinates. Then, a cubic spline fit is applied to the resulting airfoil at both the leading- and trailing edge. Removing the mean camber line removes trailing edge cusps, which are often found on supercritical airfoils, and guarantees a constant symmetrical shaped distribution of airfoil coordinates. This yields the symmetric thickness distribution of the airfoil, which is guaranteed to be of constant curvature. Hence, this implies that a transformation from Cartesian to radial coordinates yields a monotonically increasing data set that is suitable for a cubic spline fit.

#### CAMBER REMOVAL

To remove the camber distribution, it is necessary to fit both the leading- and trailing edge of the considered airfoil instead of a total fit of the airfoil's mean camber line. This is because the airfoil's camber line is dependent on the distribution of airfoil coordinates, which is not guaranteed to be smooth. Therefore, the camber line of the airfoil is initially approximated. This is viable since the approximated camber distribution can be subtracted and later in the process be again added. This effectively removes any generated errors in the camber line approximation. This is very effective for airfoils with limited points on the leading edge since large jumps in the camber lines are remedied. An example of the camber removal can be seen in Figure 3.28.

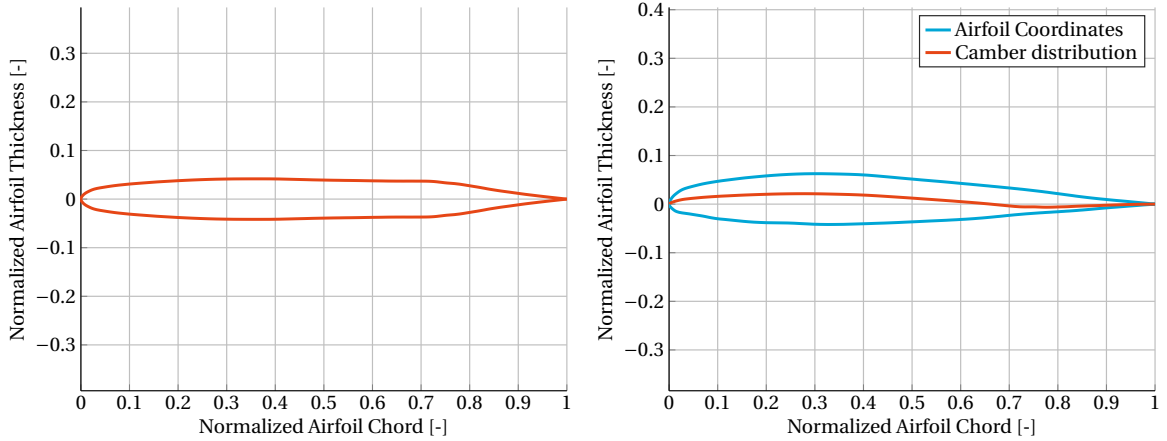


Figure 3.28: Removal of the mean camber distribution on the Boeing747-100b airfoil

#### RADIAL COORDINATE TRANSFORMATION

Now, the considered airfoil is symmetric as can be seen in Figure 3.28. This symmetrical airfoil that is defined in Cartesian coordinates is now transformed to the smoother radial coordinates to increase the point density at the leading- and trailing edges and to cope with the infinite slope at the leading edge. The resulting radial coordinate distribution for the Boeing-737 root airfoil is displayed in Figure 3.29. Here, it is seen that the radial coordinate is rapidly changing, which is expected for an airfoil with a pointed trailing edge. This rapid change can be dictated to one's need by shifting the origin of the radial transformation closer or further away from the trailing edge. Finally, a cubic spline fit is performed by using MatLab's Curve Fitting Toolbox. Here, the leading edge is defined by  $\theta = -\pi/2$ , where the gradient of the fit is set to zero. This effectively prevents the overestimation of the radius at the leading edge. This overestimation results in points with  $x < 0$  at the leading edge, which is clearly not possible since this yields a leading edge protrusion.

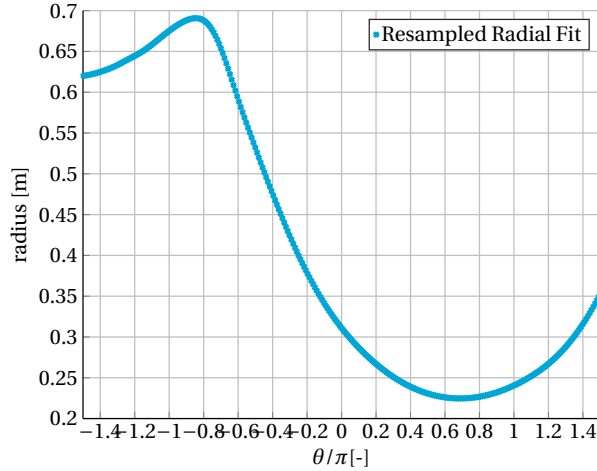


Figure 3.29: Radial coordinates distribution for the Boeing737 root airfoil

Subsequently, the radial coordinates are transformed back to the Cartesian coordinates. These Cartesian coordinates are again parsed so that the airfoil is again normalized de-rotated. Here, 60 data points per airfoil side are chosen to obtain a reasonable size of airfoil coordinates.

#### 3.4.3. TEST CASE SAMPLING

Figure 3.30 yields the parsing result of the discussed scheme. Here, the original Boeing 747 airfoil, which is obtained from an online database, shows a horizontal line which divides the upper side and lower side of the airfoil. With the parsing routine, this line is effectively removed as can be seen in the resampled Boeing 747

airfoil in Figure 3.30.

Figure 3.31 illustrates the effects of the discussed resampling. It is clearly evident that the resampled airfoil shows increased smoothness at the leading edge compared to the original airfoil. Also, Figure 3.31 clearly illustrates the achieved quality of the modelled pressure distribution. The main downside is that one is not using the identical user-defined airfoil shape since the leading edge is being approximated by the cubic spline fit. The same holds for implementing a Class-function/Shape-function Transformation since this method also approximates the shape of an airfoil until a pre-defined optimization criteria is met.

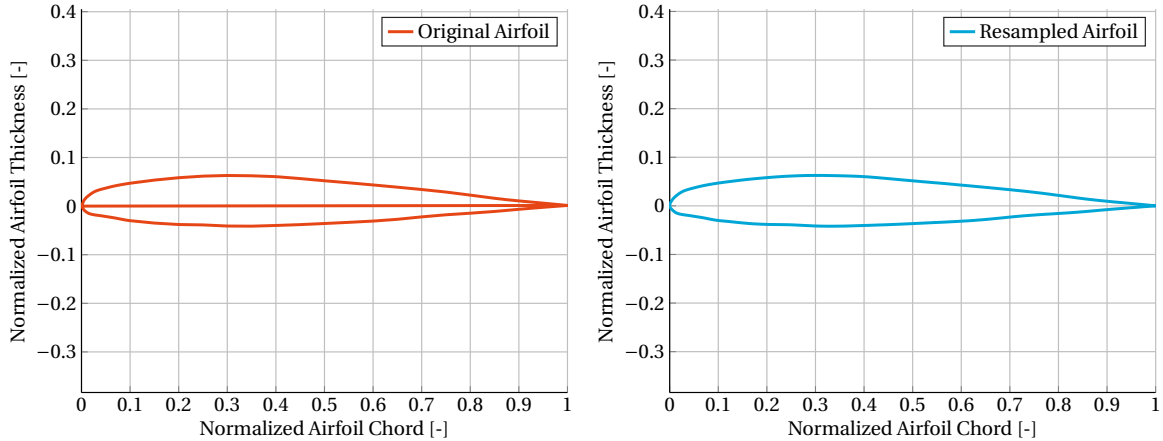


Figure 3.30: Comparison between the original Boeing747-100b airfoil and the resampled and parsed airfoil coordinates

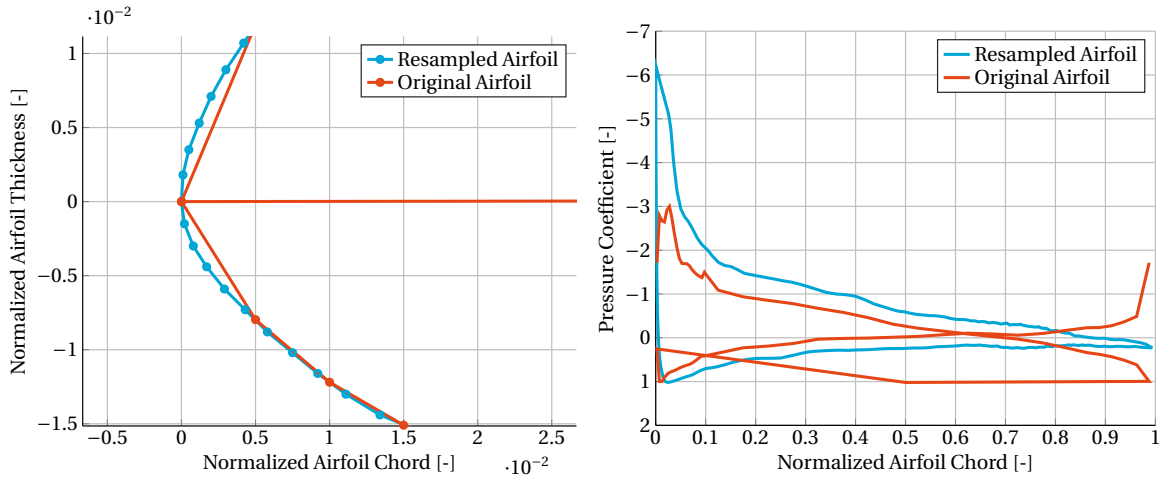


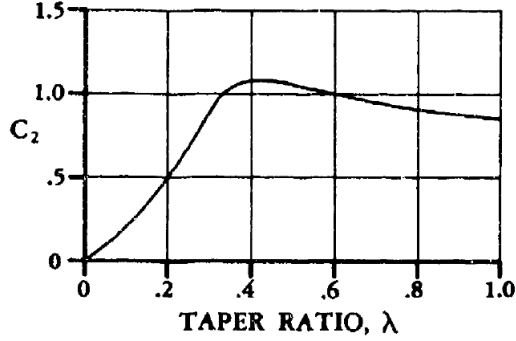
Figure 3.31: Boeing747-100b airfoil - Comparison between resampled and original airfoil coordinates.

### 3.5. FUSELAGE CORRECTION

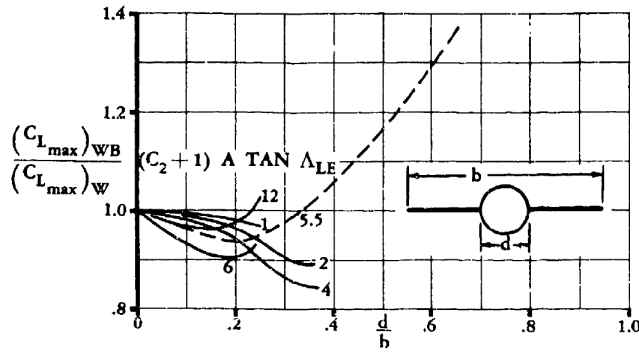
Up until now, means to determine the isolated wing maximum lift coefficient have been discussed. Adding a body of revolution to a wing at high angles of attack significantly alters the stall angle of the wing-body combination [12]. Effectively, a fuselage-wing combination increases the wing-induced angle of attack at all spanwise stations. This increase is greatest at the wing root and exponentially decreased towards the wing tip [12]. Due to this, the geometrical stall angle of the wing-fuselage combination is decreased when compared to the wing alone. Therefore, the empirical correction factor introduced by Datcom has been used in the current thesis to correct the wing-only  $C_{L_{max}}$  for body effects. Datcom established a relation between the maximum lift coefficient of the isolated wing and the maximum lift coefficient of the wing-body combination by using an empirically derived correlation which can be seen in Equation 3.54.

$$(C_{L_{\max}})_{\text{wing+body}} = \left[ \frac{(C_{L_{\max}})_{\text{wing+body}}}{(C_{L_{\max}})} \right] (C_{L_{\max}}) \quad (3.54)$$

Herein,  $\left[ \frac{(C_{L_{\max}})_{\text{wing+body}}}{(C_{L_{\max}})} \right]$  is an empirically derived factor which depends on the wing taper, leading-edge sweep, and the ratio between the wing span and fuselage diameter. The experimentally derived data sets to determine the  $\left[ \frac{(C_{L_{\max}})_{\text{wing+body}}}{(C_{L_{\max}})} \right]$  ratio as can be seen in Figure 3.32a and Figure 3.32b



(a) Taper ratio correction factor for subsonic speeds



(b) Empirical derived wing-body maximum lift coefficient correction factor

Figure 3.32: Empirically derived data to correct the wing-only maximum lift coefficient for body effects [12]

Figure 3.32b, shows that this method is solely applicable to wings that have no anhedral or dihedral. A definition of both these terms is given in Figure 3.33. Also, the vertical position of the wing seems to be neglected. To give an example, a significant amount of anhedral can counteract the spanwise boundary layer flow on swept-back wings due to prevalent gravitational forces that pull the boundary layer towards the wing root. Hence, the applicability of this empirical method is limited and a critical attitude towards the implementation should be taken.

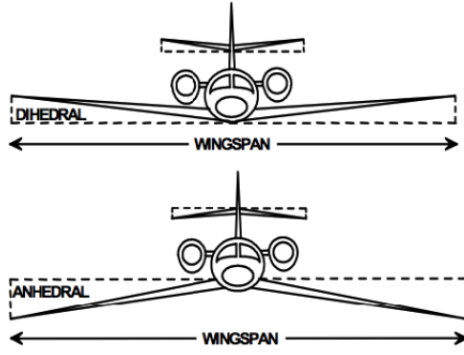


Figure 3.33: Scematic illustration of wing anhedral and wing dihedral

### 3.6. CONVERGENCE OPTIMIZATION

The methodology of approximating the maximum lift coefficient for both clean and high-lift wings has been laid out. Here, it became apparent that both the Critical Section Method, which is summarized in Figure 3.10, and the Pressure Difference Rule, which is summarized in Figure 3.16, require iterations to determine a wing's  $C_{L_{\max}}$ . One could choose to start the iteration at  $0^\circ$  angle of attack and subsequently increase the angle of attack in a stepwise manner until the stalling condition is reached. For the Critical Section Method, this happens when the span loading is locally equal to a wing section's  $c_{l_{\max}}$ . For the pressure difference rule, the same holds but the effective pressure difference,  $C_{p_{\text{eff}}}$ , and critical pressure difference,  $C_{p_{\text{crit}}}$ , are used to determine  $C_{L_{\max}}$ .

A more efficient method to find the critical conditions in both approaches is to implement one of the root-finding algorithms, which were discussed in Section 2.5. Here, it was chosen to utilize the Newton-Raphson approach as root-finding method because it yields a quadratic convergence rate compared to the linear convergence of the Bisection method.

To start, it is recognized that the Newton-Raphson root finding algorithm, as presented in Section 2.5, is solely applicable to one-dimensional data sets. However, the wing's span loading, effective pressure difference and critical pressure difference all depend on both the wing's angle of attack and the spanwise wing station  $\eta$ . Hence, the mentioned aerodynamic quantities are all two dimensional, and are thus not applicable to the Newton-Rahpson algorithm. Therefore, the Kreisselmeier-Steinhauser aggregation function, see Equation 3.55, is utilized to transform the two-dimensional data sets to a single dimension. This function is chosen since this aggregation function has shown to be useful [51–53] for predicting  $C_{L_{\max}}$  in optimization schemes.

In Equation 3.55 the Kreisselmeier-Steinhauser aggregation function is given. Here, setting  $\rho_{\text{ks}}$  equal to 80 showed remarkably good results [51] for finding the aggregate of for example the spanwise loading. The following will give an overview of the coupling of the KS-function and the Newton-Raphson root finding algorithm for the PDR implementation as presented in Figure 3.16.

$$\text{KS} = f_{\max} + \frac{1}{\rho_{\text{ks}}} \log_e \left( \sum_{k=1}^K e^{\rho_{\text{ks}}(f_k(X) - f_{\max})} \right) \quad (3.55)$$

- Initially, an initial angle of attack range is selected to find the critical conditions for both the CSM and PDR. Here, the initial angle of attack range should be large enough to encompass the stall angle of the wing, and small enough to enable a rapid convergence. Hence, a initial angle of attack range of  $0^\circ$  and  $30^\circ$  is selected for the developed  $C_{L_{\max}}$  prediction method.
- Then, the critical pressure difference and effective pressure distributions are computed at both the initial angles of attack. Subsequently, these distributions are transformed with the KS-function of Equation 3.55 by setting  $\rho_{\text{ks}} = 80$ . This yields the KS-values given in Equation 3.56 which are schematically presented in Figure 3.34.

$$\begin{aligned} & (KS_{\text{eff}})_{AOA=30^\circ} \quad (KS_{\text{eff}})_{AOA=0^\circ} \\ & (KS_{\text{crit}})_{AOA=30^\circ} \quad (KS_{\text{crit}})_{AOA=0^\circ} \end{aligned} \quad (3.56)$$

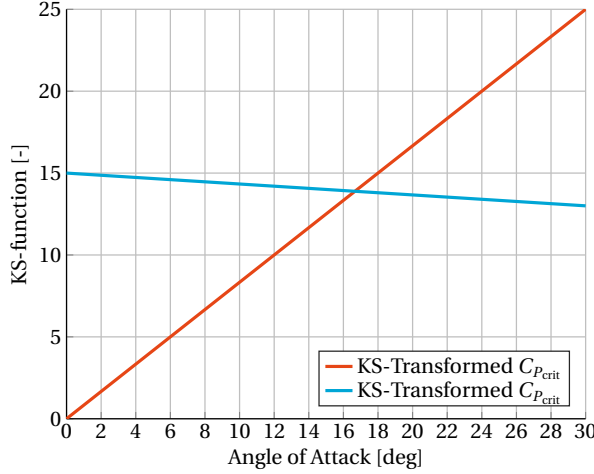


Figure 3.34: Initial range schematic of KS-values at  $\alpha = 0^\circ$  and  $\alpha = 30^\circ$  for the Newton-Raphson algorithm

- Now, one is interested in finding the wing's angle of attack where  $KS_{\text{crit}} = KS_{\text{eff}}$ . This would be rather simple if the values of  $KS_{\text{crit}}$  would be independent of angle of attack. However, this is not the case as the critical pressure difference depends on the effective Reynolds number, which again depends on the angle of attack due to the dependence on the induced angle of attack. Therefore, the Newton-Raphson root finding algorithm is used by determining the linear equation of the KS-transformed effective pressure difference (orange line in Figure 3.34) with the following:

$$y = m \alpha + C \quad (3.57)$$

$$m = \frac{(KS_{\text{eff}})_{AOA=30^\circ} - (KS_{\text{eff}})_{AOA=0^\circ}}{30^\circ - 0^\circ} \quad (3.58)$$

$$C = (KS_{\text{eff}})_{AOA=30^\circ} - m 30^\circ \quad (3.59)$$

- Then, the first iteration in the Newton-Raphson algorithm is performed to approximate the critical angle of attack where stall is bound to occur. This is done with the following:

$$KS_{\text{crit}} = m \alpha_1 + C \quad (3.60)$$

$$\alpha_1 = \frac{KS_{\text{crit}} - C}{m} \quad (3.61)$$

- Subsequently, the effective pressure difference distribution is determined at  $\alpha_1$ , this gives the value of  $C_{p_{\text{eff}}}(\alpha_1)$  at every spanwise station. Then, this value is transformed with the KS-function and a check is performed:

$$|(KS_{\text{crit}})_{\alpha_1} - (KS_{\text{eff}})_{\alpha_1}| < \epsilon_{\text{ks}} \quad (3.62)$$

- Here,  $\epsilon_{\text{ks}}$  is a user-specified convergence criteria, which is often around 1%. If the convergence criteria of Equation 3.62 holds, stall is reached. If not, subsequent iterations follow until convergence is reached. This procedure can effectively be summarized with the following:

$$\alpha_{n+1} = \alpha_n - \frac{KS_{\text{eff}}}{m} \quad (3.63)$$

Where the slope  $m$  is determined during every iteration step by using the angle of attack of every previous and consecutive iteration.

An example of this iteration scheme is presented in Figure 3.35. Here, the Newton-Raphson method is compared against the Bisection method. It can be seen that the Newton-Raphson converges in 6 iterations against the 9 iterations of the bisection method. This is a feature which was to be expected due to the difference in the discussed convergence rates. To quantify the computational expense, the 6 iterations of the Newton-Raphson method took 4.5 seconds to converge while the bisection method took 6.75 seconds to converge.

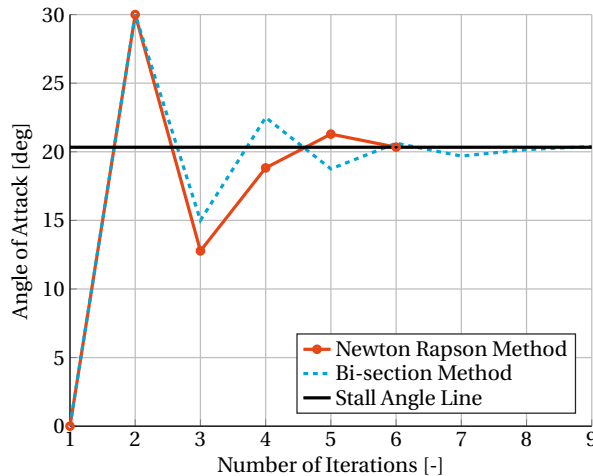


Figure 3.35: Comparison between the Newton-Raphson- and bisection convergence for a clean wing with 45° sweep back, aspect ratio 6, taper ratio 0.5 and a span of 11 m

Within the implementation of the Newton-Raphson method, it is assumed that the initial starting angles of attack are proper and that the derivatives of the implemented functions are calculable. Also, it is assumed that no overshoot occurs and that the derivative of the KS-functions are well behaved.

## 3.7. VERIFICATION & VALIDATION

Within this section, the various concepts which are presented in the methodology are verified for correctness. This enables one to judge whether the methods are applied correctly. Also, the fidelity of the individual components that make up the methodology as a whole is measured accordingly. Initially, the ESDU 84026 empirical method is validated. This is followed by a vortex-lattice grid convergence study. Finally, the implemented two-dimensional vortex-panel methods are verified.

### 3.7.1. ESDU 84026 $c_{l_{\max}}$ PREDICTION VALIDATION

The ESDU 84026 empirical method for the prediction of  $c_{l_{\max}}$  has been validated accordingly. Here, different families of the NACA airfoils are consulted. Table 3.1 displays the validation results for the NACA 4-digit series. For the validation, the extensive experimental work of Abbot & Doenhoff [32] has been consulted. From Table 3.1, it is evident that the maximal absolute error is achieved with the NACA 2410 airfoil. The reason for this is yet unknown but it is argued that the distribution of coordinate points at the leading edge might lack smoothness for this airfoil. Due to this, the leading-edge sharpness parameter,  $z_{u1.25}$  in Figure 3.1, utilized by the ESDU method might be approximated incorrectly, which translated to an inaccurate  $c_{l_{\max}}$  prediction.

The approximated and measured data for the NACA-24XX airfoil family for a variable airfoil thickness is displayed in Figure 3.36. Here, the measurements by Abbot and von Doenhoff show an initial increase of the maximum section lift coefficient with increasing airfoil thickness. The measured  $c_{l_{\max}}$  values subsequently decrease beyond an airfoil thickness of 12%. A similar trend is also obtained with the implementation of the

Table 3.1: Validation of the ESDU 84026  $c_{l_{\max}}$  prediction method for NACA 4-digit series at  $M = 0.38$  and  $Re = 9 \cdot 10^6$ . Experimental results obtained from Abbot & von Doenhoff [32]

Airfoil	Abbot & van Doenhoff $c_{l_{\max}}$	ESDU 84026 $c_{l_{\max}}$	Absolute error (%)
NACA 0006	0.92	0.95	3
NACA 0009	1.33	1.30	3
NACA 0012	1.53	1.63	7
NACA 1408	1.35	1.38	2
NACA 1410	1.52	1.5	2
NACA 1412	1.57	1.69	8
NACA 2408	1.5	1.54	3
NACA 2410	1.62	1.81	12
NACA 2412	1.69	1.75	4
NACA 2415	1.65	1.64	1
NACA 2418	1.47	1.59	8
NACA 2421	1.48	1.48	0
NACA 2424	1.3	1.41	8
NACA 4412	1.66	1.78	7
NACA 4415	1.63	1.74	7
NACA 4418	1.54	1.70	11
NACA 4421	1.47	1.57	7
NACA 4424	1.39	1.51	9

ESDU approximation. This implies that the empirical ESDU method is able to capture the effects of increasing airfoil thickness.

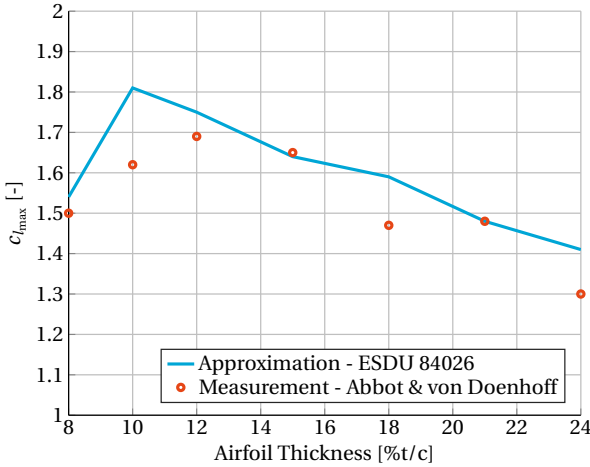


Figure 3.36: Validation of the ESDU 84026 method for the NACA24XX airfoil family

Table 3.2 displays a similar validation case. Here, the NACA 5-digit series are validated against the experimental results of Abbot & von Doenhoff [32]. It is evident that all the errors of the approximations are within 10%, which is generally acceptable during the conceptual aircraft design phase.

Finally, the work of Harris et al., [54] are consulted to validate the ESDU method for a supercritical airfoil. The results of this validation case is given in Table 3.3. Here, one can see that the ESDU method lacks fidelity in measuring the  $c_{l_{\max}}$  of a supercritical airfoil. This is peculiar since they developed a factor,  $F_S$ , to account for rear-loading effects on airfoil stall. In Section 2.3.5 it was shown that the maximum lift of an airfoil decreased with increasing compressibility effects. This trend is also seen in Table 3.3, the approximated ESDU results decrease with increasing Mach number. This implies that approximated  $c_{l_{\max}}$  might be erroneous, the compressibility effects are still captured by the ESDU method.

Table 3.2: Validation of the ESDU 84026  $c_{l_{\max}}$  prediction method for NACA 5-digit series at  $M = 0.38$  and  $Re = 9 \cdot 10^6$ . Experimental results obtained from Abbot & von Doenhoff [32]

Airfoil	Abbot & von Doenhoff $c_{l_{\max}}$	ESDU 84026 $c_{l_{\max}}$	Absolute error (%)
NACA 23012	1.78	1.7	5
NACA 23015	1.72	1.57	9
NACA 23018	1.6	1.52	5
NACA 23021	1.5	1.44	4
NACA 23024	1.42	1.32	7

Table 3.3: Validation of the ESDU 84026 method for the NASASC2-0714 airfoil at  $Re = 6 \cdot 10^6$ . Experimental results obtained from Harris et al[54]

Mach	0.1	0.2	0.3
Harris et al $c_{l_{\max}}$	2.17	2.14	1.78
ESDU 84026 $c_{l_{\max}}$	1.79	1.68	1.48

### 3.7.2. VORTEX-LATTICE GRID CONVERGENCE STUDY

AVL's panel density is another important aspect to take into account. A study on the effect of grid size on both the computational time and  $C_{L_{\max}}$  prediction has been performed. Several grid densities were selected and tested accordingly, as can be seen in Tables 3.4, 3.5 and 3.37 for a wing in clean and high lift configuration respectively.

From Table 3.4 and 3.5 it becomes evident that the time to converge increases exponentially with increasing panel density for both configurations. Also, the overall difference in  $C_{L_{\max}}$  is within 0.5 % for the clean wing and within 3 % for the high lift wing. Hence, a coarse grid density is sufficient for clean  $C_{L_{\max}}$  computations since it is both accurate and rapid. For the high-lift configuration, the  $C_{L_{\max}}$  computations change with increasing panel density. A simple cost-benefit analysis shows that it would be inefficient to use the fine grid density for high-lift configurations. A negligible difference of 0.041 in the  $C_{L_{\max}}$  approximation is obtained for the fine grid when compared to the coarse grid at an 2400% increase in computational time.

These results might not hold for other wing designs. Therefore the medium grid density is used for the clean  $C_{L_{\max}}$  computations because it is still fairly rapid. For the high-lift configurations, the medium coarse panel densities are chosen to retain rapidity.

Table 3.4: AVL grid convergence study - Clean wing

Grid type	Spanwise panels	Chordwise panels	Total panels	Clean $C_{L_{\max}}$	Run time [s]
Coarse	5	5	25	0.999	4.68
Medium coarse	10	6	60	0.995	4.81
Medium	20	10	200	0.996	4.94
Medium fine	30	20	600	0.994	12.98
Fine	38	25	950	0.995	36.11

Table 3.5: AVL grid convergence study - Full span flap deflection:  $\delta_f = 10^\circ$

Grid type	Spanwise panels	Chordwise panels	Total panels	High lift $C_{L_{\max}}$	Run time [s]
Coarse	5	5	25	1.434	8.54
Medium coarse	10	6	60	1.409	9.19
Medium	20	10	200	1.398	11.10
Medium fine	30	20	600	1.404	73.86
Fine	38	25	950	1.393	206.63

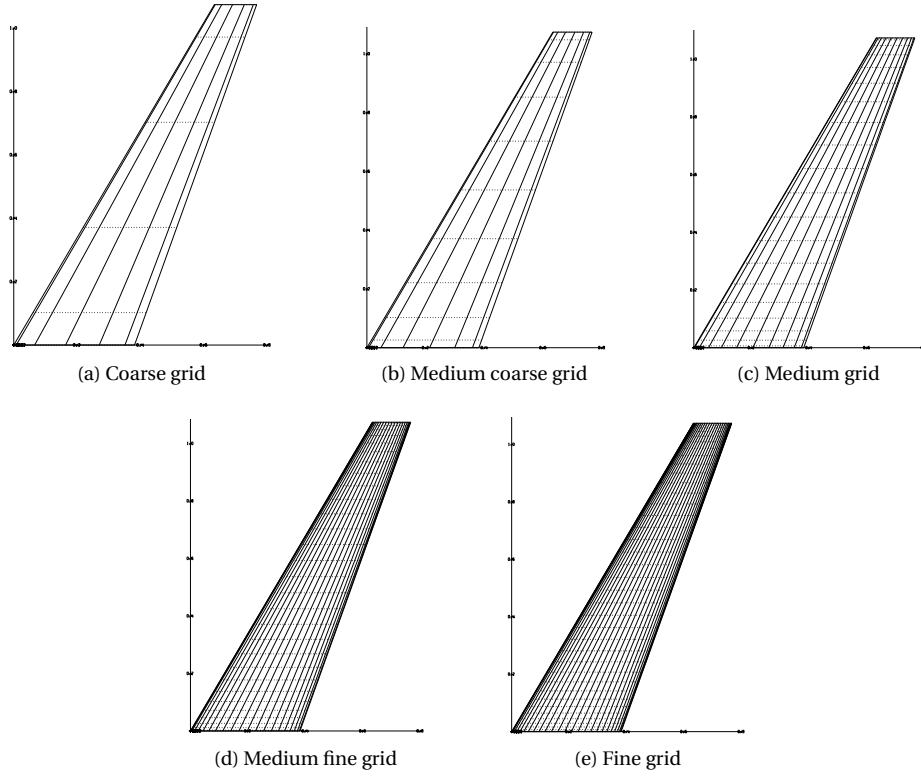


Figure 3.37: Vortex-lattice grid densities which are used in the convergence study of the clean wing

### 3.7.3. TWO-DIMENSIONAL VORTEX-PANEL METHOD VERIFICATION

The developed two-dimensional vortex-panel methods are verified to determine the fidelity of their implementation. Initially, the constant-strength vortex-panel method for single-element airfoils is discussed. Subsequently, the linear-strength vortex-panel method for high-lift airfoil configurations is verified. Figures 3.38 to 3.40 display the comparison of the computed pressure distributions with both the constant-strength vortex-panel method and Xfoil. Xfoil is an interactive linear-vortex panel-method program for the viscous/inviscid analysis of subsonic airfoils [45]. From Figures 3.38 to 3.40, it becomes evident that the constant-strength vortex-panel method is implemented correctly as the differences between the computed pressure distributions are close to nil.

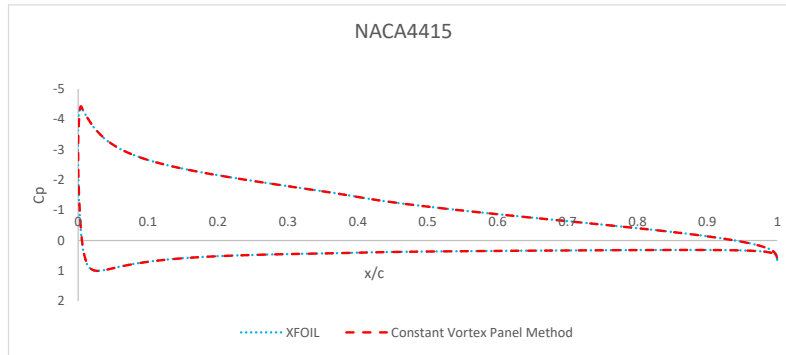


Figure 3.38: Pressure coefficient distribution over the NACA 4415 at  $\alpha = 10^\circ$  and  $M = 0$  - XFOIL vs constant strength-vortex panel method

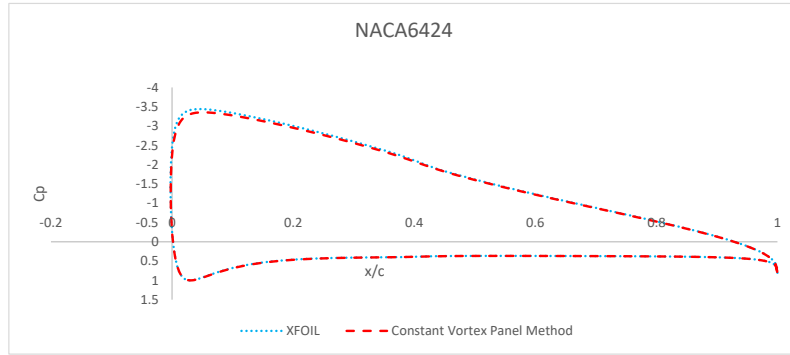


Figure 3.39: Inviscid pressure coefficient distribution over the NACA 6424 at  $\alpha = 10^\circ$  and  $M = 0$  - XFOIL vs constant strength-vortex panel method

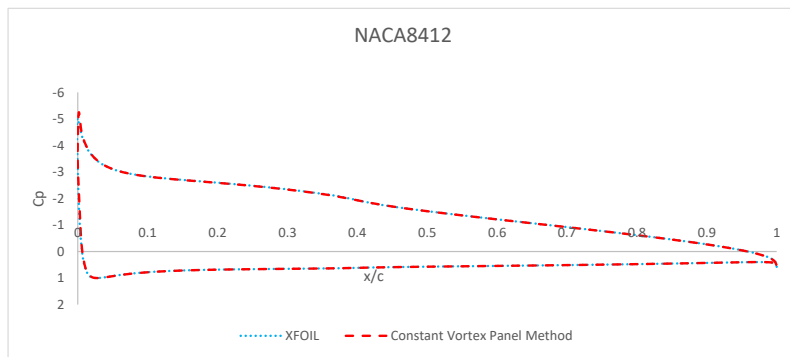


Figure 3.40: Inviscid pressure coefficient distribution over the NACA 8412 at  $\alpha = 10^\circ$  and  $M = 0$  - XFOIL vs constant strength-vortex panel method

Similarly, the computed results of the linear-strength vortex-panel method have been compared to results from MSES. MSES is a viscous/inviscid Euler method which is capable of analyzing multi-element airfoils at low Reynolds numbers. From Figure 3.41 it is evident that the linear-vortex panel method is in good agreement with MSES. However, the convex kink of the main element seems to generate a local suction peak at  $x/c = 0.7$ . This peak originates from a sudden reversal of local panel angles. Also, the trailing edge pressure coefficients on both main and flap elements seem to be locally under predicted. This possibly originates from inadequate paneling at the trailing edges.

It has been shown that the result of the linear-strength vortex-panel method is in good agreement with MSES. This does not directly imply that the linear-strength vortex-panel method yields an accurate high-lift pressure distribution prediction. However, it demonstrates that the linear-vortex panel method is on par with the fidelity of a higher-order Euler solver.

Also, a plain flap has been modeled with the linear-strength vortex-panel method. The resulting pressure distribution is illustrated in Figure 3.42. Herein, the generated pressure distribution is again compared against Xfoil. The comparison shows that the constructed panel method is in agreement with the results of Xfoil. However, Xfoil generates a higher suction peak at the leading edge and hinge point. The reasoning behind this is unclear since Xfoil is a software which is also based on a linear-strength vortex method. Perhaps the airfoil that is loaded within Xfoil is internally redesigned before it is analyzed by Xfoil's potential flow solver.

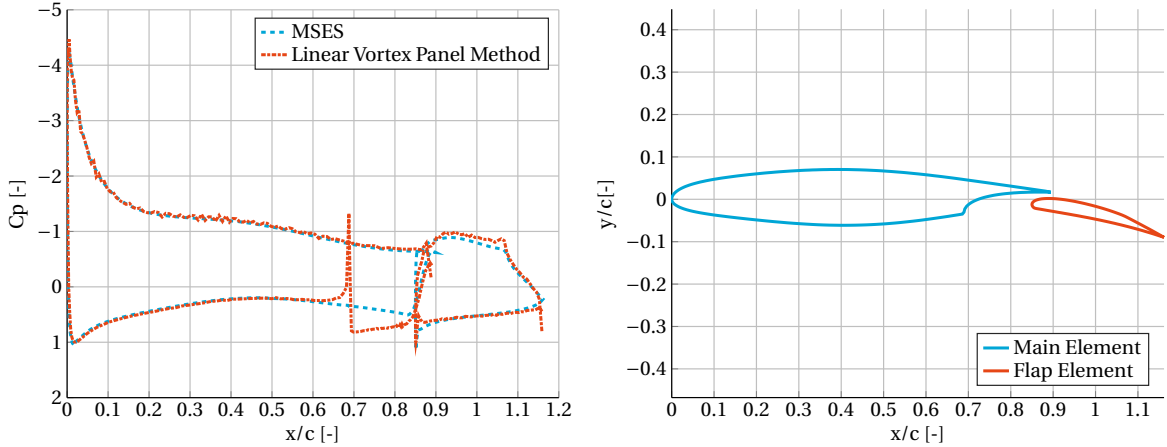


Figure 3.41: Pressure coefficient distribution over a multi-element airfoil at  $\alpha = 2^\circ$  and  $M = 0$  - MSES vs linear-vortex panel method

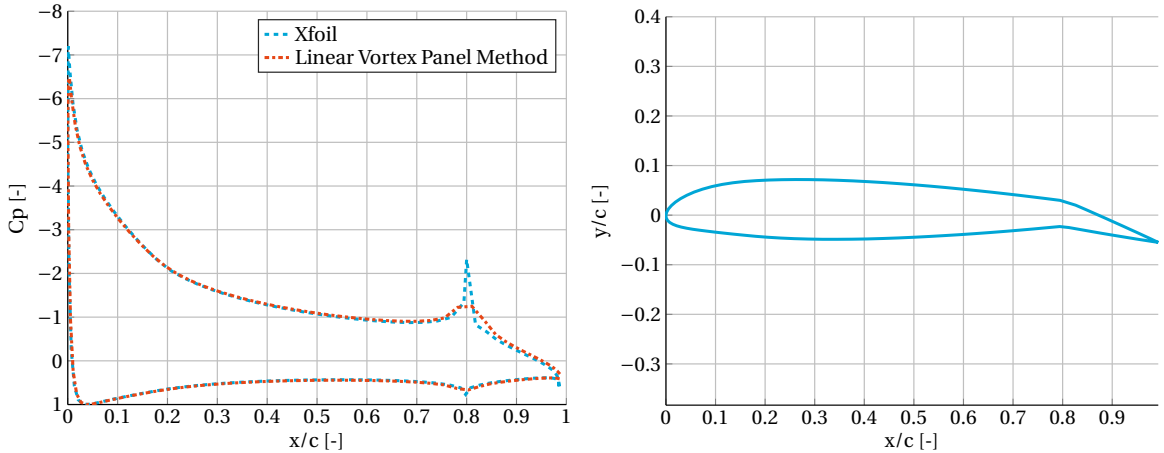


Figure 3.42: Inviscid pressure coefficient distribution over the NACA 23012 with a plain flap at  $\alpha = 8^\circ$ ,  $\delta_f = 15^\circ$  and  $M = 0$  - XFOIL vs linear-vortex panel method

### 3.7.4. $C_{L_{\text{MAX}}}$ PREDICTION METHOD VERIFICATION

The estimation of the clean  $C_{L_{\text{MAX}}}$  with both the Critical Section Method and Pressure Difference Rule, as implemented within this thesis, have been verified. Here, both methods are tested with a wing with a variable amount of leading-edge sweep. This enables one to expose the contrast, if it exists, between the two methods and their respective behavior with increasing sweep angles. The results of this verification are given in Figure 3.43 and the utilized wing and airfoil geometry are presented in Figure 3.6 and Figure 3.44 respectively. From the results, it can be seen that the computed maximum lift coefficient is decreasing with increasing sweep angle for both methods. This behavior is also commonly found during wind tunnel testing [55]. The decrease of  $C_{L_{\text{MAX}}}$  with sweep angle is more gradual for the PDR as compared to the rapid decrease of the CSM implementation. This is a result of the inaccurate simple-sweep theory implementation within the CSM method to correct the local wing section's  $c_{l_{\text{MAX}}}$  for sweep effects. The empirical data used within the PDR seemingly captures the spanwise boundary layer flow and the resulting retardation of boundary layer separation because the decrease in  $C_{L_{\text{MAX}}}$  is not vivid.

The main problem exposed with this validation case is that both methods do not yield the exact same results at the given sweep angles. Therefore, building a  $C_{L_{\text{MAX}}}$  prediction tool with these two methods is rather difficult. The reason behind this lies in the design scheme of the Initiator. Here, multiple iterations are performed within the Initiator to determine a preliminary aircraft design. During these iterations, it is probable that the sweep angle of the scrutinized wing changes. Therefore, implementing both the CSM and PDR within the

tool, where the selection of the method is based on the wing sweep, yields different results at a sweep junction point.

For example, say the CSM would be used for wings that have less than  $10^\circ$  quarter-chord sweep, and the PDR for wings with more than  $10^\circ$  quarter-chord sweep. Then, if the wing sweep would slightly change from  $9^\circ$  to  $11^\circ$  during the convergence loop of the Initiator, a change of implemented maximum lift coefficient prediction method would occur. As can be seen in Figure 3.43, large differences between the  $C_{L_{\max}}$  prediction of the consecutive iterations would result. This might cause a divergence of the desired aircraft design which is determined by the user of the Initiator.

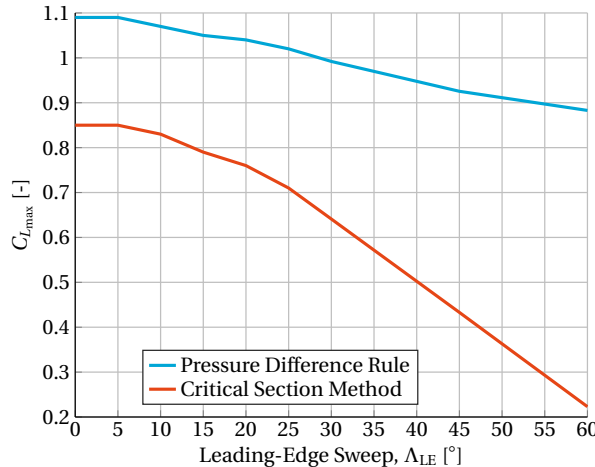


Figure 3.43: Computed  $C_{L_{\max}}$  results by the CSM and PDR for various leading-edge sweep angles at  $M = 0.22$  and  $Re_\infty = 0.96 \cdot 10^6$  for the wing geometry given in Table 3.6

Table 3.6: Geometrical properties of the verified wing [56]

Parameter	Value	Unit
Surface Area	0.5523	[m <sup>2</sup> ]
Aspect Ratio	8.51	[ - ]
Taper Ratio	0.35	[ - ]
Leading-edge sweep	variable	[deg]
Root chord	0.381	[m]
Wing span	2.148	[m]
Root/tip airfoil	Fig 3.44	[ - ]
Mean aerodynamic chord	0.2572	[m]

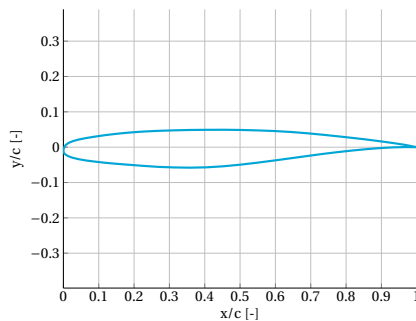


Figure 3.44



# 4

## TEST CASES

The chapter at hand presents  $C_{L_{\max}}$  test cases where both the Critical Section Method and Pressure Difference Rule are validated against windtunnel measurements. Initially, measurements conducted on the straight wing of the Fokker F27 are used to determine the fidelity of both methods in predicting the  $C_{L_{\max}}$  of a straight wing in Section 4.1. Then, two  $45^\circ$  swept-back wings, one without washout and the other with  $10^\circ$  tip washout are validated in Section 4.2. Subsequently, measurements on two swept-back wings with a full span Fowler flap are utilized to determine high-lift  $C_{L_{\max}}$  predictability in Section 4.3. Finally, the results are discussed in Section 4.4.

### 4.1. STRAIGHT WING

Research by Spigt and de Gelder [57] and Spoon [58] has been consulted for the straight wing validation. Herein, the researchers conducted a series of windtunnel measurements on a 1:20 scale model of the Fokker F27 "Friendship" in the low speed windtunnel of the Technical University of Delft. Spoon found that the clean  $C_{L_{\max}}$  of this wing, after correcting for the windtunnel wall effects, suspension systems and instrumental deficiencies, was 1.02 at an angle of attack of  $10.5^\circ$ . Also, total wing stall originated at the trailing-edge of the wing's center as can be seen in Figure 4.2. To conduct the validation, the wing's geometrical properties are obtained from [58], see Table 4.1 and Figure 4.1 and windtunnel settings are gathered from [57]. Also, the tests were conducted at  $Re = 7 \cdot 10^6$ , which was computed with a reference chord of 1.

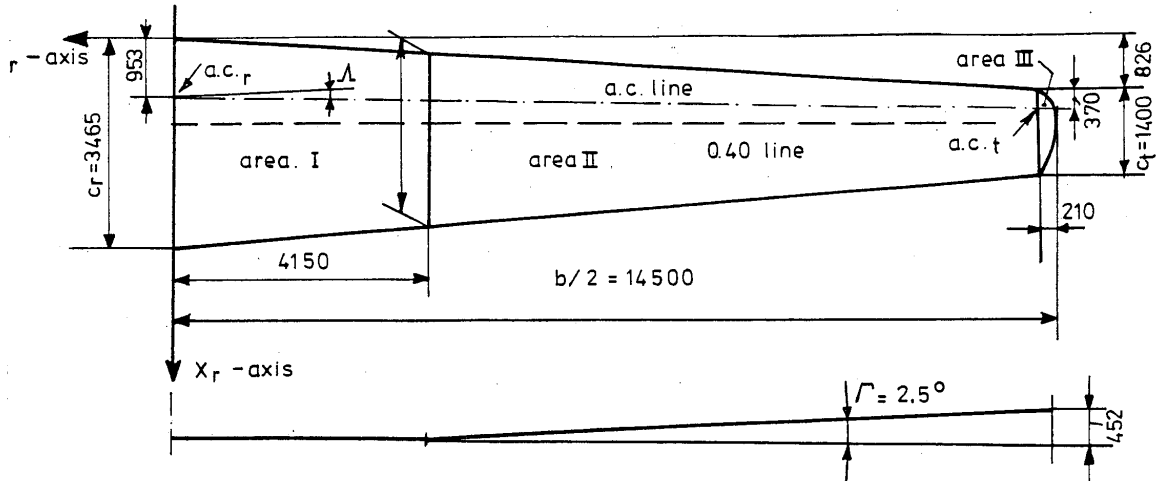


Figure 4.1: The planform of the Fokker F27 wing as tested by Spigt and de Gelder [57]

Utilizing both the Pressure Difference Rule and the Critical Section Method yields the results which are depicted in Figure 4.3 and Table 4.2. Herein, it is evident that the span loading and  $c_{l_{\max}}$  distribution are locally

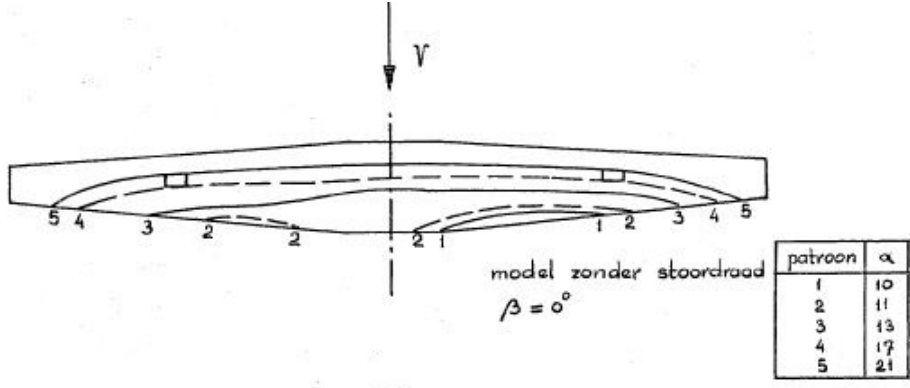


Figure 4.2: Stalling pattern on the Fokker F27 wing [57]

Table 4.1: Fokker F27 "Friendship" geometrical properties [58]

Parameter	Value	Unit
Surface Area	70	[m <sup>2</sup> ]
Aspect Ratio	12	[−]
Taper Ratio	0.42	[−]
Quarter Chord Sweep	1.19	[deg]
Tip Washout	-2.5	[deg]
Root Airfoil	NACA 642421	[−]
Tip Airfoil	NACA 642415	[−]

equal at the wing center. Also, the measured and predicted lift polars seem to be in a good agreement when the Critical Section Method is utilized. However, a large over estimation of the  $C_{L_{\max}}$  results when the Pressure Difference Rule is used.

The predicted lift polar seems to have a higher lift at zero angle of attack while having a slightly lower lift curve slope. The combination of these contrasts yields two overlapping lift curves. The dashed lift polar shows a kink at wing stall, since the post stall lift polar is omitted within the current analysis. Table 4.2 summarizes the validation results. The CSM estimation of  $C_{L_{\max}}$  is in good agreement with the measurements. The stall angle and local  $c_{l_{\max}}$  are slightly underpredicted. The found deviations stem from the non-viscous theoretical approach, e.g. omitting stall effects in the predicted lift polar. The local  $c_{l_{\max}}$  predicted by the ESDU method seems to be accurate for the used airfoils, since the percentual difference is less than 1%.

The results as per the Pressure Difference Rule are given in Table 4.3. Here, it clearly shows not that the  $C_{L_{\max}}$  estimation is heavily over predicted. The reason for this unacceptable estimation is discussed in the results and discussion Section 4.4.

Table 4.2: Comparison between the results found by Spoon [58], at  $M = 0.27$  and  $Re = 7 \cdot 10^6$ , and the estimated values with the Critical Section Method for the wing depicted in Figure 4.1

Parameter	Measured value	Estimated value	Unit	% error
$C_{L_{\max}}$	1.02	1.05	[−]	+3
$(c_{l_{\max}})_{\text{root}}$	1.13	1.12	[−]	-1
$(c_{l_{\max}})_{\text{tip}}$	1.11	1.10	[−]	-
$(\delta C_L / \delta \alpha)_{\text{linear}}$	0.1	0.087	[rad]	-13
$\alpha_{\text{stall}}$	10.5	9.94	[°]	-5

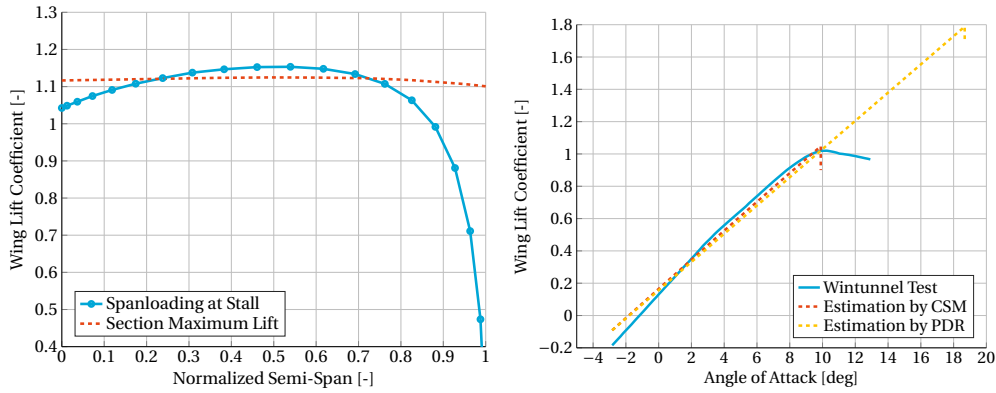


Figure 4.3: Lift polar comparison between the clean Fokker F27 results [57, 58], at  $M = 0.27$  and  $Re = 7 \cdot 10^6$ , and the estimated lift polars as per the CSM and PDR methods & critical span loading

Table 4.3: Comparison between the results found by Spoon [58], at  $M = 0.27$  and  $Re = 7 \cdot 10^6$ , and the estimated values with the Pressure Difference Rule for the wing depicted in Figure 4.1

Parameter	Measured value	Estimated value	Unit	% error
$C_{L_{\max}}$	1.02	1.78	[−]	+174
$(\delta C_L / \delta \alpha)_{\text{linear}}$	0.1	0.087	[rad]	-13
$\alpha_{\text{stall}}$	10.5	18.7	[°]	+178

## 4.2. SWEPT WINGS

For the swept wings, the validation procedure is divided into clean configurations and high lift configurations separately. Initially, two  $45^\circ$  swept wings in clean configuration are tested. This is proceeded by validating two wings with trailing-edge Fowler flaps.

### 4.2.1. SWEPT UNTWISTED WING

To validate the PDR, the work of Hunton [59, 60] has been used. Herein, a study of the span effects on aerodynamic wing properties of two swept-back wings at low speed, attached to a fuselage, has been conducted. The geometrical properties of the first wing configuration can be found in Table 4.4 and Figure 4.4. Figures. 4.6 and 4.5 yield the results of the implemented PDR coupled with the induced angle of attack calculation. Firstly, Figure 4.5 displays the calculated induced and effective angle of attack at wing stall. The induced angle of attack distribution seems plausible. I.e. a high induced angle of attack at the wing tip which is often seen on 3D lifting surfaces due to tip vortices. The effective angle of attack distribution is a logic derivative of the induced angle of attack when Equation 3.39 is used.

Table 4.4: Geometrical properties of the swept-back wing as tested by Hunton [59, 60]

Parameter	Value	Unit
Surface Area	11	[m <sup>2</sup> ]
Aspect Ratio	6	[−]
Taper Ratio	0.42	[−]
Quarter Chord Sweep	45	[deg]
Root Airfoil	NACA 64A010	[−]
Tip Airfoil	NACA 64A010	[−]
Fuselage Diameter	0.762	[m]

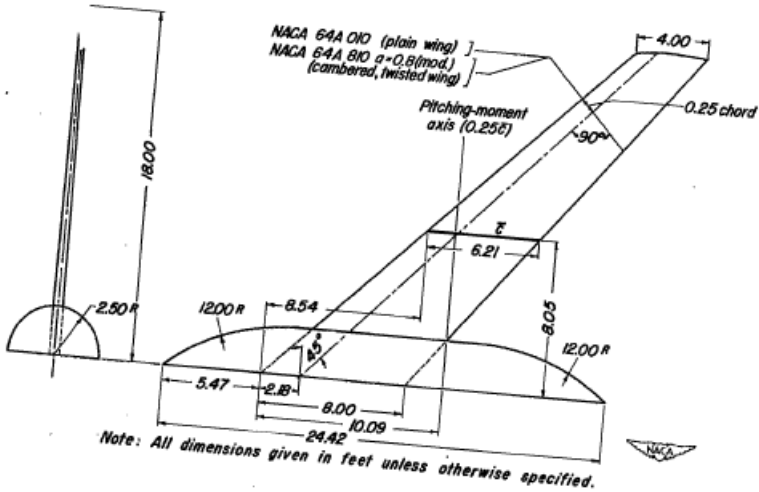


Figure 4.4: The planform of Hunton's analyzed wing+fuselage combination [59, 60]

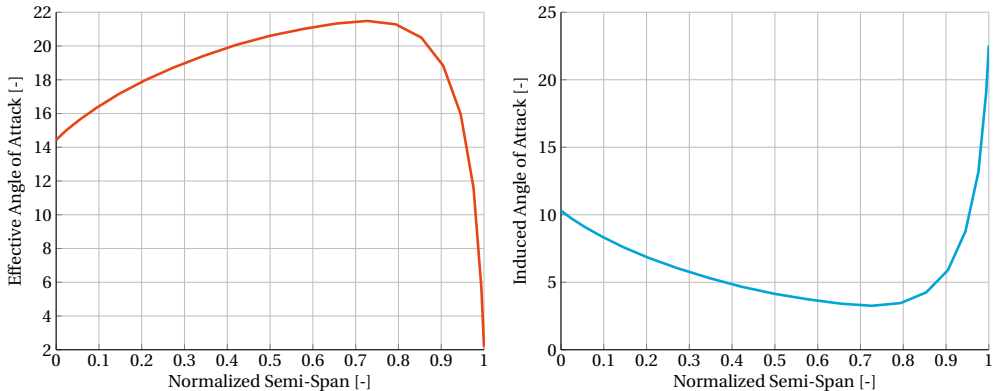


Figure 4.5: Effective and induced angle of attack distribution perpendicular to the wing at stall for the clean wing given in Table 4.4

Secondly, Figure 4.6 indicates the pressure difference at critical conditions and the associated lift polars. The pressure difference distribution shape is in agreement with the work of Valerzo & Chin [37]. The lift polars clearly show a good correlation with the measured lift polar in the linear range. However, at stall the approximation obviously differs from the measurements as the prevalent viscous flow is omitted. Also, the stall angle is significantly under predicted, see Table 4.5.

The stall angle of attack underprediction is caused by a concert of viscous phenomena. To start, lateral boundary layer flow acts as a boundary layer control agent at high lift values. This viscous phenomenon alleviates flow separation on the wing and therefore increases the stall angle. Secondly, from [60] it is evident that the inviscid span loading is over predicted when stall is imminent. Due to this, the effective angle of attack distribution is over predicted and therefore stall is reached at a lower wing angle of attack.

Proceeding, the difference between predicted and measured  $C_{L_{max}}$  is small due to the under prediction in stall angle. From Table 4.5, it is evident that the percentage difference is 5%.

This swept wing has also been tested with the CSM accordingly. The computed results can be found in Figure 4.7 and Figure 4.8. From Figure 4.7, it is evident that a boundary layer flow control is present on this 45° swept-back wing because the inboard  $c_l$  is rather high and rapidly declines towards the wing tip. This feature

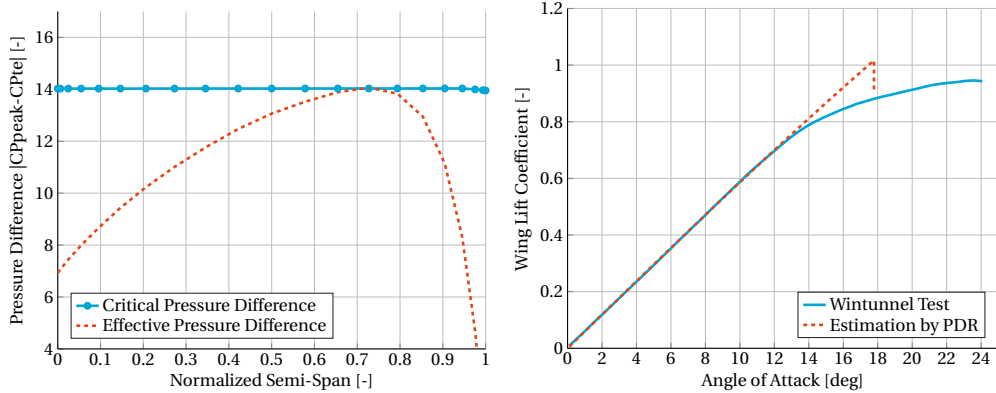


Figure 4.6: Lift polar comparison between the results of Hunton [59, 60], at  $M = 0.2$  and  $Re = 8 \cdot 10^6$ , and the estimated lift polar as per the PDR for the wing geometry given in Table 4.4 & section pressure distribution

Table 4.5: Comparison between the results found by Hunton [59, 60] at,  $M = 0.2$  and  $Re = 8 \cdot 10^6$ , and the estimated values with the Pressure Difference Rule for the wing geometry given in Table 4.4

Parameter	Measured value	estimated value	Unit	% error
$(C_{L_{max}})_{\text{wing}}$	–	1.0	[–]	–
$(C_{L_{max}})_{\text{wing+fuselage}}$	0.95	1.0	[–]	+5
$(\delta C_L / \delta \alpha)_{\text{linear}}$	0.06	0.06	[/ $^{\circ}$ ]	0
$\alpha_{\text{stall}}$	23	17.78	[ $^{\circ}$ ]	-29

is not captured by the ESDU 84026 method, which is implemented in the CSM scheme. Due to this, the  $C_{L_{max}}$  is strongly underpredicted by the CSM as can be seen in 4.8.

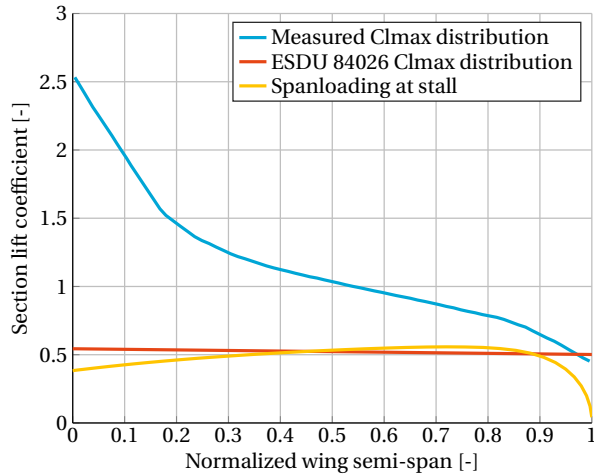


Figure 4.7: Section  $c_{l_{max}}$  distribution comparison between the measurements of Hunton [59, 60], at  $M = 0.2$  and  $Re = 8 \cdot 10^6$ , and the estimated  $c_{l_{max}}$  distribution as per the ESDU 84026 method for the wing geometry given in Table 4.4

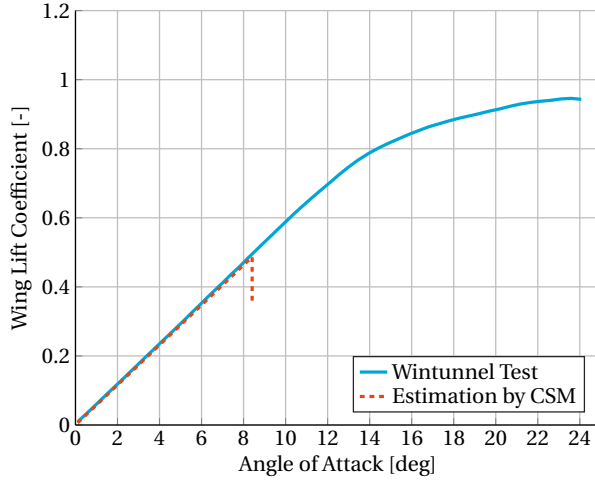


Figure 4.8: Lift polar comparison between the results of Hunton [59, 60], at  $M = 0.2$  and  $Re = 8 \cdot 10^6$ , and the estimated lift polar as per the CSM for the wing geometry given in Table 4.4

#### 4.2.2. SWEPT TWISTED WING

The following swept wing is similar to the initial swept wing but differs by a 10 degrees tip washout and the implementation of the cambered NACA 64A810 airfoil. Figure 4.9 displays the generated results. Herein, it is evident that the point of stall is moved inboard with the addition of wing washout. Figure 4.9 also displays the measured and predicted lift polars. It is evident that AVL's inviscid prediction coalesces with the measured lift polar in the linear lift range. However, the stall angle is under predicted.

This under prediction in stall angle is a product of flow separation suppression by lateral boundary flow solely. The implemented NACA 64A810 airfoil stalls from turbulent trailing-edge separation [60]. However, the lateral boundary layer flow completely suppressed the trailing-edge separation until the onset of leading-edge stall [60]. This stall suppression feature is absent in both the panel method and the stalling criterion set up by Valerzo & Chin [37].

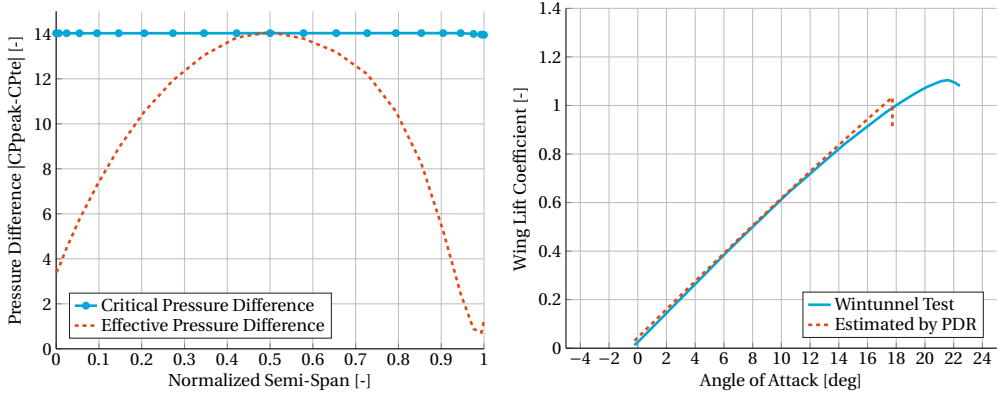


Figure 4.9: Lift polar comparison between the results of Hunton [59, 60], at  $M = 0.2$  and  $Re = 8 \cdot 10^6$ , and the estimated lift polar as per the PDR for the twisted wing geometry given in Figure 4.4 & section pressure distribution

The final results of the swept and twisted wing are summarized in Table 4.6. Herein, it is evident that the lift curve slope is well modeled. The mentioned discrepancy of the stall angle caused a  $C_{L_{max}}$  under prediction of 5 %. Care should be taken when the erroneous stall angle is utilized for other means.

Table 4.6: Comparison between the results found by Hunton [59, 60] and the estimated values, at  $M = 0.2$  and  $Re = 8 \cdot 10^6$ , for the twisted wing geometry given in Figure 4.4

Parameter	Measured value	Estimated value	Unit	% error
$(C_{L_{\max}})_{\text{wing}}$	—	1.04	[—]	—
$(C_{L_{\max}})_{\text{wing+fuselage}}$	1.1	1.04	[—]	-5
$(\delta C_L / \delta \alpha)_{\text{linear}}$	0.079	0.079	[rad]	0
$\alpha_{\text{stall}}$	21.5	17.73	[°]	-18

### 4.3. SWEPT HIGH-LIFT WINGS

The work of Lovell [56] has been consulted to validate a wing in high-lift setting. Lovell conducted wind tunnel experiments on two RAE wings which both had a variable span Fowler flap, with and without an attached fuselage. The main geometrical wing properties of the tested wing are given in Table 4.7 alongside the used airfoil geometry in high-lift setting in Figure 4.10. The mentioned validation model is tested against several nominal flap angles, namely 0, 10, 25 and 40 degrees.

Table 4.7: Geometrical properties of the RAE wing as tested by Lovell [56]

Parameter	Value	Unit
Surface Area	0.5523	[m <sup>2</sup> ]
Aspect Ratio	8.51	[—]
Taper Ratio	0.35	[—]
Quarter Chord Sweep	28	[deg]
Deflection Angles	0, 10, 25, 40	[deg]
Flap Chord	0.34c	[%]
Fuselage Diameter	0.3048	[m]

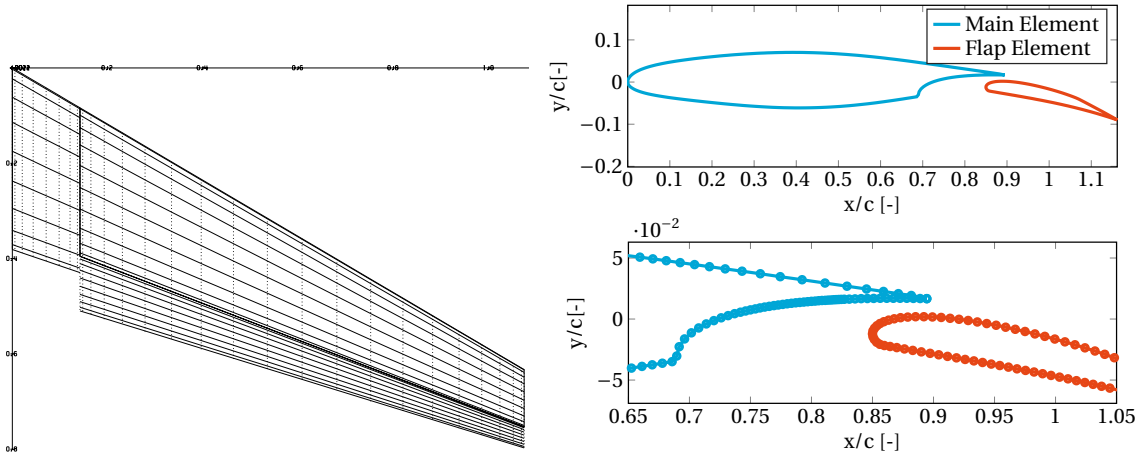


Figure 4.10: Airfoil and wing geometry in high lift setting generated by the high-lift AVL routine for the geometrical properties that are presented in Table 4.7

Also, the flap reduction models given in Figure 3.27 are simultaneously tested along side this wing model. It was found that the flap angle reduction model by Murillo & McMasters yielded the most accurate  $C_{L_{\max}}$  prediction when compared against wing only windtunnel data in Figure 4.11. Obert's model, although mostly similar to Murillo and McMaster's model, under predicted  $C_{L_{\max}}$  at a flap deflection of 40°. This was caused by the under prediction of the inviscid lift polar. Implementation of Valerzo & Chin's flap reduction model yielded good results at small flap deflections. However, a significant over prediction of  $C_{L_{\max}}$  is obtained at high nominal flap angles due to the flap being over deflected.

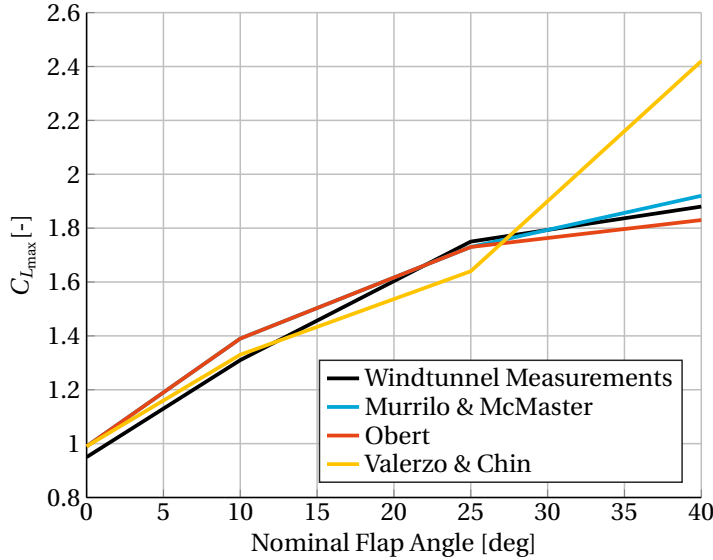


Figure 4.11: Computed  $C_{L_{\max}}$  by the high-lift PDR implementation, at  $M = 0.223$  and  $Re = 1.27 \cdot 10^6$ , for several flap angles and the comparison between flap angle reduction models of Figure 3.27

Figure 4.12 (left) illustrates the predicted  $C_{L_{\max}}$  for the tested flap deflections for the wing only model while implementing Murillo & McMasters's flap reduction curve. It is evident that an overall good approximation of  $C_{L_{\max}}$  is achieved. The largest error percentage of 8% was found at a nominal flap angle of 10 degrees.

Figure 4.12 (right) depicts the associated experimental and estimated lift curves for every nominal flap angle under scrutiny. From this Figure, it is clear that the proposed multi-element vortex lattice model in conjunction with Torenbeek's multi-element lift curve slope approximation works properly. All the estimated inviscid lift curves coalesce, to a certain degree, to the linear part of the experimental lift polars. An exception to this is found at a combination of relative high flap deflection of 40 degrees and a large wing angle of attack. This large discrepancy is caused by the inability to approximate the complex viscous decambering and boundary layer separation on the flap during these conditions.

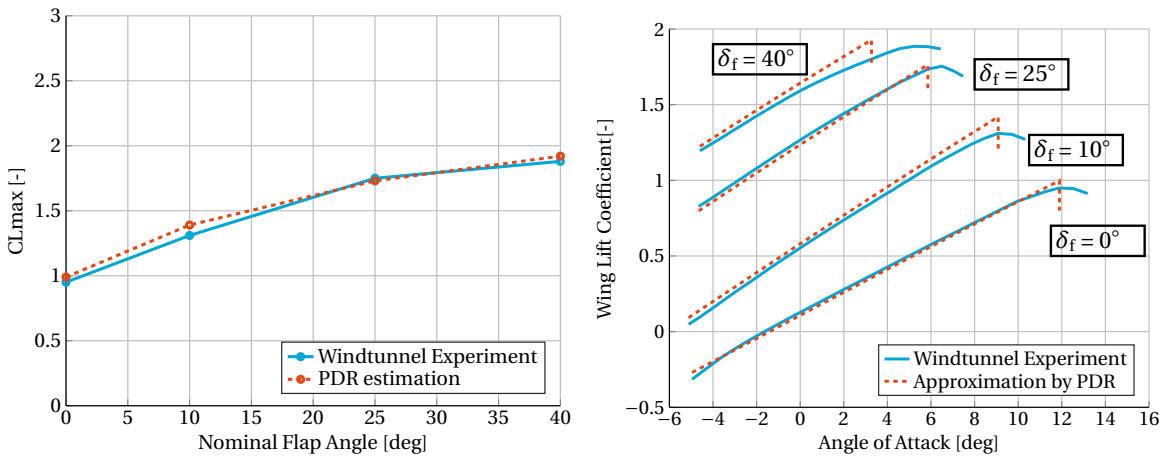


Figure 4.12: Comparison between estimated and measured [56]  $C_{L_{\max}}$ , at  $M = 0.223$  and  $Re = 1.27 \cdot 10^6$ , for the wing only model

The clean wing stall angle of Figure 4.12 is compared to the two swept wings in clean condition, Figure 4.6 and Figure 4.9, which were discussed prior to this section. The stall angle estimation is much more in agreement with measurements for this  $28^\circ$  swept back wing when compared to the estimated stall angles of the two wings of Figure 4.6 and Figure 4.9. This contrast depicts the difference in the magnitude of stall suppression

on wings having different sweep-back angles. Apparently, the stall angle of attack is estimated incorrectly for highly-swept wings. Therefore, the degree to which the stall angle can be estimated accurately depends on wing sweep.

Figure 4.13 displays the results for the wing-fuselage model. The obtained results are in good agreement with the experimental data on tested wing-fuselage model and similar behavior to the wing only model is observed. Hence, it can be concluded that the combination of the PDR and Datcom's fuselage correction yields adequate  $C_{L_{\max}}$  predictions.

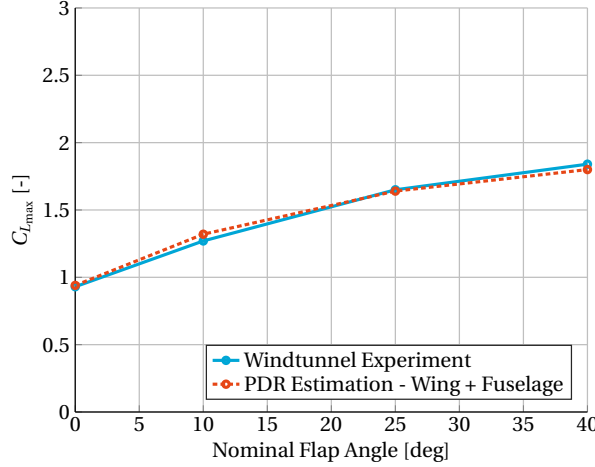


Figure 4.13: Comparison between estimated and measured [56]  $C_{L_{\max}}$ , at  $M = 0.223$  and  $Re = 1.27 \cdot 10^6$ , for the wing fuselage combination

Similarly, RAE's kinked swept wing with a single-slotted Fowler flap and fuselage combination has been validated. The results and wing geometry are depicted in Figure 4.14. Again, it is evident that the approximation is in good agreement with the measurements. However, the error at  $\delta_f = 10^\circ$  equals  $+11\%$ . This can be considered a rough over estimation since it can have a significant impact on further conceptual aircraft design practices.

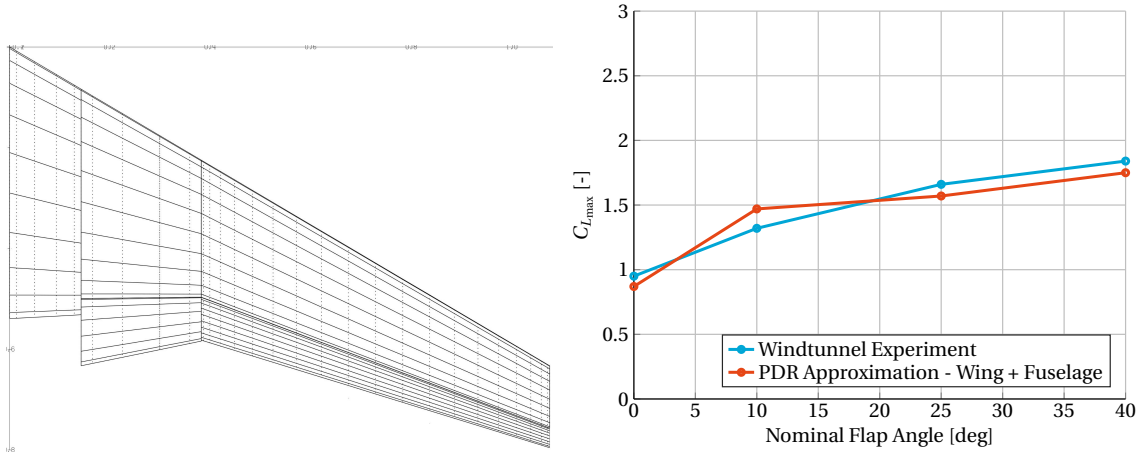


Figure 4.14: Comparison between estimated and measured [56] wing + fuselage  $C_{L_{\max}}$  at various flap angles for RAE's kinked wing,  $S = 0.55 m^2$ ,  $AR = 8.5$ ,  $\lambda = 0.35$ ,  $\Lambda_{c/4} = 28$ ,  $M = 0.2$

## 4.4. RESULTS AND DISCUSSION

From the test cases, several conclusions can be drawn. First, Murillo & McMasters's flap angle reduction model yielded both the best prediction of inviscid lift polar and  $C_{L_{\max}}$  when compared to windtunnel measurements of Lovell [56]. Although, Ober's approach is rather similar, it is based solely on the experimental

data of the Fokker 100. Therefore, Obert's flap reduction curve can be labeled devious.

The maximum lift coefficient can be predicted with reasonable accuracy, less than 11% error, for both the clean wing configuration and high-lift configurations. When one scrutinizes the Critical Section Method, it becomes evident that this method is suitable for straight wing configurations as the prediction error was rather small in Table 4.2. However, using the Critical Section Method for swept wings is disastrous since the  $C_{L_{max}}$  is highly under predicted due to the negligence of the spanwise flow effects as can be seen in Figure 4.7.

The Pressure Difference Rule on the other hand showed to be remarkably accurate for swept wings. The reason why this method works for swept wings lies in the implementation of the method. In the current thesis, a two-dimensional streamwise pressure distribution is computed with a vortex-panel method at several wing stations. Subsequently, these spanwise pressure distributions are transformed to be perpendicular to the quarter chord of a swept wing by using the simple-sweep theory. Harper and Maki [29] showed that the simple-sweep theory correction is a reasonable first estimate for the three-dimensional effects on the streamwise pressure distributions. This fact is depicted in Figure 4.15. Also Valerzo and Chin [37] argue that a wing will experience a pressure relief effect, which causes an actual wing to have a more positive suction peak at a given wing angle of attack when compared to a two-dimensional airfoil. However, at high angles of attack, it is expected that the two-dimensional and three-dimensional suction peaks are identical.

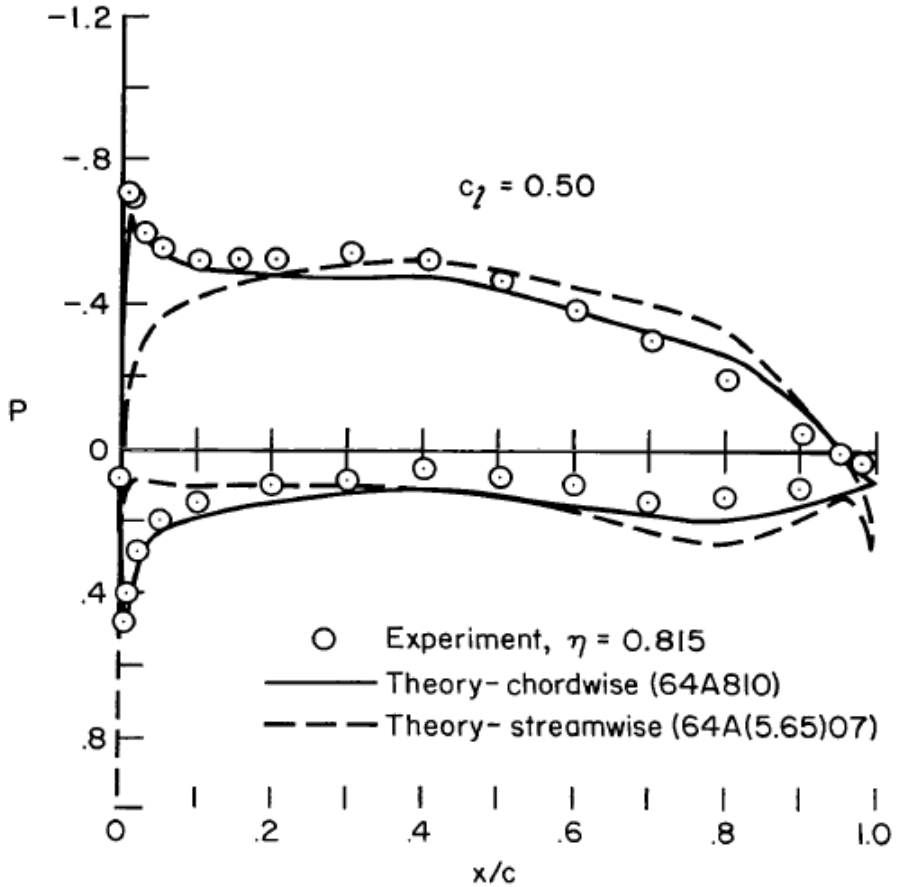


Figure 4.15: Section pressure distribution comparison between chordwise, streamwise and measured local pressure distributions on a  $45^\circ$  swept-back wing [29]

However, the Pressure Difference Rule was unable to accurately estimate the maximum lift coefficient of the straight Fokker F27 wing. The reason behind this was uncovered during an interview with the researcher that developed the Pressure Difference Rule (Valerzo, W.O. (2016, December 23). Email interview). Here, it was revealed that the Pressure Difference rule solely holds for wings that stall from the leading edge. This is often the case for swept-back wings as they implement thin airfoils to operate in transonic conditions. The

Fokker F27 is a low-speed propeller powered aircraft which incorporates airfoils which are efficient in low-speed and stall from the trailing edge as can be seen in Figure 4.2. Due to this, the empirically based Pressure Difference Rule does not include the means to cope with the trailing-edge stall of any straight wing. On behalf of this, Valerzo delivered unpublished data. Here, his preliminary, and unfinished, findings on airfoils which stall from the trailing edge showed that the maximum critical pressure difference peaked at 10 instead of the original 14 as can be seen in Figure 4.16. He labeled this method as the Modified Pressure Difference Rule (MPDR). Hence, the MPDR have been utilized again with the Fokker F27 as can be seen in Figure 4.17. Again, the MPDR lacks fidelity in predicting the maximum lift coefficient. Hence, it is recommended that this method is developed further by additional windtunnel experiments on airfoils which stall from the trailing edge.

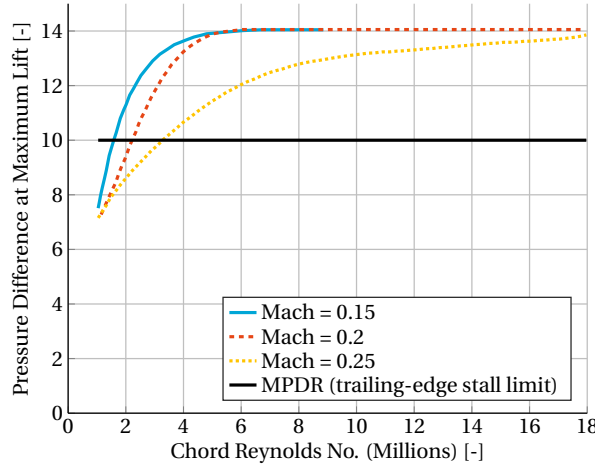


Figure 4.16: The Modified Pressure Difference Rule for trailing-edge stall airfoils

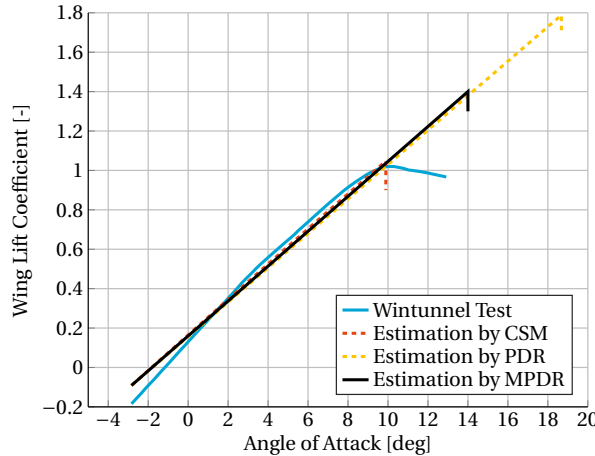


Figure 4.17: Lift polar comparison between the clean Fokker F27 results [57, 58], at  $M = 0.27$  and  $Re = 7 \cdot 10^6$ , and the estimated lift polars as per the CSM, PDR, and the MPDR for the wing depicted in Figure 4.1

From this discussion, it can be concluded that the Pressure Difference Rule is suitable for swept wings that stall from the leading edge. However, swept wings incorporating trailing-edge stall airfoils are also permitted because the spanwise boundary layer flow retards the trailing edge separation as could be seen in Section 4.2.2. However, the main bottleneck is that the amount of sweep-back dictates the magnitude of boundary layer control as could be seen in Section 2.3.3. Hence, using the PDR on a low-swept wing that incorporates airfoils that stall from the trailing edge might lead to a faulty  $C_{L_{max}}$  prediction. Hence, it is recommended to test this accordingly. Finally, the Critical Section Method as incorporated within this thesis seems to work

solely on straight wings. Hence, for the Initiator, a conjunction of both the PDR and CSM need to be implemented to increase the design space of  $C_{L_{\max}}$  predictability within the Initiator.

# 5

## CONCLUSIONS AND RECOMMENDATIONS

### 5.1. CONCLUSION

Two medium-fidelity methods for the rapid estimation a wing's maximum lift coefficient have been presented. Here, it was found that the quarter-chord sweep angle, airfoil thickness, airfoil nose radius, Mach number, Reynolds number all play a pertinent role in the prediction of the maximum lift coefficient. To account for these effects, multiple computational methods that range from high- to low fidelity can be implemented. After a trade-off, it became evident that both the Pressure Difference Rule (PDR) and Critical Section Method (CSM) excelled in applicability, robustness, and rapidity. Therefore, both methods were scrutinized as candidates to build the  $C_{L_{\max}}$  prediction method within the Initiator.

The Pressure Difference Rule was implemented by coupling a two-dimensional constant-strength vortex-panel method with the downwash model of Elham. For high-lift configurations, a linear-strength vortex-panel method has been coupled to the Elham's downwash model together with a flap reduction curve to account for flap decambering. Also, a generic airfoil parsing and resampling routine has been added to the Initiator to ensure airfoil smoothness in order to obtain feasible results from the vortex-panel methods. Similarly, the Critical Section Method was implemented by coupling the two-dimensional empirical ESDU 84026 method for the prediction of an airfoil's maximum lift coefficient, and the vortex-lattice solver Athena Vortex Lattice. Also, an empirical fuselage correction has been incorporated to account for fuselage effects on the maximum lift coefficient.

Both the Pressure Difference Rule and Critical Section Method were validated against wind tunnel experiments, both for wing only samples and wing + fuselage models. The approximated clean maximum lift coefficient showed to be in good agreement, about 3% error, with wind tunnel experiments for the straight Fokker F27 wing when incorporating the Critical Section Method. A contrast was observed with the Pressure Difference Rule, where an over-estimation of 180 % resulted for the straight wing case. This large over prediction originates from the fact that the Pressure Difference Rule is not suitable on wings that incorporate airfoils that stall from the trailing edge, such as on the Fokker F27. This information became apparent after an interview with the leading researcher behind the Pressure Difference Rule. Within this interview, it became apparent that the Pressure Difference Rule is solely applicable to wings that stall from the leading edge, a phenomenon commonly found on thin swept-back wings.

Similarly, swept wings have been tested with both the Pressure Difference Rule and Critical Section Method. Here, the Pressure Difference Rule was within a 5% error margin for three clean swept-back wings. During the validation, a peculiarity established because one of the validated clean wings stalled from the trailing edge while it was mentioned that the Pressure Difference Rule is incapable of accurately predicting the  $C_{L_{\max}}$  for these stall cases. This phenomenon stems from the fact that the wing under scrutiny, a wing with 45° quarter chord sweep and 10° tip washout, showed a form of natural boundary layer control due to a spanwise boundary layer flow. Due to this, the trailing-edge separation changed to a leading-edge type of separation and the PDR yielded an accurate estimation. On the contrary, The CSM lacked fidelity in determining the  $C_{L_{\max}}$  of swept wings. The reason for this was due to the negligence of the prior mentioned boundary layer control due to spanwise boundary layer flow. Due to this, the wing section's  $c_{l_{\max}}$  is locally much higher when compared to the two-dimensional airfoil case. Therefore, the CSM under predicts the  $C_{L_{\max}}$  on swept-back wings.

Continuing, the Pressure Difference Rule was validated against two high-lift swept-back wings which both had a full span single-slotted Fowler flap. Here, it was found that the maximum error in the maximum lift coefficient approximation was +11% on a kinked swept back wing with a 10° deflected single-slotted Fowler flap. The subsequent  $C_{L_{\max}}$  estimations on high-lift wings with flaps deflections of 0°, 25° and 40° showed to be within a 5% error margin when compared to measurements. Finally, the Newton-Raphson root-finding algorithm was incorporated to increase the rapidity of both the PDR and CSM. With this, both the Pressure Difference Rule and Critical Section Method converged within 3 – 4 seconds for a clean configuration and 5 – 7 seconds for high-lift wings.

To conclude, a conjunction between the Pressure Difference Rule and the Critical Section Method is required within the Initiator to increase the design space of  $C_{L_{\max}}$  predictability. This is because the Pressure Difference Rule is applicable to swept wings and straight wings with leading-edge stall while the opposite is true for the Critical Section Method, which solely works on straight wings.

## 5.2. RECOMMENDATIONS

In the following, recommendations regarding future research on the rapid prediction of maximum lift coefficient will be discussed since there is still room for improvements.

### 5.2.1. EXPANSION OF HIGH-LIFT DEVICE IMPLEMENTATION

Developing a rapid boundary layer model for spanwise flow and local 2D wing sections might enhance the  $C_{L_{\max}}$  predictability on swept-back wings. This will yield better approximations of the stall angle and allows one to analyze double/triple slotted flaps in conjunction with slats. This is currently not possible since the intricate boundary layer flows over each high-lift element is being neglected. Also, double-slotted flaps are not considered within this thesis, hence, it is recommended to conduct additional research on this topic.

### 5.2.2. EXPANSION TO TRANSONIC MACH NUMBERS

Also, low-speed maximum lift coefficients have been scrutinized, hence, an endeavor can be made to extend this to transonic Mach numbers by researching boundary layer separation due to shock waves. Here, one can try to find relations between the pressure difference upstream, and downstream of a shock wave to predict separation.

### 5.2.3. INTERFERENCE EFFECTS

It must be recognized that the maximum lift of the wing may be substantially altered by interference effects due to nacelles, pylons, and other protuberances which change the local aerodynamics. These have not been accounted for in the current research. Also, the maximum usable lift coefficient should be considered, because the  $C_{L_{\max}}$  estimated by the methods within this thesis work neglect the pitch break which is often seen on swept-back wings. Therefore, the  $C_{L_{\max}}$  determined within this thesis is often not measured during actual flight testing.

### 5.2.4. TRIM EFFECTS

Similarly, the aircraft's tail alters the maximum lift coefficient in order to trim the aircraft during stall. These trim effects can be significantly strong as swept-back wings stall from the wing tip, which causes large shifts in the center of gravity.

### 5.2.5. SWEEP ANGLE VS $C_{L_{\max}}$ PREDICTION IMPLEMENTATION

As mentioned in the conclusion, it is found that two different methods are required to determine the  $C_{L_{\max}}$  of both straight and swept wings within the initiator. It has shown that both methods heavily depend on sweep angle. However, both methods do not yield similar results at the same sweep angle. This causes a jump in the  $C_{L_{\max}}$  prediction during a convergence loops of the Initiator, which might lead to unfeasible or unwanted aircraft designs. Also, using these two methods in conjunction requires additional information on when spanwise boundary layer flow effects becomes dominant. This feature depends on the spanwise pressure difference that is generated due to the sweep angle, wing section's stalling characteristics and the Mach number and therefore sets a bound to the implementation of the Critical Section Method.

### 5.2.6. FUSELAGE MODEL

Continuing, A fuselage correction model has been implemented. However, this methods does not account for anhedral and diherdral of the wing. Also, the vertical position of the wing w.r.t the fuselage was neglected. Hence, additional work regarding this can be conducted.

### 5.2.7. DOWNWASH MODEL

For the downwash model, use have been made of the PhD thesis of Elham. Within this downwash model, it is assumed that the wing sees a clean and undisturbed flow. However, the Initiator is also capable of designing business jet aircraft. These businesses jets occasionally utilize canards, which produce a downwash upstream of the main wing. This additional downwash component is not considered within this thesis while it can have a significant effect on the stalling characteristics of the main wing. Similarly, winglets at the ends of wing tips are often incorporated on both business- and commercials airliners. These winglets effectively decrease the induced angle of attack produced by the main wing by retarding the leaking of the boundary layer at the wing tip. This effects on the local downwash angle on a wing section is neglected and required additional research.

### 5.2.8. MODIFIED PRESSURE DIFFERENCE RULE

The Modified Pressure Difference Rule was presented. Here, it showed that it lacked either theoretical justification or accuracy. Additional wind tunnels tests are required to expand the Pressure Difference Rule for wings that incorporate airfoils that stall from the trailing edge. Also, additional validation cases should be consulted to test whether the Pressure Difference Rule is applicable to wings that have a moderate to low sweep angle and incorporate airfoils that stall from the trailing edge. The reason for this is that the trailing-edge boundary layer control, on a swept-back wing, increases with sweep angle. Therefore, the accuracy of the Pressure Difference Rule depends on the magnitude of the trailing-edge boundary layer stall suppression.

### 5.2.9. NEWTON-RAPHSON STABILITY ANALYSIS

Finally, the Newton-Raphson method has been incorporated to increase the rapidity of the computations. Additional research regarding the convergence and root overshoot should be conducted. Also, the implemented derivatives should be researched for their continuity.



# II

## PART II: CODE REPORT



# 1

## INTRODUCTION

In the first part of this thesis report, methods to estimate the maximum lift coefficient during the conceptual design of an aircraft have been researched and validated accordingly. Hereby, it was found that the Critical Section Method and Pressure Difference Rule excelled in predicting the maximum lift coefficient in the early design stages of an aircraft. In the Part II of this thesis, the developed  $C_{L\max}$  prediction tool derived from the research conducted in Part I of this thesis is presented. The developed  $C_{L\max}$  prediction tool is incorporated, as a sub module, within TU Delft's Initiator which is a MatLab based conceptual/preliminary aircraft design tool developed by TU Delft's Flight Performance and Propulsion Department. The implementation of this sub module was required since the predictability of  $C_{L\max}$  lacked fidelity and consistency within Initiator Version 2.6. Therefore, incorporating the researched  $C_{L\max}$  prediction methods within Initiator Version 2.9, introduces the possibility of capturing the effects of the  $C_{L\max}$  on preliminary aircraft design.

Within Part II of this thesis, the requirements for developing a maximum lift coefficient prediction tool are presented in Chapter 2. From this, a better insight of the required capabilities of the  $C_{L\max}$  prediction tool are laid out. Then in Chapter 3, the  $C_{L\max}$  prediction tool is discussed. Here, a full description of the developed tool is provided by using a top down activity diagram with a accompanied flow charts for the Pressure Difference Rule implementation. Finally, the limitations of the  $C_{L\max}$  prediction tool alongside a discussion on the future work within the Initiator are presented in Chapter 3.



# 2

## DEVELOPMENT REQUIREMENTS

The requirements for developing a  $C_{L_{\max}}$  prediction tool for the conceptual design phase of an aircraft are discussed in this chapter. With this, one is able to expose the required capabilities of the  $C_{L_{\max}}$  prediction tool. Also, means to incorporate the  $C_{L_{\max}}$  prediction tool within the Initiator become evident. Therefore, Section 2.1 discusses the scope of the tool with the accompanied limitations. Then, Section 2.2 defines the different cases for which the developed tool can be utilized. Subsequently, an analysis on the tool's requirements is presented in Section 2.3. Finally, the assumptions used within the developed tool are given in Section 2.4.

### 2.1. SCOPE & LIMITATIONS

Before one can utilize the developed  $C_{L_{\max}}$  prediction tool, both the scope and limitations of this tool have to be laid out. As such, the scope of the developed tool is limited to *the low-speed maximum lift prediction of wing fuselage combinations in both clean and high-lift conditions where both plain- and single-slotted flaps can be analyzed on a mid-wing configuration*. Therefore, this tool allows the Initiator to capture the effects of the maximum lift coefficients on the overall conceptual design of an aircraft. The described scope has been formalized by defining the limitations of the maximum lift coefficient prediction tool. The most significant limitations are that the tool is solely applicable to MatLab since the built-in function of MatLab have been used extensively. Also, the developed tool is only applicable from the Initiator Version 2.9 and onward, since crucial changes have been implemented within this version of the Initiator. Two other limitations have to be taking into account during the implementation the tool, namely:

- The developed tool is only applicable for the prediction low-speed  $C_{L_{\max}}$  because the interaction between shocks and boundary layers is omitted.
- High-lift devices are included. However, these only encompass plain flaps and single-slotted flaps.

As for the low-speed limitation, the stalling characteristics of wings in transonic flow are significantly different from their low-speed counterpart. In transonic flow, shocks are often formed on bot the upper- and lower side of the wing. This shock interacts with the local boundary layer by exciting a disturbance. This disturbance depends on the strength of the shock, which is dictated by the freestream Mach number and the effective curvature of the wing. If the magnitude of this disturbance is high enough, the boundary layer detaches from the wing surface and stall is reached. This yields the transonic  $C_{L_{\max}}$  which has a significant importance. However, the low-speed maximum lift coefficient has a great impact on the wing size and accompanied wing loading. As such, the low-sweep  $C_{L_{\max}}$  is a key-performance indicator in the early design stages of an aircraft.

Secondly, the tool is limited to plain- and single-slotted flaps. This fact originates from the fact that on a slat, the suction peak is high enough to form a shock. In the current methodology, described in Chapter 3, no methods are presented that cope with this. Hence, to ensure feasible  $C_{L_{\max}}$  predictions, slats are omitted from the tool. Similarly, the intricate mutual interference effects which are present on double-slotted flaps are

omitted because the implemented methods lack theoretical justification for the high-lift configuration. Finally, the implementation of trip-slotted flaps are omitted because aircraft designers often find these systems too heavy and complex to be of any benefit to an economically viable aircraft.

## 2.2. USE CASES

Several use cases are defined for which the  $C_{L_{max}}$  prediction tool can provide an accurate estimation of the maximum lift coefficient. These cases also agree with the purpose and research questions that are presented Part I, Section 1.2. To summarize, the  $C_{L_{max}}$  prediction tool allows the Initiator to do the following:

1. The estimation of the clean low-speed  $C_{L_{max}}$  for straight wings.
2. The estimation of the clean low-speed  $C_{L_{max}}$  for swept-back wings.
3. The estimation of the high-lift  $C_{L_{max}}$  for the above mentioned cases.
4. The estimation of the stall angle for the above mentioned cases.

## 2.3. REQUIREMENTS

To develop a tool which is to be seamlessly incorporated within the Initiator, it is essential to define the requirements of the tool. This information provides the scope in which the tool should operate. As such, computational methods can be chosen accordingly to meet the requirements. In the following, the key requirements on the  $C_{L_{max}}$  prediction tool are discussed.

- For the research project at hand, the maximum lift coefficient of an aircraft is analyzed. With this, the output of the tool should ideally yield both the  $C_{L_{max}}$  and associated stall angle,  $\alpha_{text{stall}}$ .
- The Initiator is a MatLab based tool. As such, the  $C_{L_{max}}$  prediction tool, with associated methods, should either be programmable or executable from within the MatLab working environment.
- Also, the aircraft design phase for which the  $C_{L_{max}}$  prediction tool has to be developed is a point of consideration. In doing so, the preferred analysis methods to estimate  $C_{L_{max}}$  can be determined. As the Initiator performs a conceptual/preliminary aircraft design, the estimation of  $C_{L_{max}}$  should be adjusted for computational expense and accuracy. Therefore, a computational time of not more than 15 seconds is allocated to the prediction of  $C_{L_{max}}$  within the Initiator. Due to this, the used methods will most likely incorporate a degree of empiricism to allow for a rapid  $C_{L_{max}}$  estimation.
- The  $C_{L_{max}}$  prediction tool is used during the conceptual aircraft design stage. Therefore, a degree of flexibility should be presented which allows for the analysis of a wide range of aircraft designs.
- At last, the tool should incorporate a degree of user friendliness. With this, it is implied that the developed MatLab code is easy to follow and adjust. Also, an accompanying documentation on working principles behind the tool are necessary to guide used. Another feature is to incorporate comments within the MatLab code to elaborate difficult code structures and guide the user though the tool.

## 2.4. ASSUMPTIONS & SIMPLIFICATIONS

To analyze the maximum lifting capability of a lifting surface within a conceptual design, several assumptions and simplifications are made. Here, the main assumptions adhered to in the  $C_{L_{max}}$  prediction tool are presented.

First, interference effects are omitted. These interferences can for example stem from local fences on top of the wing. Also, pylons, nacelles, and movables can locally change the aerodynamics. Also, it is assumed that the flow over the wing is turbulent, which means that the occurrence of a laminar separation bubble is not considered. This is a justified assumption, since the boundary layer on the swept wing of a conventional airliner often transitions at the leading edge due to local disturbances. Similarly, it is assumed that the wings, that are to be analyzed, do not have winglets. As such, the induced angle of attack approach discussed in Section 3.2.2 might yield unfeasible results for wings that implement winglets.

Within the  $C_{L_{\max}}$  prediction tool, it is assumed that the trim forces, which are generated by the tail, are small compared to the  $C_{L_{\max}}$  component of the wing only. As such, these effects are omitted in the current approach. Also, it is assumed that the predicted  $C_{L_{\max}}$  gives a proper estimation of the usable  $C_{L_{\max}}$ . Here, pitch break, wing rock, and buffet effects are omitted from the current analysis.

The assumed planform is such that the quarter chord sweep angles range between  $0^\circ$  and  $50^\circ$ . Hereby, the occurrence of a leading-edge vortex that traverses over the wing is neglected. Similarity, in the MatLab code it is assumed that the wing under scrutiny has not more than one spanwise kink. This is a feature often seen in commercial airliners. Also, the aircraft is assumed to have a symmetric wing, since only one side of the wing is analyzed to reduce the computational time. Here, the symmetry axis is placed through the x-z plane of the aircraft as can be seen in Figure 2.1.

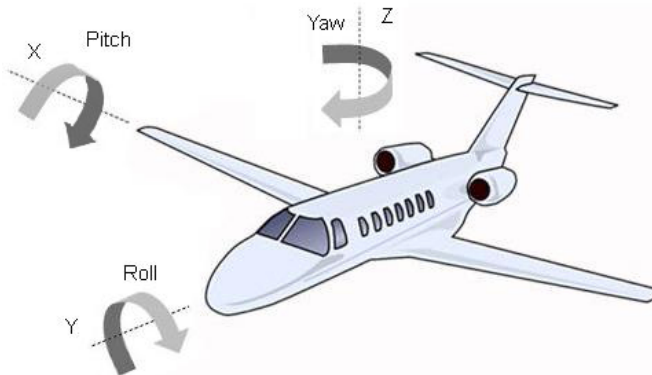


Figure 2.1: Aircraft axis system



# 3

## PREDICTION TOOL

Within this Chapter, a description is given for the implemented  $C_{L_{\max}}$  prediction tool. Hereby, the work flow is discussed and a guide is provided to get started with the tool. In Section 3.1 the tool is presented and proposed future work is discussed in Section 3.3

### 3.1. THE TOOL

A schematic overview of the developed tool is presented in Figure 3.1. Initially, the geometry details are obtained from the Initiator controller alongside the operation conditions of the aircraft. Then, a decision follows, when the preferred method is selected. From the conclusions of Part I of this thesis, it became evident that the CSM is able predict the  $C_{L_{\max}}$  accurately on straight wings while the PDR is preferred on swept wings. Also, the PDR did not yield accurate results on straight wings that stall from the leading edge. Therefore, it was chosen to utilize the CSM for straight wings in general regardless of stalling condition as this avoids the need to determine the stalling characteristics of the wing under scrutiny. Then, the estimated wing-only  $C_{L_{\max}}$  is passed to the Datcom method to correct for the presence of the fuselage.

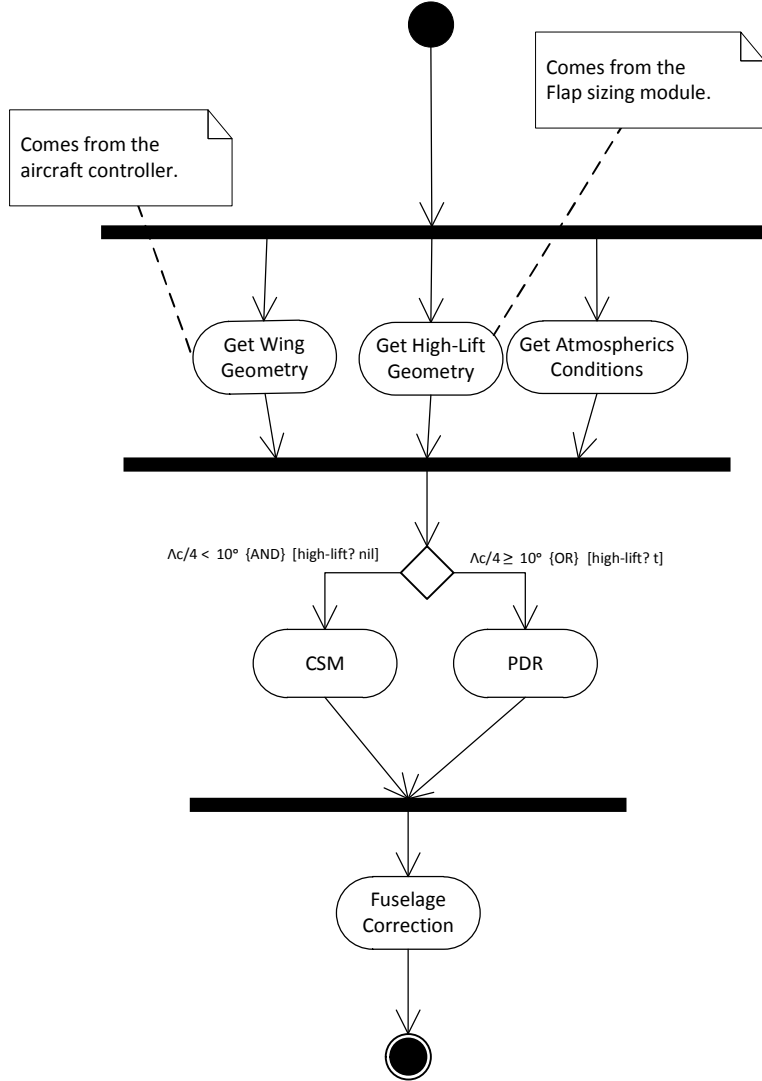


Figure 3.1: Overview of the prediction method as implemented in the Initiator

To highlight the Pressure Difference Rule, Figure 3.2 is constructed. Here, a flow chart over the operations within the Pressure Difference Rule are depicted. Here, the linear-strength vortex panel method is illustrated for the high-lift  $C_{L_{max}}$  prediction. For a clean wing, the linear-strength vortex panel method is replaced by the constant-strength vortex panel method while the flowchart of Figure 3.2 still holds.

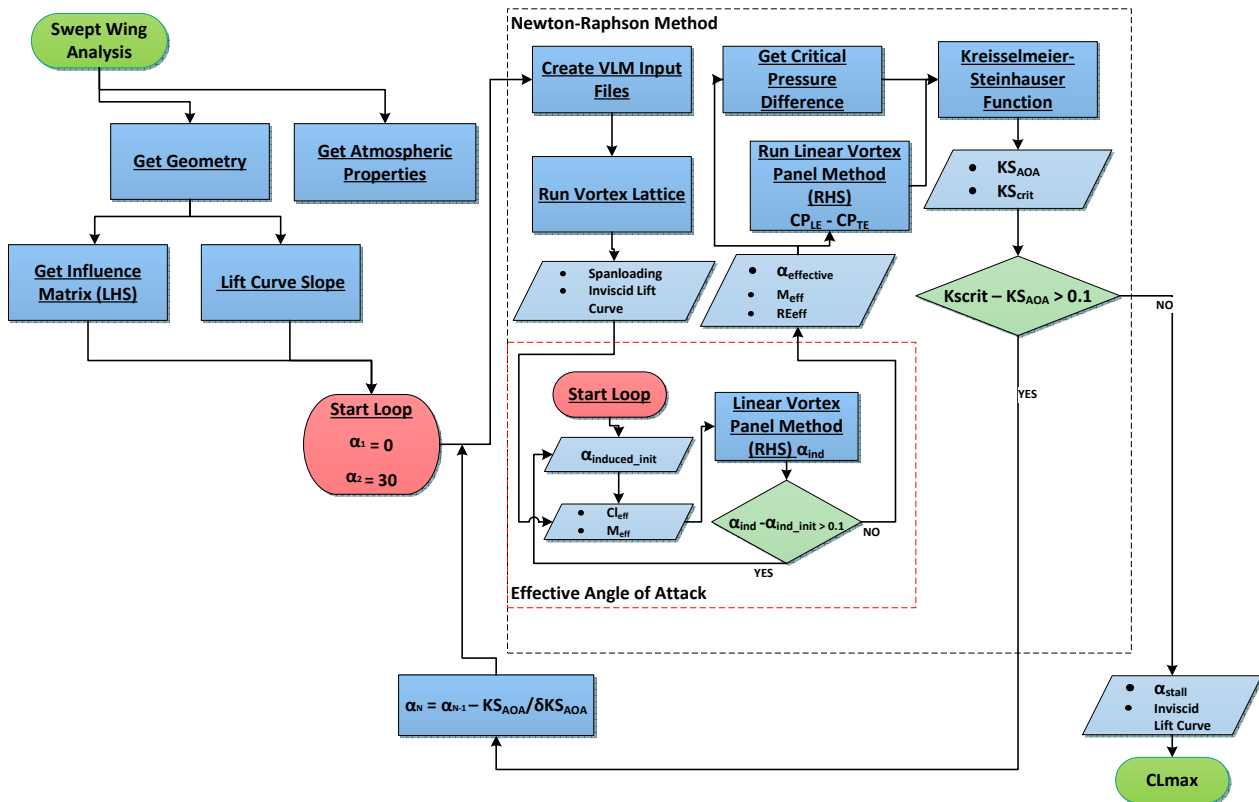


Figure 3.2: Overview of the Pressure Difference Rule as implemented in the Initiator

### 3.2. WORKING GUIDE

The working principles are as follows:

- Initially, one needs to make sure that the AVL directory is empty.
- Subsequently, the Initiator controller sends the  $C_{L_{\max}}$  module specifications on the grid size, which is to be used in the VLM, along with the operating altitude and fuselage diameters.
- Then, the wing geometry is defined. Here, the basic wing geometry is obtained from the Initiator controller. However, additional geometry needs to be specified. To summarize: the airfoil geometry needs to be specified at every wing break or discontinuity in order to build the vortex-lattice grid properly as discussed in Chapter 3 of the Part I. Here, the flap geometry needs to be also specified at every discontinuity of the wing. The considered discontinuities are a wing kink and a change from a high-lift wing section to a clean wing section. For example, Figure 3.3 indicates an example wing. Here, the wing has both a trailing edge flap segment and a kink. At the kink, the airfoil section, either clean or high-lift, need to be specified. Also, the position of the flap hinge should be input to model the trailing edge of the flap and position the flap in the vortex-panel methods. Finally, the flap deflection should be specified. All the high-lift specifications should be written in the *CLmaxInput.m* file as the module inputs are collected here.
- Finally, a low-speed Mach number should be passed to the  $C_{L_{\max}}$  module from the Initiator controller.

To use the Module, the run file within the folder AnalysisModules/CleanCLmax should be ran after specifying an aircraft geometry with the .xml files. From this, the maximum lift coefficient of the wing, wing fuselage combination and the stall angle are determined by the module. These quantities are subsequently passed to the Initiator controller so it can be used elsewhere in the Initiator.

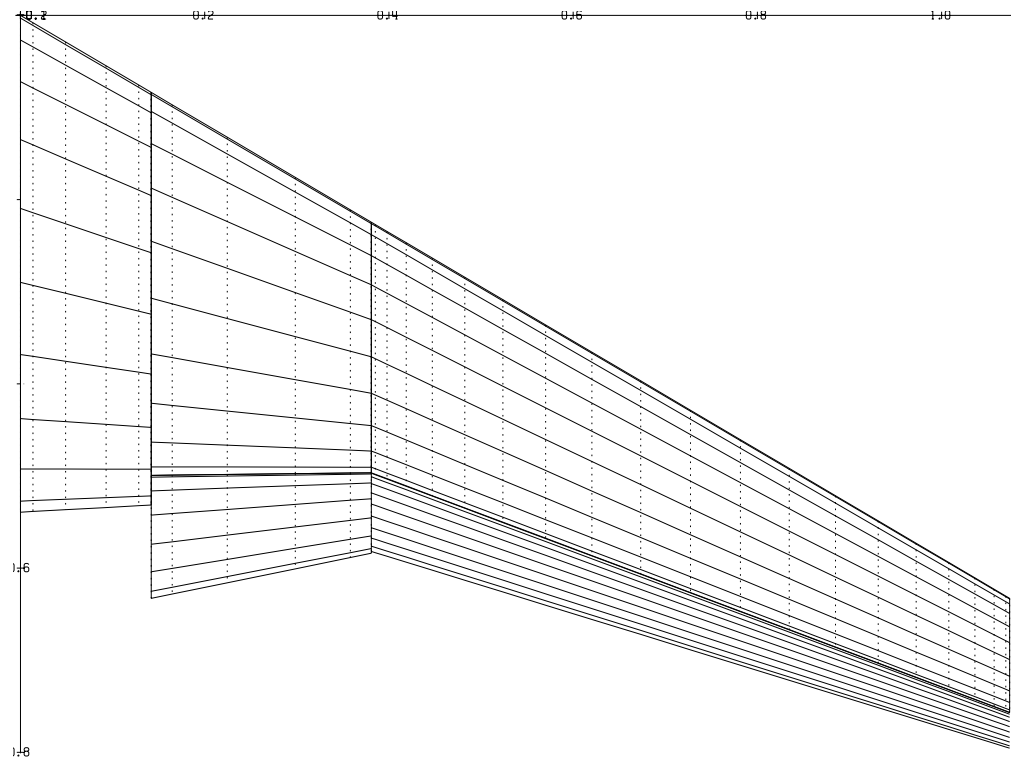


Figure 3.3: Sample Wing

### 3.3. FUTURE WORK

As for the future work of this module the following can be said:

- The low-speed Mach number remains undefined. Therefore, the Initiator needs a new definition for this quantity. Either as an user-input or with an analysis.
- Secondly, a proper high-lift sizing module should be implemented as the Initiator Version 2.9 lacks this as of now.
- Finally, slats and double-slotted flaps should be included within the Initiator to increase the conceptual design space.

# 4

## DEVELOPMENT REQUIREMENTS



# A

## APPENDIX A: HIGH-LIFT AVL INPUT FILE

```

RAE Wing
# Mach
0.223
# IYsym IZsym Zsym
1 0 0
# Sref Cref Bref
0.5523 0.2572 2.148
# Xref Yref Zref
0 0 0
#
#
#=====
SURFACE
RAE MAIN WING (ROOT)
#Nchordwise Cspace Nspanwise Sspace
10 1 0 0
#
COMPONENT
1
#
ANGLE
0.00000
#-----
SECTION
# Xle Yle Zle Chord Ainc Nspan Sspace
0 0 0 0.5393 0 5 1
CLAF
0.9613
AFILE
Lovell.dat

SECTION
# Xle Yle Zle Chord Ainc
0.0836 0.142 0 0.448 0
CLAF
0.9613
AFILE
Lovell.dat
#=====
SURFACE
RAE MAIN WING (Pre-Kink)
#Nchordwise Cspace Nspanwise Sspace
10 1 0 0
#
COMPONENT
1
#
ANGLE
0.00000
#-----
SECTION
# Xle Yle Zle Chord Ainc Nspan Sspace
0.0836 0.142 0 0.4158 0 5 1
CLAF
1.0513
AFILE
Lovell.dat

SECTION
# Xle Yle Zle Chord Ainc

```

```

    0.224515    0.3810      0   0.27204   0
CLAF
1.0513
AFILE
Lovell.dat
#=====
SURFACE
RAE MAIN WING
#Nchordwise   Cspace   Nspanwise   Sspace
10          1           0           0
#
COMPONENT
1
#
ANGLE
0.00000
#-----
SECTION
# Xle      Yle      Zle   Chord   Ainc   Nspan Sspace
  0.224515    0.3810      0   0.27204   0     20    1
CLAF
1.0513
AFILE
Lovell.dat

SECTION
# Xle      Yle      Zle   Chord   Ainc
  0.63288    1.074      0       0.1238322 0
CLAF
1.0513
AFILE
Lovell.dat
#=====
SURFACE
INBOARD FLAP
#Nchordwise   Cspace   Nspanwise   Sspace
6          1           0           0
#
COMPONENT
1
#
ANGLE
0.00000
#-----
SECTION
# Xle      Yle      Zle   Chord   Ainc   Nspan Sspace
  0.4994     0.142      0   0.13348   29     5    1
CLAF
1.0513
AFILE
LovellFlap.dat

SECTION
# Xle      Yle      Zle   Chord   Ainc
  0.496555    0.3810      0       0.087329 29
CLAF
1.0513
AFILE

```

```

LovellFlap.dat
#=====
SURFACE
OUTBOARD FLAP
#Nchordwise   Cspace     Nspanwise    Sspace
10           1           0           0
#
COMPONENT
1
#
ANGLE
0.00000
#-----
SECTION
# Xle      Yle      Zle      Chord      Ainc  Nspan Sspace
  0.496555  0.3810    0       0.087329    29   20   1
CLAF
1.0513
AFILE
LovellFlap.dat

SECTION
# Xle      Yle      Zle      Chord      Ainc
  0.7567122  1.074    0       0.039739  29
CLAF
1.0513
AFILE
LovellFlap.dat
#=====

```

# BIBLIOGRAPHY

- [1] Radical Departures, "Forecast for global aviation soars," 2016, visited 15-12-2016.
- [2] Airbus, "Global market forecast 2016-2035," 2016, visited 15-12-2016.
- [3] E. Obert, *Aerodynamic Design of Transport Aircraft*. Ios Press, 1 ed., 2009.
- [4] C. P. van Dam, "The aerodynamic design of multi-element high-lift systems for transport airplanes," *Progress in Aerospace Sciences*, vol. 38, no. 2, pp. 101–144, 2002.
- [5] P. T. Meredith, "Viscous phenomena affecting high-lift systems and suggestions for future cfd development," *AGARD-CP-515: High-Lift System Aerodynamics (1993) Chap.31*.
- [6] C. L. Rumsey and S. X. Ying, "Prediction of high lift: review of present CFD capability," *Progress in Aerospace Sciences*, vol. 38, no. 2, pp. 145–180, 2002.
- [7] C. L. Rumsey, J. P. Slotnick, M. Long, R. A. Stuever, and T. R. Wayman, "Summary of the first AIAA CFD high lift prediction workshop," *Journal of Aircraft*, vol. 48, no. 6, pp. 2068–2079, 2011.
- [8] C. L. Rumsey and J. P. Slotnick, "Overview and summary of the second AIAA CFD high-lift prediction workshop," *Journal of Aircraft*, vol. 0, no. 0, pp. 1–20, 2014.
- [9] D. P. Raymer, *Aircraft Design: A Conceptual Approach*. AIAA Education Series, 1 ed., 1996.
- [10] S. Gudmundsson, *General Aviation Aircraft Design: Applied Methods and Procedures*. Elsevier, 1 ed., 2013.
- [11] P. Sforza, *Commercial Airplane Design Principles*. Butterworth Heinemann, 1 ed., 2014.
- [12] R. D. Finck, "USAF stability and control Datcom," tech. rep., McDonnell Douglas Corporation, 1978.
- [13] A. Slingerland, "Preliminary Sizing of Conventional and Unconventional Aircraft," Master's thesis, Delft University of Technology, 2014.
- [14] R. J. M. Elmendorp, "Synthesis of Novel Aircraft Concepts for Future Air Travel," Master's thesis, Delft University of Technology, 2014.
- [15] T. Langen, "Development of a conceptual design tool for conventional and boxwing aircraft," Master's thesis, Delft University of Technology, 2011.
- [16] F. Vaessen, "Improved aerodynamic analysis to predict wing interaction of high-subsonic three-surface aircraft," Master's thesis, Delft University of Technology, 2013.
- [17] J. v. Dommelen, "Design of a Forward-Swept Blended Wing Body Aircraft," Master's thesis, Delft University of Technology, 2011.
- [18] M. Hoogreef, "The Oval Fuselage," Master's thesis, Delft University of Technology, 2012.
- [19] R. Vos and S. Farokhi, *Introduction to Transonic Aerodynamics*. Springer, 1 ed., 2015.
- [20] P. D. Chappell, "The maximum lift coefficient of plain wings at subsonic speeds," *IHS ESDU 89034*, 1989.
- [21] J. J. Ruijgrok, *Element of Airplane Performance*. VSSD, 2 ed., 2009.
- [22] A. M. O. Smith, "High-lift aerodynamics," *Journal Aircraft*, vol. 12, no. 6, pp. 501–530, 1975.
- [23] P. K. C. Rudolph, "High-lift systems on commercial subsonic airliners," tech. rep., NASA, Seattle, WA, 1996.

- [24] R. S. Pepper, C. P. v. Dam, and P. A. Gelhausen, "Design methodology for high-lift systems on subsonic transport aircraft," in *AIAA, NASA, and ISSMO, Symposium on Multidisciplinary Analysis and Optimization* (AIAA, Reston, VA), 1996.
- [25] G. B. McCullough and D. E. Gault, "Examples of three representative types of airfoil - section stall at low speed," tech. rep., National Advisory Committee for Aeronautics, 1951.
- [26] F. G. Chester and J. G. Mchugh, "A summary and analysis of the low-speed longitudinal characteristics of swept wings at high Reynolds number," tech. rep., National Advisory Committee for Aeronautics Langley Aeronautical Lab; Langley Field, VA, United States, 1957.
- [27] D. E. Gault, "A correlation of low-speed, airfoil-section stalling characteristics with Reynolds number and airfoil geometry," tech. rep., National Advisory Committee for Aeronautics, 1957.
- [28] "The low-speed stalling characteristics of aerodynamically smooth aerofoils," *IHS ESDU 66034*, 1966.
- [29] C. W. Harper and R. Maki, "A review of the stall characteristics of swept wings," tech. rep., National Aero-nautic and Space Administration, Ames Aeronautical Lab; Moffet Field, CA, United States, 1964.
- [30] A. Elham and M. J. L. Tooren, "Coupled adjoint aerostructural wing optimization using quasi-three-dimensional aerodynamic analysis," *Structural and Multidisciplinary Optimization*, pp. 1–18, 2016.
- [31] J. R. Spreiter and J. Steffen, "Effect of Mach and Reynolds numbers on maximum lift coefficient," tech. rep., National Advisory Committee for Aeronautics, 1946.
- [32] H. Abbot and A. E. von Doenhoff, *Theory of Wing Sections*. Dover Publications, 1 ed., 2012.
- [33] J. V. van der Vaart and H. Muhammad, "Static longitudinal stability and control characteristics of the Fokker F27 "Friendship" calculated by simple handbook methods," tech. rep., Technische Universiteit Delft, 1983.
- [34] R. L. Maki, "The use of two-dimensional section data to estimate the low-sweep wing lift coefficient at which section stall first appears on a swept wing," tech. rep., National Advisory Committee for Aeronau-tics Washington, United States, 1951.
- [35] W. F. Phillips and N. R. Alley, "Predicting maximum lift coefficient for twisted wings using lifting - line theory," *AIAA Journal*, vol. 44, no. 3, pp. 10847–10855, 2007.
- [36] W. F. Phillips, N. R. Alley, and R. E. Spall, "Predicting maximum lift coefficient for twisted wings using computational fluid dynamics," *AIAA Journal*, vol. 44, no. 3, pp. 911–917, 2007.
- [37] W. O. Valerzo and V. D. Chin, "Method for the prediction of wing maximum lift," *Journal Aircraft*, vol. 31, no. 1, 1994.
- [38] P. D. Chappell, "Increments in aerofoil lift coefficient at zero angle of attack and in maximum lift coef-ficient due to deployment of a single-slotted trailing-edge flap, with or without a leading-edge high-lift device, at low speeds," *IHS ESDU 94030*, 1995.
- [39] R. L. Burden and J. D. Faires, *Numerical Analysis*. Prindle, Weber & Schmidt, 1985.
- [40] E. T. Whittaker and G. Robinson, *The Calculus of Observations: An Introduction to Numerical Analysis*. Springer, 1967.
- [41] M. Drela, "Athena Vortex Lattice (AVL) source page." <http://web.mit.edu/drela/Public/web/avl/>, 2008. Accessed: 2016-09-23.
- [42] C. D. Hollis and R. G. Williams, "Aerofoil maximum lift coefficient for Mach numbers up to 0.4," *IHS ESDU 84026*, 1984.
- [43] J. Katz and A. Plotkin, *Low-Speed Aerodynamics*. McGraw-Hill, 2 ed., 1991.
- [44] A. Elham, *Multidisciplinary Design Optimization of Lifting Surfaces*. PhD thesis, Delft University of Tech-nology, 2013.

- [45] M. Drela, "XFOIL source page." <http://web.mit.edu/drela/Public/web/xfoil/>, 1989. Accessed: 2016-09-23.
- [46] M. Drela, "MSES source page." <http://web.mit.edu/drela/Public/web/mses/>, 2007. Accessed: 2016-10-29.
- [47] E. Moerland, "Development of an Aeroelastic Analysis Tool for Structural Sizing of High-lift Devices During Preliminary Design," Master's thesis, Delft University of Technology, 2011.
- [48] C. A. Cox, "Two Element Linear Strength Vortex Panel Method," Master's thesis, California Polytechnic State University, San Luis Obispo, 2011.
- [49] E. Torenbeek, *Synthesis of Subsonic Airplane Design: An introduction to the preliminary design of subsonic general aviation and transport aircraft, with emphasis on layout, aerodynamic design, propulsion and performance*. Springer Netherlands, 1982.
- [50] L. E. Murillo and J. H. McMasters, "A method for predicting low-speed aerodynamic characteristics of transport aircraft," *Journal Aircraft*, vol. 21, no. 3, 1983.
- [51] K. v. d. Kieboom and A. Elham, "Combined aerostructural wing and high-lift system optimization," *17th AIAA/ISSMO Multidisciplinary Analysis and Optimization Conference, Washington, DC*, 2016.
- [52] G. J. Kennedy and J. R. R. A. Martins, "A comparison of metallic and composite aircraft wings using aerostructural design optimization," *14th AIAA/ISSMO multidisciplinary analysis and optimization conference, Indianapolis, IN*, 2012.
- [53] G. A. Wrenn, "An indirect method for numerical optimization using the Kreisselmeier-Steinhauser function," tech. rep., National Advisory Committee for Aeronautics, 1989.
- [54] C. D. Harris, R. J. McGhee, and D. O. Allison, "Low-speed aerodynamic characteristics of a 14-percent-thick nasa phase 2 supercritical airfoil designed for a lift coefficient of 0.7," tech. rep., National Aeronautics and Space Administration, 1980.
- [55] J. A. Shortal and B. Maggin, "Effects of sweepback and aspect ratio on longitudinal stability characteristics of wings at low speeds," tech. rep., National Advisory Committee for Aeronautics, 1981.
- [56] D. A. Lovell, "A wind-tunnel investigation of the effects of flap span and deflection angle, wing planform and a body on the high-lift performance of a 28° swept wing," tech. rep., Aeronautical Research Council, C.P. No. 1372, London, 1977.
- [57] C. L. Spigt and A. de Gelder, "Windtunnel metingen aan een model van de Fokker F27 "Friendship" uitgevoerd in de lage snelheidstunnel," tech. rep., Technische Universiteit Delft, 1959.
- [58] C. Spoon, "Windtunnel metingen aan een model van de vleugel van de Fokker F27 "Friendship" in de lage snelheidstunnel van de onderafdeling Vliegtuigbouwkunde," tech. rep., Technische Universiteit Delft, 1961.
- [59] L. W. Hunton, "Effects of finite span on the section characteristics of two 45° swept-back wings of aspect ratio 6," tech. rep., National Advisory Committee for Aeronautics Ames Aeronautical Lab; Moffet Field, CA, United States, 1952.
- [60] L. W. Hunton and J. K. Dew, "The effects of camber and twist on the aerodynamic loading and stalling characteristics of a large-scale 45° swept-back wing," tech. rep., National Advisory Committee for Aeronautics Ames Aeronautical Lab; Moffet Field, CA, United States, 1951.